

Multi-mode cooling techniques for trapped ions

Dissertation

zur Erlangung des Doktorgrades an der
Fakultät für Mathematik, Informatik und Physik
der Leopold-Franzens-Universität Innsbruck

vorgelegt von

Regina Lechner

durchgeführt unter der Leitung von
o. Univ.-Prof. Dr. Rainer Blatt

Innsbruck, August 2016

The experimental work for this thesis has been carried out at the

Leopold-Franzens-Universität Innsbruck

Institut für Experimentalphysik
Technikerstraße 25
6020 Innsbruck
Austria

and the

Institut für Quantenoptik und Quanteninformation (IQOQI)

der Österreichischen Akademie der Wissenschaften
Otto-Hittmair-Platz 1
6020 Innsbruck
Austria

Abstract

Trapped atomic ions localized with Paul traps are one of the most promising realizations for quantum computers and quantum simulators. The traps confine the ions using alternating electric fields. However, scaling up such a trapped-ion quantum computer to large numbers of ions, which serve as the basis for the quantum computation, remains a challenge.

The trapped ions interact with each other via Coulomb repulsion. This interaction leads to a motion of the trapped ions, which can be described in terms of motional modes. These motional modes can be used to implement entangling-gate operations, which are necessary to execute algorithms. The realization of such gate operations relies on the ability to specifically address individual modes. However, all attempts of scaling up a trapped-ion quantum computer relying on a large number of ions confined within the same harmonic potential lead to an increase in the mode-spectrum density. Thus, the addressing of individual modes requires a narrow bandwidth laser, which is experimentally challenging to achieve. But if such a narrow bandwidth laser is available, it can ever only address one mode after the other leading to a lengthy process. However, precise control of the mode spectrum in terms of the modes' vibrational excitation can also be realized using laser-cooling methods.

This thesis presents methods to control the excitation of motional modes with laser-cooling methods implemented in two different trap geometries. Special interest is put on the implementation of electromagnetically induced transparency (EIT) cooling. The fast broadband cooling behavior provided by this scheme is sought-after in a wide range of applications ranging from quantum gas microscopes to cooling of nanomechanical resonators. For quantum information processing with trapped ions, the results presented in this thesis characterize an improvement compared to commonly used sideband-cooling schemes. The superior cooling properties allow an increase in the number of quantum resources used, which is synonymous with an increase in the computational power available. Thus, it is one additional step to outperform classical computers on an increasing number of tasks in the near future.

A segmented microtrap was used to obtain data on repetitive sideband cooling and cooling relying on EIT applied to up to two trapped ions. These data indicated that EIT cooling has a broadband nature that could be extended to more ions. Systematic instabilities of the segmented trap setup prevented investigations of larger ion crystals. Thus, additional measurements were carried out using a macroscopic ion trap.

EIT cooling was implemented in a macroscopic linear trap setup with the ability to stably trap long ion strings. Subsequently, the cooling bandwidth and cooling rate of the EIT cooling scheme were characterized using ion crystals with up to eighteen ions. Such large crystals share the vibrational excitation of a motional mode over the whole ion string due to Coulomb repulsion. Therefore, techniques used to investigate a mode's vibrational excitation for single ions are

no longer applicable. Thus, some of the results were obtained applying a novel measurement method based on rapid adiabatic passage (RAP).

Zusammenfassung

Paulfallen ermöglichen die Speicherung geladener Teilchen durch elektrische Wechselfelder. Die so gefangenen Ionen bilden die Basis einer der vielversprechendsten Realisierungen von Quantencomputern und Quantensimulatoren. Die Skalierbarkeit eines solcherart implementierten Quantencomputers zu einer großen Anzahl von Ionen, welche die Grundbausteine für Berechnungen sind, stellt jedoch eine Herausforderung dar.

Bedingt durch ihre Ladung wechselwirken die gespeicherten Ionen durch Coulomb Abstoßung, was zu einer Bewegung der Teilchen um ihre Gleichgewichtsposition führt. Diese Auslenkung wird durch Bewegungsmoden beschrieben, welche zur Implementierung von verschränkenden Gatteroperationen genutzt werden können. Solche Gatteroperationen sind notwendig, um Algorithmen zu realisieren. Die Anwendung einer verschränkenden Gatteroperation beruht auf der Fähigkeit bestimmte Moden individuell ansprechen zu können.

Eine Systemvergrößerung anhand einer steigenden Anzahl gefangener Ionen innerhalb desselben Potentialtopfes geht mit einer Verdichtung des Modenspektrums einher. Aus diesem Grund bedarf es eines Lasers mit schmaler Linienbreite um individuelle Moden zu adressieren. Zum einen ist es experimentell aufwändig solch einen Laser zu realisieren, zum anderen ist solch ein schmalbandiger Laser nur in der Lage mehrere Moden hintereinander anzusprechen. Dies bedeutet für die Anwendung des Lasers auf eine Vielzahl von Moden eine zeitliche Verlängerung des angestrebten Prozesses. Eine präzise Kontrolle der Anregung des Modenspektrums kann jedoch durch Laserkühlung erzielt werden.

In dieser Arbeit wird die Anwendung von Laserkühlverfahren zur Kontrolle der Ionenbewegung in zwei unterschiedlichen Fallengeometrien präsentiert, wobei spezielles Augenmerk auf der Kühlung durch elektromagnetisch induzierte Transparenz (EIT) liegt. Die Eigenschaft der schnellen Breitbandkühlung, welche diese Kühlmethode aufweist, ist in einer Vielzahl von Experimenten erstrebenswert. Der Anwendungsbereich der Technik erstreckt sich von der Kühlung in Experimenten mit Quantengasmikroskopen über die hier präsentierte Anwendung in Ionenfallen bis hin zur Kühlung von nanomechanischen Resonatoren. Im Bereich der Quanteninformationsverarbeitung stellt die Methode eine Verbesserung verglichen mit der üblicherweise genutzten Seitenbandkühlung dar: die überlegenen Kühleigenschaften erlauben eine Steigerung der Anzahl der Ionen welche an einer Berechnung teilnehmen was mit einer Steigerung der Rechenleistung des Quantencomputers gleichbedeutend ist. Somit ist die Anwendung von EIT Kühlung ein weiterer Schritt, damit Quantencomputer in der nahen Zukunft klassische Computer überflügeln können.

In einer segmentierten Mikrofalle wurden Daten zur wiederholten Anwendung der Seitenbandkühlung sowie zur Kühlung durch EIT für bis zu zwei Ionen gewonnen. Diese Daten deuteten auf die mögliche Breitbandkühlung durch die EIT Methode hin. Allerdings erschwerten systematische Instabilitäten der Mikrofalle eine Implementierung der Technik für lange Ionenketten. Aus diesem Grund

wurden zusätzliche Messungen mit Hilfe einer makroskopischen Paulfalle durchgeführt. Dies erlaubte die Charakterisierung der Kühlbandbreite und der Kühlrate gemessen mit Ionenketten von bis zu achtzehn Ionen.

Für mehrere gefangene Ionen führt die bereits erwähnte Coulomb Abstoßung zu einer Verteilung der Modenanregung über den gesamten Ionenkristall. Daher liefert die normalerweise für Einzelionen benutzte Methode zur Messung der Vibrationsanregung keine aussagekräftigen Resultate. Aus diesem Grund basieren die in dieser Arbeit präsentierten Ergebnisse auf einer neuen Technik zur Bestimmung der Anregung der Bewegungsmoden beruhend auf schnellen adiabatischen Passagen (RAP).

Contents

Abbreviations	xi
1 Introduction	1
2 Ion trapping in Paul traps	7
2.1 Ion trapping with radio-frequency fields	7
2.2 Ion motion within traps	11
2.2.1 Harmonic trapping potential	11
2.2.2 Anharmonic trapping potential	14
3 Atom-light interaction	19
3.1 Light coupling to trapped ions	19
3.1.1 Light coupling to a single trapped ion	20
3.1.2 Light coupling to a multi-ion crystal	23
3.2 Laser cooling	24
3.2.1 Doppler cooling	24
3.2.2 Sideband cooling	25
3.2.3 EIT cooling	28
3.3 Measuring motional states of trapped ions	32
3.3.1 Red-sideband and blue-sideband excitation	32
3.3.2 Motional-state dynamics on the blue sideband	35
3.3.3 Rapid adiabatic passage	36
4 The Microion-trap setup	43
4.1 The trap and vacuum setup	43
4.2 Laser setup	47
4.2.1 Photoionization lasers	48
4.2.2 Laser driving the $S_{1/2} \Leftrightarrow P_{1/2}$ transition	48
4.2.3 Laser driving the $S_{1/2} \Leftrightarrow D_{5/2}$ transition	52
4.2.4 Laser driving the $D_{3/2} \Leftrightarrow P_{1/2}$ transition	53
4.2.5 Laser driving the $D_{5/2} \Leftrightarrow P_{3/2}$ transition	54
4.2.6 System control and data accumulation	55
4.2.7 Introduction of the sample-and-hold stabilization	56
5 Multi-mode cooling in the Microion apparatus	61
5.1 Objectives for the Microion trap	61
5.2 Repetitive sideband cooling	63
5.2.1 Axial sideband cooling	63
5.2.2 Repetitive sideband cooling	65
5.3 EIT cooling of a two-ion crystal	67

5.3.1	EIT beam characterization	68
5.3.2	EIT cooling results	70
6	EIT cooling of long ion strings	77
6.1	The linear-trap setup	78
6.1.1	The linear ion trap and vacuum vessel	78
6.1.2	The laser setup	81
6.1.3	The EIT-cooling setup	83
6.2	Motional-state analysis	85
6.2.1	Single-ion heating rate	86
6.2.2	Dynamics of the blue-sideband transition	87
6.2.3	RAP to determine the mean phonon number	90
6.3	EIT cooling of a multi-ion crystal	99
6.3.1	Characterizing the EIT beams	99
6.3.2	EIT cooling results	103
7	Summary and outlook	109
A	Anharmonic trapping potentials	113
B	List of publications	117
C	List of datasets	119
	Bibliography	123

List of Figures

2.1	Schematics of RF traps	8
2.2	Stability diagram for a harmonic linear Paul trap	10
2.3	Equilibrium ion positions for a harmonic potential	13
2.4	Normal mode frequencies for a harmonic potential	14
2.5	Equilibrium ion positions for an anharmonic potential	16
2.6	Normal mode frequencies for an anharmonic potential	17
3.1	Two-level system interacting with light	20
3.2	Coupling of a harmonic oscillator with a two-level system	21
3.3	Sideband-cooling scheme and off-resonant heating processes	26
3.4	Steady-state population for sideband cooling	28
3.5	Transitions used for EIT	29
3.6	Line profile for EIT cooling	30
3.7	Steady-state population for EIT cooling	31
3.8	Rabi oscillations for varying mean phonon numbers	34
3.9	Global blue-sideband excitation of a two-ion crystal	35
3.10	Blue-sideband RAP for a three-ion crystal	38
3.11	Dicke-state generation with RAP	39
3.12	Red-sideband RAP for a three-ion crystal	40
4.1	Micreion trap schematic	44
4.2	Top-view schematic of the Micreion-trap vacuum vessel	46
4.3	Level scheme of $^{40}\text{Ca}^+$	47
4.4	Level scheme for state detection and optical pumping	48
4.5	Zeeman sublevels of $^{40}\text{Ca}^+$ used for EIT cooling	49
4.6	Optical setup for the laser at 397 nm	50
4.7	EIT beam alignment	51
4.8	Optical setup for the laser at 729 nm	52
4.9	Optical setup for the lasers at 854 nm and 866 nm	54
4.10	Rabi oscillation and population fluctuation over time	56
4.11	Sample-and-hold loop schematic	57
4.12	Improved Rabi oscillation and contrast fluctuation over time	58
5.1	Experimental sequence with sideband cooling	63
5.2	Axial heating rate for a single ion axially sideband cooled	64
5.3	Axial heating rate for a single ion repetitively sideband cooled	65
5.4	Radial heating rates for a single ion repetitively sideband cooled	66
5.5	EIT light-shift optimization	70
5.6	Experimental sequence with EIT cooling	71
5.7	EIT cooling results for a two-ion crystal	72

6.1	Schematic of the QSim trap	78
6.2	Schematic of the QSim vacuum setup	80
6.3	EIT cooling setup and EIT beam alignment	83
6.4	Experimental sequence with sideband cooling	85
6.5	Radial heating rates for a single ion	87
6.6	Global blue-sideband oscillations of a four-ion crystal	88
6.7	Phonon-state distribution for a global blue-sideband pulse-length scan	89
6.8	Fock-state preparation	91
6.9	Fock-state measurement using RAP	92
6.10	Fock-state measurement with red-sideband pulse length scan	94
6.11	Preparation of large Fock states using RAP	97
6.12	Nine-ion crystal heating-rate measurement with RAP	99
6.13	EIT polarization optimization	101
6.14	Measurement for EIT polarization optimization	102
6.15	EIT light-shift optimization	103
6.16	Measurement for EIT light-shift optimization	103
6.17	Experimental sequence with EIT cooling	104
6.18	Radial spectra of a nine-ion crystal without and with EIT cooling	105
6.19	Radial spectra of an eighteen-ion crystal without and with EIT cooling	106
6.20	EIT cooling dynamics for an eighteen-ion crystal	107
A.1	Electric field and potential for an equidistant ion string	114

Abbreviations

In the following, commonly used abbreviations are listed.

AC	alternating current
AOM	acousto-optic modulator
BS	beam splitter
COM	center of mass
DC	direct current
DPSS	diode-pumped solid-state
EIT	electromagnetically induced transparency
EMCCD	electron-multiplying charged-coupled device
EOM	electro-optical modulator
GND	ground
GUI	graphical user interface
IQOQI	Institute for Quantum Optics and Quantum Information
LBO	lithium triborate
NEG	non-evaporable getter
PBS	polarizing beam splitter
PD	photodiode
PDH	Pound Drever Hall
PID	proportional-integral-differential
PMT	photomultiplier tube
QSim	quantum simulation experiment
RAP	rapid adiabatic passage
RF	radio frequency
RGA	residual gas analyzer
RMSE	root-mean-square error
TA	tapered amplifier
Ti:Sa	titanium-sapphire laser

1

Introduction

The nature of light was heavily disputed within the physics community for several centuries. While Newton was convinced that light was a beam of particles, Huygens was not satisfied with this picture and considered light to have a wave-like character. Until the end of the 19th century, both experimental observations and Maxwell's equations, which allowed the description of light in terms of electromagnetic waves, supported Huygens' wave theory [1–3].

At the beginning of the 20th century, a turning point for the argument was reached as Planck formulated the *quantum hypothesis* to theoretically reflect experimental results on black body radiation [4]. In his *quantum hypothesis*, Planck postulated that the energy of electromagnetic waves of frequency ν could only occur in integer multiples of a discrete quantity $h\nu$, with h a newly introduced fundamental constant. Planck's findings together with experimental work on the photoelectric effect prompted Einstein to discern that the exchange of energy between light and matter is only possible in a discrete fashion. He summarized his considerations as the *light-quantum hypothesis* [5]. Both men were awarded the Nobel prize for their work, Planck in 1918 and Einstein in 1921. In 1926, the granules of energy $h\nu$, which constitute a beam of light, were labeled *photons* by Lewis [6].

The findings of Einstein, Planck and others described and fortified that light consists of photons. Thus, a new perspective on previously valid concepts had to be contemplated to accommodate the dual nature of light. Depending on the experimental setup, either the wave-like character or the granular nature of light play a major role to describe and interpret the experiment and its results: Classical interference experiments, as, for example, Young's double-slit experiment, clearly indicate the wave-like behavior based on a description with the electric field $E(\mathbf{r}, t)$ and corresponding intensities. However, a reduction of the incident light to an extent where single photons can be detected after the double-slit necessitates the consideration of the light's particle-nature. A statistical interpretation of the experimental outcomes based on multiple measurements taken under identical conditions is necessary to achieve a correct result.

In the 1920s, the wave-particle duality was extended to matter by de Broglie [7]. The goal of his considerations was to explain the discrete orbits of electrons circling a nucleus, which lead to the lines in atomic emission and absorption spectra. The experimental observation of electron diffraction by Davisson and Germer supported the theory that "solid" particles could also exhibit wave-like behavior [8]. de Broglie received the Nobel prize in 1929 and Davisson in 1937.

As for the wave-particle duality of light, the different aspects of matter take effect dependent on the experiments conducted and a statistical interpretation of repetitive measurements is necessary. In addition, the term *quantum mechanics* was coined to refer to quantized processes, which happen in multiples of Planck's constant.

The interaction of light and matter on this new theoretical base was subject to intense studies leading, amongst others, to the research field of *quantum optics*. *Quantum optics* is concerned with the interaction of light and matter on a single quantum scale. The investigations in this field are based on *semiclassical* as well as quantum mechanical approaches. The *semiclassical* considerations take into account a classical description of light as an electromagnetic wave interacting with matter, for example, a single atom, which is described quantum-mechanically. In addition, quantum optics focuses on processes involving light of low intensities with a countable number of photons, calling for a quantization of the light field.

One process that has been studied in the field of quantum optics using mostly semiclassical approaches is laser cooling. Although the force exerted by radiation had been considered and demonstrated before, it was the invention of the laser in 1960 [9] that enabled the experimental use of this effect to cool matter with light [10].

The concept of laser cooling is based on energy and momentum conservation related to the absorption and subsequent spontaneous emission of a photon by a particle. The absorption process happens with photons possessing an energy that (nearly) corresponds to the transition energy of two internal states of an atom. The photon absorption results in an atomic recoil that always has the same direction. However, the spontaneous emission process following the absorption causes atomic recoils in random directions. Therefore, the momentum transfer, i.e., the averaged recoils, cancels over time, thus effectively slowing the atom. Application of laser cooling to samples of neutral atoms [10, 11] and ions [12, 13] showed the method's ability to provide cooling with light into the milli- and micro-Kelvin regime and below.

Laser cooling applied to confined particles can be used to generate samples of cold dense atomic clouds. In addition, the application of the method to trapped particles enables cooling of said particles into their quantum mechanical ground state [14, 15]. These are just two examples that demonstrate the excellent control over the atoms' and ions' motional degrees of freedom achieved with laser cooling. As a result, laser cooling has become a standard tool in the quantum optics toolbox used in various fields such as atom interferometry [16], atomic clocks [17, 18], ultra-cold quantum gases [19] and quantum information processing with ions [20] and atoms [21].

While the minimum temperature achieved is certainly an important figure of merit for any cooling scheme, other characteristics need to be considered as well. Depending on the field of application, laser cooling has to satisfy varying requirements. For example, it is important to detail the range of initial temperatures for which the cooling method can be used as well as the expected cooling rate. For the application with trapped particles, it is also of importance how many motional modes of the system can be cooled simultaneously. Thus, since Doppler cooling

was first implemented, a number of more sophisticated schemes have emerged to meet the challenges due to specific applications [12, 13, 22].

One of these applications is quantum information processing. Since the 1980s, the properties emerging from quantum mechanics, like superposition of particle states and entanglement, have been under discussion as a means to improve classical Turing machines [23–25]. As early as the mid 1990s, a number of quantum algorithms had been proposed, driving the search for physical realizations of such quantum computing systems [26–30].

One distinctive difference between a classical computer and a quantum computer lies in the physical representation of the smallest unit to perform computations: while in a classical computer, so-called “bits” can represent information as 0 or 1, the quantum bits (“qubits”) a quantum computer relies on are able to exist in a superposition of these states. Quantum bits can thus represent information not only as $|0\rangle$ or $|1\rangle$, but more generally as $\alpha|0\rangle + \beta|1\rangle$, with α and β being complex coefficients fulfilling the normalization condition $|\alpha|^2 + |\beta|^2 = 1$. This representation allows the use of quantum mechanical effects like entanglement to increase the computing power of a quantum computer beyond that of a classical computer [31].

Whichever physical system is used to implement a quantum computer, the criteria introduced by DiVincenzo [32] serve to consider the conditions necessary for a successful implementation. These can be summarized as follows:

- (i) The quantum bit needs to be *well-defined* and implemented in a scalable physical system. *Well-defined* refers to the ability to encode a two-level system and to know the sources and the strength of internal and external interactions.
- (ii) The *initialization* of a specific quantum-bit input state has to be achievable. *State initialization* refers to a deterministic preparation of the register’s input state, for example, in the state $|00\dots 0\rangle$.
- (iii) A method to read out the state of the quantum bit ($|0\rangle$ or $|1\rangle$) after the calculation has been executed has to exist.
- (iv) The physical realization of the quantum bit has to exhibit *coherence times* that are longer than the time taken up by the computation. The system’s *coherence time* for a single quantum bit gives the span during which the information described by the superposition state $|\psi\rangle = \alpha|0\rangle + \beta|1\rangle$ is preserved despite interaction with the environment.
- (v) A universal set of quantum gate operations has to be established for the system. The realization of arbitrary gate operations can be factorized into single quantum bit rotations and entangling-gate operations.

Trapped atomic ions represent one very promising candidate to realize a quantum computer with the quantum bit being encoded in two internal electronic states of the ion [31, 33]. Two different quantum-bit realizations based on trapped ions have been explored:

- (i) Zeeman or hyperfine sublevels of two electronic ground states with a transition frequency of a few gigahertz can be used for quantum bit implementation [34]. The quantum state can thus be manipulated directly

using microwaves. However, the application of two far-off-resonant lasers to drive a two-photon Raman transition can be applied for state manipulation as well [34, 35].

- (ii) An electronic ground state and a metastable excited state with a transition frequency of a few hundred terahertz can be used for the quantum bit implementation [36]. The quantum state can thus be manipulated using waves provided by lasers.

Both initialization and readout of the target state are available with high efficiency (>99 %) for trapped atomic ions [37]. The natural lifetime of the excited state sets an upper bound for the achievable coherence time. This is dependent on the ion species used in the experiment. However, experimental conditions like the stability of magnetic fields and fluctuations of interacting laser fields influence this parameter [38]. For $^{40}\text{Ca}^+$, a coherence time of approximately 100 ms could be achieved [37, 38].

The information exchange across a quantum register is based on entanglement of the trapped ions. This entanglement is mediated via the collective motional mode of the ions due to their shared harmonic trapping potential and is induced by electromagnetic waves. These waves are often in the infrared to ultraviolet regime and generated by laser sources due to the well established coherent manipulation based on this approach [39]. However, it is also possible to mediate entanglement using microwaves [40–42].

In order to apply gate operations between the ions within a register, it is necessary to precisely control the motional modes. Such a control can be achieved using laser-cooling methods. Thus, the interaction of trapped ions and electromagnetic waves is at the core of an ion based quantum computer, as it not only allows the information to be written onto single quantum bits, but it is also used to implement entangling-gate operations.

The first two-qubit gate operation applied to entangle trapped ions was a controlled-NOT gate operation [28, 35, 43]. This so-called CZ-gate operation requires the motional mode used for the implementation to be cooled to its vibrational ground state. However, gate operations based on spin-dependent forces, which are nowadays widely used to mediate entanglement, work under less stringent conditions [44–46]. These gate operations are able to provide entanglement even for a thermal state and only require cooling of the vibrational state of the mode into the Lamb-Dicke regime. Nonetheless, their performance has been shown to improve with decreasing vibrational excitation of the motional mode [47].

Techniques that achieve cooling of the motional mode to its ground state include sideband cooling [14] and Raman sideband cooling [35]. While sideband cooling relies on a narrow atomic transition like a quadrupole transition, Raman sideband cooling works through the application of far-off-resonant lasers to broad transitions like dipole transitions. For both of these techniques an initial cooling step is necessary to ensure that the ions are already in the Lamb-Dicke regime.

An alternative approach is cooling by [electromagnetically induced transparency \(EIT\)](#) [48]. EIT requires a three-level system and uses quantum interference ef-

fects to suppress unwanted heating due to spontaneous emission. The frequency range over which motional modes are cooled to their ground state is wider for EIT cooling than for Raman sideband cooling or for sideband cooling, and the achieved cooling rates are higher. However, the final temperature of the system is also higher than for those schemes.

Surveying the cooling behavior of these three ground-state cooling techniques, it can be inferred that while the CZ controlled-NOT gate operation relies on cooling by sideband cooling or Raman sideband cooling, gate operations based on spin-dependent forces can be combined with cooling using EIT. A first experimental demonstration of EIT cooling was executed using a single trapped ion [49]. However, the method has recently attracted more attention with applications to small ion crystals [50], a quantum gas microscope [51], neutral atoms in a cavity-QED setup [52], and a nanomechanical resonator [53].

In ion trap quantum computers, scalability consists of being able to increase the number of ions provided as quantum resources without compromising gate fidelities. However, with more ions trapped in a common potential, the mode-spectrum density also increases. For the reliable application of entangling-gate operations for so many ions, it is necessary to provide a cooling scheme that works quickly and efficiently on a large number of modes. Therefore, the combination of spin-dependent-force entangling-gate operations with EIT cooling represents one plausible route to a scalable ion trap quantum computer.

This thesis presents the implementation of multi-mode cooling techniques for trapped $^{40}\text{Ca}^+$ ions. These ions serve as the basis for a quantum computer. The quantum bits are encoded in the Zeeman sublevels of the $S_{1/2} \Leftrightarrow D_{5/2}$ transition with an upper state lifetime of 1.16s [54]. $^{40}\text{Ca}^+$ is a good choice for the task at hand, as its internal level structure provides closed cycles for Doppler cooling, manipulation and state detection. The experiments presented have been carried out using two different trap geometries: a segmented, microfabricated trap in which the axial potential can be tailored, and an unsegmented macroscopic linear Paul trap with a harmonic axial potential. The microtrap (which is referred to as the “Mitreon” trap in this thesis, after the company which fabricated it) offers the possibility of generating anharmonic potentials to create trapping sites next to one another [55, 56] or to confine equidistant strings of ions [57]. With the macroscopic linear trap, investigations with long strings of ions were executed. In both setups, cooling of multiple modes of motion has been investigated. While in the Mitreon setup repetitive sideband cooling and EIT cooling have been integrated, the focus in the linear trap setup was on EIT cooling of long strings of ions. In addition, [rapid adiabatic passage](#) and global blue-sideband excitations were introduced as novel techniques to study the vibrational excitation of a mode in multi-ion crystals.

This work summarizes the theoretical concepts of ion trapping in Ch. 2 and the interaction between trapped particles and light in Ch. 3. The setup of the Mitreon trap apparatus is presented in Ch. 4, and the results obtained with this trap are summarized in Ch. 5. Ch. 6 gives insights on the macroscopic linear-trap setup and details results concerning multi-mode cooling in long strings of ions. A summary of the findings and an outlook for the future development of the projects

can be found in Ch. 7.

2

Ion trapping in Paul traps

All experiments presented in this thesis rely on the ability to confine charged particles at a well-defined location and shield them from unwanted interactions with their environment. These conditions can be achieved in so-called Paul traps [58, 59]. The working principle of such devices dates back to the 1950s, when Wolfgang Paul and associates introduced a two-dimensional quadrupole potential generated by **radio frequency (RF)** fields for mass spectrometry [59]. Since that early work, a steadily increasing number of applications ranging from collision measurements with various constituents [60, 61], to metrology [62, 63], and continuing to quantum information processing [33, 37] have proven the usefulness and versatility of these traps. Even today, new designs and variations of the “classic” Paul apparatus are being invented to satisfy various emerging experimental requirements [59, 64, 65].

In this chapter, an introduction to trapping in Paul traps is given. A summary of the working principles of Paul traps in Sec. 2.1 is followed by a presentation concerning the motion of trapped ions within their confining potential in Sec. 2.2. The reader is referred to the literature for more comprehensive information on the state of the art in Paul traps [59, 64, 66].

2.1 Ion trapping with radio-frequency fields

In an attempt to increase the number of ions available as quantum resources, numerous novel trap designs have been invented [67]. However, the basic considerations for the potentials generated and the ion motion within the trap can be traced back to the basic Paul trap design. The linear Paul trap is a trap configuration which has been a workhorse in the field of quantum information processing over the past twenty years [68]. Fig. 2.1(a) shows the schematics for one type of linear Paul trap, a so-called blade trap. This type of trap consists of four blade-shaped electrodes and two so-called endcap electrodes. The application of **RF** voltage to two opposing blade electrodes while the other two are held at ground provides radial confinement of the ions. The application of **direct current (DC)** voltage to the endcap electrodes provides axial confinement of the ions.

Additionally, Fig. 2.1(b) shows a segmented ion trap. Such trap types emerge from a segmentation of the RF-ground electrodes, enabling the application of different **DC** voltages to electrode segments and using this configuration to provide axial confinement.

So far, up to fourteen ions have been successfully entangled in a single harmonic potential generated by a blade trap [69]. However, the segmentation of electrodes allows the creation of multiplexing architectures and pushes the versatility of the generated axial confinement beyond single harmonic potentials [34, 67]. Segmented traps enable shuttling of ions between individual trapping sites thus making it possible to increase the number of the quantum bits involved in a computation. Furthermore, higher-order axial potentials like double-well potentials or quartic potentials can be realized [55, 56]. The latter can be used to generate large strings of uniformly spaced ions, a configuration that simplifies the stabilization of a linear crystal structure [57].

For the measurements presented in this work, both a segmented trap and a blade trap have been used to execute measurements. Details on the setup incorporating the segmented trap and the results obtained with it can be found in Ch. 4 and Ch. 5. Ch. 6 summarizes the setup and measurements carried out with the blade trap.

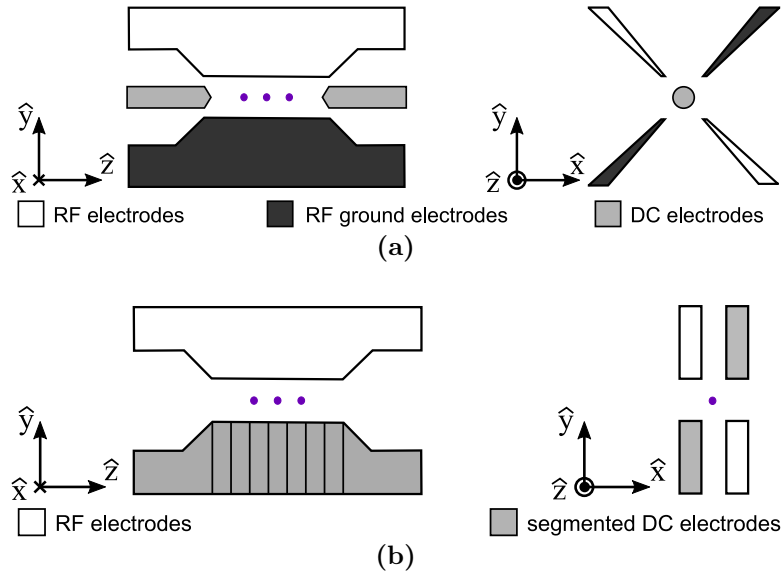


Figure 2.1. RF traps in front projection and side projection. (a) In a blade-type linear Paul trap, ions are trapped in the center region along the direction of the z -axis. Radial confinement is provided by an RF voltage applied to opposing blade-shaped electrodes. A DC voltage applied to the endcap electrodes supplies axial confinement. (b) In a two-layer segmented trap, ions are trapped in the center region along the direction of the z -axis. Radial confinement is provided by an RF voltage applied to opposing electrodes. A DC voltage applied to two segmented electrode pairs supplies axial confinement.

The potential confining the ions within a trap is a superposition of a time-varying radial (x,y -axis) quadrupole potential and a static axial (z -axis) harmonic potential. The radial confinement is generated by applying an RF voltage of amplitude V_0 (0 - peak), and frequency Ω_{RF} to two opposing blade electrodes. This forms a quadrupole potential which under certain conditions which are discussed below can be made to be confining on time average. For a linear Paul trap, the axial confinement is generated by applying a static voltage, U_{DC} , to the so-called endcap electrodes. The total potential near the trap center is approximately a

2.1. Ion trapping with radio-frequency fields

quadrupole potential, which can be expressed as [70]

$$\Phi(x, y, z, t) = \underbrace{\frac{U_{\text{DC}}}{\tilde{r}^2}(\alpha_x x^2 + \alpha_y y^2 + \alpha_z z^2)}_{\text{static potential}} + \underbrace{\frac{V_0}{\tilde{r}^2} \cos(\Omega_{\text{RF}} t)(\beta_x x^2 + \beta_y y^2 + \beta_z z^2)}_{\text{oscillating potential}}, \quad (2.1)$$

with \tilde{r} the minimum distance between the trap axis (z axis) and the surface of the electrodes, and with α_k and β_k multiplicative constants, $k = x, y, z$.

As the potential (Eq. 2.1) has to fulfill the Laplace equation, $\Delta\Phi = 0$, the constants have to satisfy the constraints $\alpha_x + \alpha_y + \alpha_z = 0$ and $\beta_x + \beta_y + \beta_z = 0$. In the case of a linear Paul trap, these conditions can be specified to be

$$\begin{aligned} -(\alpha_x + \alpha_y) &= \alpha_z > 0, \\ \beta_x &= -\beta_y, \\ \beta_z &= 0. \end{aligned} \quad (2.2)$$

Within the trap, the three-dimensional motion of one singly charged particle can then be inferred from the equations of motion¹, which yield

$$\frac{d^2 u_k}{d\zeta^2} + (a_k - 2q_k \cos(2\zeta)) u_k = 0, \quad (2.3)$$

with the substitution

$$a_k = \frac{4|e|U_{\text{DC}}\alpha_k}{m\Omega_{\text{RF}}^2\tilde{r}^2} \quad q_k = \frac{2|e|V_0\beta_k}{m\Omega_{\text{RF}}^2\tilde{r}^2} \quad \Omega_{\text{RF}}t = 2\zeta. \quad (2.4)$$

In Eq. 2.4, m denotes the trapped particle's mass, and $|e|$ the elementary charge. Eq. 2.3 represents the standard form of the Mathieu differential equations, which exhibit stable and unstable solutions. For a linear Paul trap with typical experimental parameters of $q_x = -q_y$, $q_z = 0$ and $|a_k| \ll 1$, the stability diagram is shown in Fig. 2.2.

With these experimental parameters, the ion trajectory within the confining potential can be inferred from a first-order approximation of the full solution for the Mathieu equations (Eq. 2.3). This lowest-order approximation can be written as

$$u_k(t) \approx \underbrace{u_{1k} \cos(\omega_k t + \phi_k)}_{\text{secular motion}} \underbrace{\left(1 + \frac{q_k}{2} \cos(\Omega_{\text{RF}} t)\right)}_{\text{micromotion}}, \quad (2.5)$$

with ϕ_k a phase, and u_{1k} an amplitude, both of which are dependent on the initial conditions of the system. Here, a secular motional frequency ω_k has been introduced, which can be approximated as

$$\omega_k \cong \frac{\Omega_{\text{RF}}}{2} \sqrt{a_k + \frac{q_k^2}{2}}. \quad (2.6)$$

¹ $\mathbf{F} = m\ddot{\mathbf{r}} = -|e|\nabla\Phi$

with \mathbf{F} the force, m the particle mass, $\ddot{\mathbf{r}}$ the acceleration, $|e|$ the elementary charge, and ∇ the nabla operator.

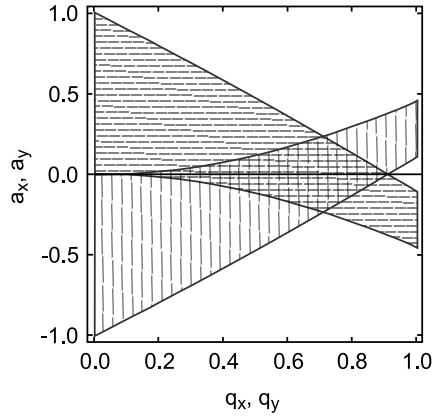


Figure 2.2. Stability diagram for a harmonic linear Paul trap. The solutions for the equations of motion in x direction (horizontally hatched area) and y direction (vertically hatched area) mirror each other. The overlap between the hatched areas corresponds to the conditions that can be used to trap particles.

For details on the derivation see references [64, 70]. The solution, as presented in Eq. 2.5, exhibits two different sets of motion.

The *secular oscillation* is a harmonic motion. It corresponds to the motion a particle would undergo if trapped in the center of a harmonic trapping potential, the so-called *pseudopotential* [64, 70, 71]. Secular motion is slow compared to the driving frequency Ω_{RF} .

In addition, Eq. 2.5 introduces fast *micromotion*. This oscillation is coherently driven by the **radio frequency** and out of phase with it by 180° . At the RF null, a trapped particle exhibits no micromotion. However, a non-zero static electric field can shift the trapped particle away from the RF null, leading to micromotion with an increasing amplitude the farther the ion is shifted. This excess motion causes a broadening of the transition linewidth, reduces the cooling efficiency and introduces a second-order Doppler shift [72]. It can also lead to heating by mixing RF noise to the ion’s motional frequency [73]. For multi-ion crystals, parametric coupling between the secular motion and the micromotion can occur, leading to a reduction of the cooling efficiency and, if no cooling method is applied, a reduction of the ion lifetime in the trap [72, 74]. Therefore, it is necessary to shift the ion back to the RF null by applying additional DC voltages, known as “compensating” for the micromotion [71].

In a linear Paul trap, such as the blade trap in Fig. 2.1(a), $q_z = 0$ and no RF confinement is generated along the trap axis. This leads to the suppression of micromotion along the z -axis, which is an advantage that linear Paul traps have over Paul traps with three-dimensional RF confinement [72]. In segmented ion traps, however, the miniaturization and fabrication process often leads to an additional unwanted micromotion component along the trap axis.

Axial particle confinement in a linear trap arises from the applied DC potential. The equation of motion in this direction can be inferred from Eq. 2.3 to give a harmonic motion as well. An attenuation of the radial confining potential due to the defocusing effect of the DC voltage, U_{DC} , applied to the endcap electrodes

2.2. Ion motion within traps

can be observed [75]. As denoted in Eq. 2.6, the defocusing leads to a reduction of the secular trap frequencies in the radial direction².

2.2 Ion motion within traps

For a single ion trapped in a harmonic potential generated by an RF trap, Eq. 2.5 describes the motion in all three spatial dimensions with the corresponding frequencies given in Eq. 2.6. For a linear trap, the multiplicative constants obey Eq. 2.2. However, as soon as more ions are loaded into the trapping region, the Coulomb interaction between the charged particles has to be taken into account. This interaction leads to three additional motional frequencies per added ion.

In linear Paul traps, the confinement close to the trap center is, to a good approximation, harmonic and anharmonicities of higher order are dealt with as perturbations [76]. Since the harmonic trapping potential is the simplest case, it will first be introduced in Sec. 2.2.1 to illustrate the methods used to determine the ion positions and mode frequencies.

The segmentation of a trap's DC electrodes was initially envisioned to achieve scalability through having multiple, reconfigurable trapping minima [34, 67]. In addition to this, the segmented electrodes offer the possibility to shape the axial confining potential. Strong anharmonic terms are advantageous to trap a large number of ions in a more stable fashion [57]. The additional terms should have even symmetry. So the first, and simplest, higher-order term, which can be added, is a quartic term. Sec. 2.2.2 introduces a quartic trapping potential with the resulting ion positions and motional frequencies.

2.2.1 Harmonic trapping potential

Trapped ions align themselves linearly provided the radial frequencies $\omega_{x,y}$ are sufficiently high relative to the axial frequency ω_z [77]. This is the case for trap frequencies satisfying the inequality [78, 79]

$$\frac{\omega_{x,y}}{\omega_z} > 0.77 \frac{N}{\sqrt{\log N}}. \quad (2.7)$$

Hence, the minimum ratio between $\omega_{x,y}/\omega_z$, for which ions can be confined in a one-dimensional string, depends on the number of ions, N .

A string of N ions trapped in a harmonic potential has a potential energy of

$$U(x, y, z, t) = \underbrace{\frac{m}{2} \sum_{i=1}^N (\omega_x^2 x_i^2(t) + \omega_y^2 y_i^2(t) + \omega_z^2 z_i^2(t))}_{\text{effective harmonic potential}} + \underbrace{\frac{1}{2} \frac{e^2}{4\pi\epsilon_0} \sum_{\substack{j,i=1 \\ j \neq i}}^N \frac{1}{|\mathbf{r}_i(t) - \mathbf{r}_j(t)|}}_{\text{Coulomb potential}}, \quad (2.8)$$

²Note that the parameters a_x, a_y are negative.

Chapter 2. Ion trapping in Paul traps

with m the ion mass, ω_k the secular motional frequency in the $k = x, y, z$ direction, e the elementary charge, ϵ_0 the vacuum permittivity, and $\mathbf{r}_i = (x_i, y_i, z_i)$ the position vector of the i th ion. Eq. 2.8 consists of the total effective harmonic trapping potential generated by the applied voltages and the Coulomb potential created by the interaction of each ion with every other ion.

If the energy due to Coulomb repulsion is larger than the kinetic energy of the ions, their time dependent position can be approximated by [80]

$$\mathbf{r}_i(t) \approx \mathbf{r}_i^0 + \mathbf{q}_i(t), \quad (2.9)$$

dividing the trajectory into a stationary part in equilibrium, \mathbf{r}_i^0 , and a time-dependent fluctuating term, $\mathbf{q}_i(t)$. If the inequality Eq. 2.7 is satisfied, a linear crystal forms along the z -axis with the equilibrium position of the i th ion given by $(x_i^0 = 0, y_i^0 = 0, z_i^0)$. The linear shape of the crystal simplifies the calculation by decoupling the potential in the spatial dimensions. Solutions for the ions' equilibrium positions, z_i^0 , can be calculated by considering the derivative of the potential,

$$\left[\frac{\partial U}{\partial z_i} \right]_{z_i=z_i^0} = 0. \quad (2.10)$$

Eq. 2.10 can be expressed as a set of N coupled algebraic equations [80]. The analysis of these equations can be greatly simplified by introducing a length scale, l , and a dimensionless position, u_i , for the i th ion defined as

$$u_i = \frac{z_i^0}{l}, \quad l = \left(\frac{e^2}{4\pi\epsilon_0 m \omega_z^2} \right)^{1/3}. \quad (2.11)$$

Using the new variables allows analytical solutions to be derived from the coupled equations for an ion number of up to $N = 3$, but numerical analysis is necessary for larger ion numbers.

The solutions for up to eighteen $^{40}\text{Ca}^+$ ions confined in a harmonic potential with an axial frequency of $\omega_z = 2\pi \times 0.21$ MHz are shown in Fig. 2.3. The chosen frequency value is taken from experimental settings introduced in Ch. 6 for an eighteen-ion crystal. The calculated positions presented in Fig. 2.3 illustrate that with larger particle numbers confined in the harmonic trapping potential, the innermost ions get pushed closer together by the outer ions. This relation between the number of ions and minimum inter-ion distance can be expressed as [79]

$$z_{\min}(N) = \left(\frac{e^2}{4\pi\epsilon_0 m \omega_z^2} \right)^{1/3} \frac{2}{N^{0.57}}. \quad (2.12)$$

After the equilibrium positions for the ions are calculated, the fluctuations around them have to be considered using the Lagrange formalism $L = T - U$, with T the kinetic energy of the system, and U its potential energy. For the system at hand, N ions trapped in a harmonic potential, the Lagrangian can be

2.2. Ion motion within traps

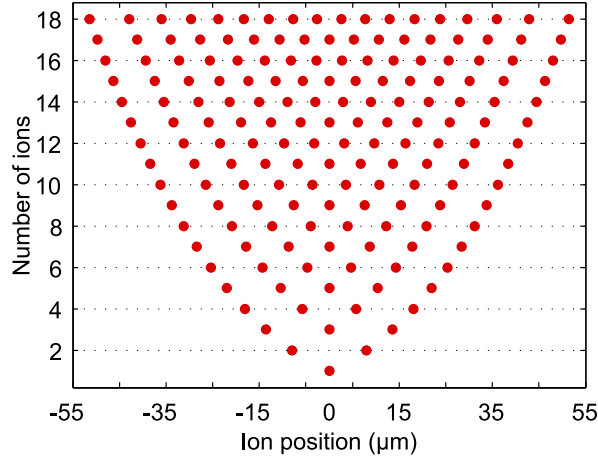


Figure 2.3. Equilibrium positions for up to eighteen $^{40}\text{Ca}^+$ ions trapped in a harmonic potential with an axial frequency of $\omega_z = 2\pi \times 0.21$ MHz. The non-uniformity of the spatial distribution is visible for larger ion numbers: the distance between the innermost nearest-neighbors is smaller than the distance between outer nearest-neighbor ions.

expressed as [75, 80, 81]

$$L = \frac{m}{2} \sum_{k=x,y,z} \left(\sum_{i=1}^N (\dot{q}_{k|i}^2) - \omega_z^2 \sum_{j,i=1}^N A_{j,i}^k q_{k|i} q_{k|j} \right), \quad (2.13)$$

with the coupling matrix (also called the Hessian matrix), $A_{i,j}^k = \frac{\partial^2 U}{\partial k_i \partial k_j}$, in the spatial dimensions $k = x, y, z$. The notation $q_{k|j}$ refers to the displacement of the j th ion from its equilibrium position in the $k = x, y, z$ direction, respectively.

Along the trap axis (z direction), the coupling matrix can be written as [75, 80, 82]

$$A_{i,j}^z = \begin{cases} 1 + 2 \sum_{\substack{p=1 \\ p \neq i}}^N \frac{l^3}{|z_i - z_p|^3} & \text{if } j = i, \\ \frac{-2l^3}{|z_i - z_j|^3} & \text{if } j \neq i. \end{cases} \quad (2.14)$$

The expression in Eq. 2.14 is also part of the definition for the coupling matrix in the x direction and the y direction [75, 82],

$$A_{i,j}^{x,y} = \left(\left(\frac{\omega_{x,y}}{\omega_z} \right)^2 - \frac{1}{2} \right) \delta_{i,j} - \frac{1}{2} A_{i,j}^z, \quad (2.15)$$

with the Kronecker delta $\delta_{i,j}$. The N eigenmodes in the axial direction can be derived by diagonalizing the coupling matrix presented in Eq. 2.14. For the $2 \times N$ eigenmodes in the radial directions, the same procedure is applied to the coupling matrices in Eq. 2.15.

Fig. 2.4 presents axial motional frequencies (Fig. 2.4(a)) and radial motional frequencies (Fig. 2.4(b)) for up to ten $^{40}\text{Ca}^+$ ions confined in a harmonic trapping potential with center of mass (COM) frequencies of $\{\omega_x, \omega_y, \omega_z\} = 2\pi \times \{2.71, 2.68, 0.21\}$ MHz. These values for the frequencies correspond to experimental settings in Ch. 6: the axial COM mode frequency, ω_z , is fixed to achieve

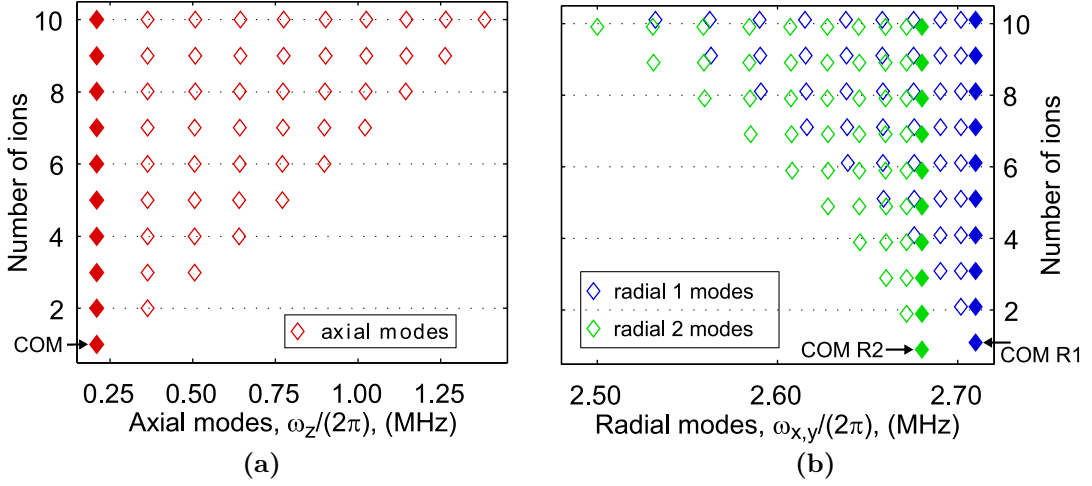


Figure 2.4. $3 \times N$ normal modes in the axial and radial directions for up to ten $^{40}\text{Ca}^+$ ions confined in a harmonic trapping potential with trap frequencies of $\{\omega_x, \omega_y, \omega_z\} = 2\pi \times \{2.71, 2.68, 0.21\}$ MHz. (a) All N axial motional frequencies. (b) All $2 \times N$ radial motional frequencies. The frequencies of the radial 1 modes (radial 2 modes) are slightly shifted up (down) around the corresponding number of ions, to allow a clearer presentation of the values.

a predetermined ion-ion distance (Eq. 2.11) by applying the corresponding DC voltage; the radial COM mode frequencies, ω_x and ω_y , are set to allow a linear crystal configuration (Eq. 2.7) by correctly adjusting the amplitude value of the RF voltage. The axial COM mode sets a lower bound on the frequency range and does not change with increasing ion number. All higher-order modes along the axial direction appear at higher frequencies. The radial COM modes set an upper bound on the frequency range and also do not change with increasing ion number. All higher-order modes along the transverse directions occur at lower frequencies. In comparing Fig. 2.4(a) and Fig. 2.4(b), it can be seen that the radial motional modes are spread out over a frequency range of 0.21 MHz, which corresponds to approximately 18% of the frequency range covered by the axial mode spectrum.

2.2.2 Anharmonic trapping potential

An ion trap with segmented DC electrodes can generate a confining potential using higher-order multipoles [83]. With such a setup it is possible to tailor a potential and create, for example, a double-well potential to store ions in neighboring potential minima [55, 56]. It is also possible to find voltage configurations that allow the trapping of a uniformly spaced ion crystal [57, 84]. The equal spacing of the ion crystal in an anharmonic potential has advantages compared to the bunching of the inner ions in a harmonic potential (Fig. 2.3): it offers a higher stability of the linear structure with increasing crystal size [57]. This can be seen by comparing Eq. 2.7 with the condition for a linear structure in an anharmonic potential, given by [57, 85]

$$\omega_{x,y}^2 > \frac{7\zeta(3)e^2}{2md_0^3} \approx \frac{4.2e^2}{md_0^3}, \quad (2.16)$$

2.2. Ion motion within traps

with d_0 the inter-ion distance and $\zeta(3)$ the Riemann zeta function.

In view of the benefits an equidistant ion crystal offers, it is interesting to consider the details of its implementation. A qualitative presentation is given here and a more detailed description can be found in App. A. Starting from a uniformly spaced ion chain, the external electric field necessary to create such a structure can be calculated. Integration of the field yields the potential, which can be expanded as a power series. This step facilitates the implementation of the necessary voltages using segmented ion traps. Because the power series is truncated and higher-order expansion terms are neglected, a deviation between the ideal case with perfect equidistant spacing and the real case is expected.

As described in reference [57], the use of five neighboring electrode segments allows the generation of a quartic potential along the z -axis. Such a confining potential gives the following expression for the total potential energy of an N -ion chain,

$$\begin{aligned}
 U(x, y, z, t) = & \underbrace{\sum_{i=1}^N \left[\frac{m}{2} \left(\omega_x^2 x_i^2(t) + \omega_y^2 y_i^2(t) \right) + \frac{\kappa_2}{2} z_i^2(t) + \frac{\kappa_4}{4} z_i^4(t) \right]}_{\text{effective quartic potential}} \\
 & + \underbrace{\frac{1}{2} \frac{e^2}{4\pi\epsilon_0} \sum_{\substack{j=1 \\ j \neq i}}^N \frac{1}{|\mathbf{r}_i(t) - \mathbf{r}_j(t)|}}_{\text{Coulomb potential}}, \tag{2.17}
 \end{aligned}$$

with $\omega_{x,y}$ the COM frequencies in radial direction, and κ_2 and κ_4 parameters determined by the applied DC voltages. The implementation of higher-order terms in the axial potential would allow the spacing between neighboring ions to be more uniform, but at the cost of involving a larger number of electrode pairs. Furthermore, for electrode segments with an axial extent much larger than the ion crystal's length, higher-order terms of significant influence can only be achieved with increasing voltage values. Thus, depending on the trap geometry, the realization of such potentials is impossible, if the necessary DC voltages lie in a regime, where damage to the trap cannot be prevented.

In the segmented trap presented in this thesis, the trap geometry precludes the generation of higher-order terms beyond a quartic coefficient. In general, a quartic potential provides a reasonable trade-off between the necessary experimental effort versus the uniformity of the ion chain. The techniques and insights developed in this first realization of an anharmonic potential can later be applied to systems with higher-order anharmonic terms.

A similar treatment as for the harmonic potential, described in Sec. 2.2.1 and in references [80, 81], can be applied to the anharmonic potential: A linearization of the time-dependent ion trajectory is carried out (see Eq. 2.9), consisting of a stationary equilibrium part and a time-dependent fluctuation. The equilibrium position of the i th ion within a linear crystal of N ions is given by $\{0, 0, z_i^0\}$. These positions can be calculated along the trap axis from a set of N coupled equations using dimensionless coordinates $\{0, 0, v_i^0\}$ given by

$$\begin{aligned}
 v_i &= \frac{z_i^0}{b}, \\
 b &= \left(\frac{e^2}{4\pi\epsilon_0\kappa_2} \right)^{1/3}, \\
 B &= \frac{\kappa_4}{\kappa_2} b^2 = \frac{\kappa_4}{\kappa_2} \left(\frac{e^2}{4\pi\epsilon_0\kappa_2} \right)^{2/3}.
 \end{aligned} \tag{2.18}$$

Eq. 2.18 introduces the length scale b , and the dimensionless ratio B , used to characterize and optimize the potential along the trap axis. Further details about the calculations can be found in App. A.

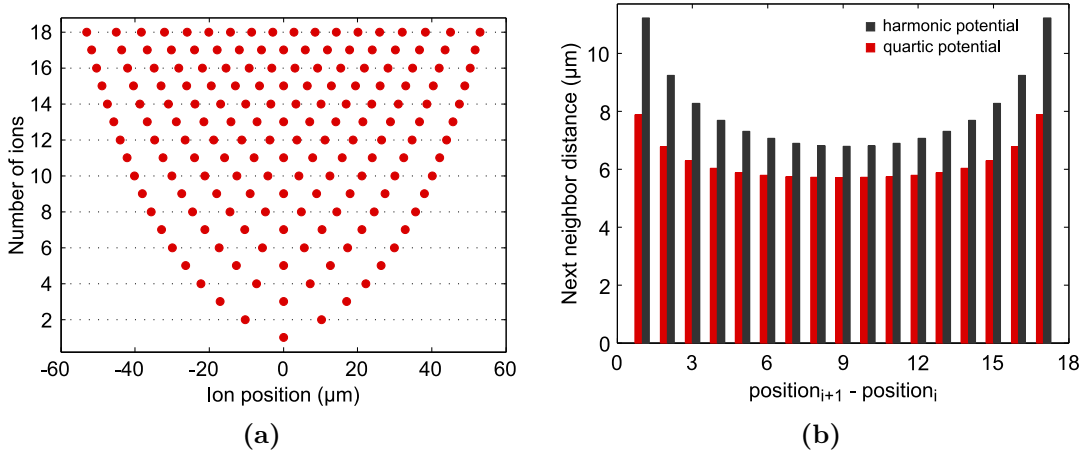


Figure 2.5. Equilibrium positions within an anharmonic potential and comparison to the corresponding harmonic trapping potential for up to eighteen $^{40}\text{Ca}^+$ ions. (a) The anharmonic trapping potential has parameters of $\kappa_2 = 5.04 \times 10^{-14} \text{ J m}^{-2}$ and $\kappa_4 = 2.66 \times 10^{-5} \text{ J m}^{-4}$. (b) Comparison of the equilibrium positions for an anharmonic potential and a harmonic potential with an axial frequency of $\omega_z = 2\pi \times 0.138 \text{ MHz}$ related to the value for κ_2 in (a).

With Eq. 2.18 it is possible to derive the equilibrium positions of the ions. They are dependent on the constants κ_2 and κ_4 , which can be determined from an analysis of the electric field produced by voltages applied to the DC electrodes. However, κ_2 also determines the secular COM mode frequency along the trap axis as $\omega_z = \sqrt{|\kappa_2|/m}$. This therefore poses an additional constraint on the chosen voltage values.

Fig. 2.5(a) presents the equilibrium positions for up to eighteen $^{40}\text{Ca}^+$ ions confined by a quartic potential with $\kappa_2 = 5.04 \times 10^{-14} \text{ J m}^{-2}$ and $\kappa_4 = 2.66 \times 10^{-5} \text{ J m}^{-4}$. The axial COM frequency for a $^{40}\text{Ca}^+$ ion trapped in a harmonic potential determined with the κ_2 parameter is $\omega_z = 2\pi \times 0.138 \text{ MHz}$. The harmonic and quartic parameters are those that would be required for a chain of eighteen uniformly spaced ions with an inter-ion distance of $4.8 \mu\text{m}$ (see App. A). Since the coefficients rely on a terminated series expansion of the necessary potential to counteract the Coulomb repulsion, they represent an approximation. As discussed in App. A, the truncation of the potential expansion beyond the quartic

2.2. Ion motion within traps

term leads to a reduced confinement strength with a corresponding deviation from the initially specified inter-ion distance of $4.8\ \mu\text{m}$. In the case presented here, the minimum distance between neighboring ions is $5.7\ \mu\text{m}$ in the center of the trapping region, which increases to $7.9\ \mu\text{m}$ at the ends of the chain.

Fig. 2.5(b) depicts a comparison of the equilibrium positions of eighteen ions in the anharmonic potential based on the given parameters and in a harmonic potential with axial frequency of $\omega_z = 2\pi \times 0.138\ \text{MHz}$. Although the positions for the quartic potential deviate from the specified value of $4.8\ \mu\text{m}$ due to the termination of the series approximation, the overall difference in the inter-ion spacing is smaller than for the harmonic potential. Not taking into account the outermost ion distance on the left and right end of the chain, there is a fluctuation in inter-ion distance of 6% for the anharmonic potential. Application of the same conditions to the harmonic potential yields a fluctuation of the inter-ion distance of 11%. These values increase to 9% in the anharmonic case and 14% in the harmonic case if the outermost ions are included in the calculation.

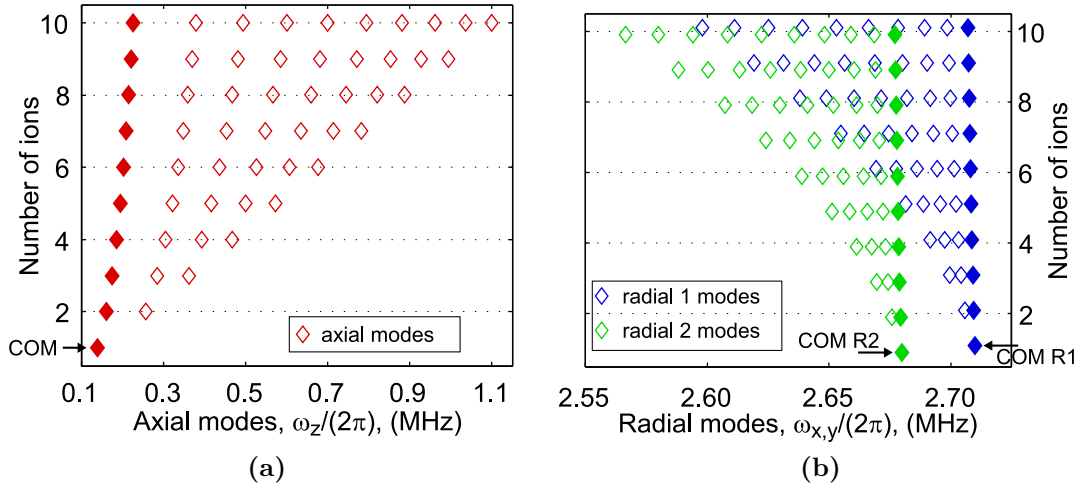


Figure 2.6. $3 \times N$ normal modes in the axial and radial directions for up to ten $^{40}\text{Ca}^+$ ions confined in an anharmonic (quartic) trapping potential with trap frequencies of $\{\omega_x, \omega_y, \omega_z\} = 2\pi \times \{2.71, 2.68, 0.138\}\ \text{MHz}$. (a) All N axial motional frequencies. (b) All $2 \times N$ radial modes. For a quartic trapping potential, all mode frequencies shift with increasing ion number.

The Lagrange formalism is applied in the same way as detailed in Sec. 2.2.1 to calculate the eigenmodes of the ion crystal. The coupling matrices are diagonalized to determine the $3 \times N$ eigenmodes of the system. Fig. 2.6 presents the normal mode frequencies for up to ten $^{40}\text{Ca}^+$ ions confined in an anharmonic trapping potential. The motional frequencies of a single ion confined in this potential are $\{\omega_x, \omega_y, \omega_z\} = 2\pi \times \{2.71, 2.68, 0.138\}\ \text{MHz}$ and the coefficients for the quadratic and the quartic terms are $\kappa_2 = 5.04 \times 10^{-14}\ \text{J m}^{-2}$ and $\kappa_4 = 2.66 \times 10^{-5}\ \text{J m}^{-4}$, respectively. Unlike the harmonic modes depicted in Fig. 2.4, the number of ions confined in the trap has an influence on the COM mode frequencies (compare also Sec. 3.3, Fig. 3 in reference [76]). With increasing ion number, the axial COM modes increase in frequency, while the radial COM modes slightly decrease. Aside from the expected shift in the mode frequencies due to the anharmonicity

of the confining potential, the overall behavior is similar to the harmonic case: the higher-order axial modes increase in frequency with the COM mode being a lower bound, and the higher-order radial modes decrease in frequency with the COM modes being an upper bound. As for the confinement in a harmonic potential, the frequency range of 0.88 MHz covered by the axial motional frequencies is much wider than the frequency range of 0.14 MHz covered by the radial mode frequencies. The spread of the radial mode spectrum corresponds to about 16% of the axial mode spectrum's frequency range.

Summary

This chapter presents the principles of charged particle confinement in Paul traps and summarizes the considerations for the motion of trapped particles in harmonic trapping potentials and an anharmonic trapping potential.

A linear Paul trap is one possibility with which to localize particles within a given trap volume. In such a trap, three-dimensional confinement is realized by a superposition of a time-varying quadrupole potential stemming from RF voltages and a harmonic potential generated by DC voltages.

A single trapped ion exhibits motion in all three spatial dimensions with oscillation frequencies entirely specified by the applied voltages, the ion mass and the trap geometry. However, the Coulomb repulsion between trapped ions has to be taken into account for multiple ions. In total, an N -ion crystal exhibits $3 \times N$ motional modes: N for each spatial direction.

In an (unsegmented) linear Paul trap, the confining axial potential is to good approximation harmonic, and experiments are executed using a linear ion crystal aligned along the trap axis. With these prerequisites, the general treatment to determine the eigenmodes of the ion crystal follows the approach detailed in reference [80] by first calculating the equilibrium position along the z -axis. Then, diagonalization of the coupling matrix at the equilibrium positions is carried out to determine time-dependent variations in position, which correspond to normal modes of the crystal.

In segmented traps, anharmonicities can be introduced in the axial confining potential and a confinement using multipoles of higher order can be achieved. The principle of the approach to determine the eigenmodes stays the same, calculation of the equilibrium position followed by diagonalization of the coupling matrix. However, the mode frequencies behave differently as they are dependent on the number of ions present in the trap.

3

Atom-light interaction

The measurements and results presented in this thesis rely on interactions between trapped atomic ions and laser light. The interaction leads to a coupling between the internal electronic states of the ion and its motional modes. This coupling can be used in connection with dissipative processes to achieve cooling to the vibrational ground state [86, 87]. Furthermore, entanglement between several ions can be mediated by the ions' interaction with laser light [28, 44, 45]. The implementation of such entangling-gate operations is a prerequisite for quantum information processing. For Cirac-Zoller gate operations, cooling of one or a number of motional modes to the ground state is required [28]. Gate operations using spin-dependent forces work under less strict conditions [44, 45]. They require, at minimum, cooling to a regime where the ground-state wave expansion is smaller than the wavelength used for the transition (the so-called Lamb-Dicke regime). Nevertheless, cooling to low mean phonon numbers improves their performance [47]. Therefore, efficient methods to cool trapped ions are necessary to control the motional state as well as possible.

In this chapter, a general introduction into the atom-light interaction of trapped particles is given in Sec. 3.1. Based on this framework, cooling methods allowing one to prepare trapped atomic ions in or close to the vibrational ground state of a mode are presented in Sec. 3.2. Determination of the system's vibrational excitation is a means of analyzing the cooling efficiency and several methods to measure the mean phonon number are then presented in Sec. 3.3. The interaction between atoms and light is a topic of enormous interest within the physics community. In this thesis, only a brief overview can be given, and the reader is referred to the literature for more information [88–90].

3.1 Light coupling to trapped ions

In the following, a single trapped ion interacting with laser light is considered. As presented in Ch. 2, the ion exhibits three modes of motion, and its internal degrees of freedom can often be treated as a two-level system. Hence, the following section first deals with the single-ion case before introducing the multi-ion case.

3.1.1 Light coupling to a single trapped ion

The interaction of a single trapped ion with a near-resonant laser field can be described semiclassically as a quantum mechanical two-level system interacting with a classical light field. A harmonic potential confines the ion to a well-defined volume as described in Ch. 2. The ground state of the trapped particle is labeled $|g\rangle$ and the excited state is labeled $|e\rangle$. The energy difference between both states is given by $E = \hbar\omega_0$, with $h = 2\pi\hbar$ Planck's constant and ω_0 the transition frequency, as depicted in Fig. 3.1. The laser radiation is modeled as a classical, monochromatic light wave. The laser field interacting with an ion located at position z at time t is given by $\mathbf{E}(z, t) = E_0\boldsymbol{\epsilon} \cos(k_z z - \omega_L t + \phi)$ [70, 87, 89]. In this expression, E_0 is the amplitude of the electric field, $\boldsymbol{\epsilon}$ is the polarization vector, $k_z = \mathbf{k} \cdot \mathbf{z}$ is the projection of the wave vector onto the z axis, ω_L corresponds to the laser frequency, and ϕ is the laser phase.

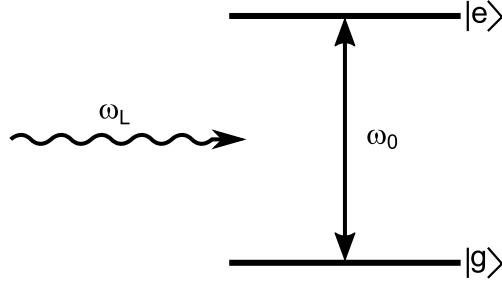


Figure 3.1. Two-level atom with ground state $|g\rangle$, excited state, $|e\rangle$, and transition frequency ω_0 , interacting with a single-mode traveling light field with frequency ω_L .

For the interaction of the two-level system with a light field, the system Hamiltonian can be divided into a stationary part $\hat{\mathcal{H}}^0$, valid for the trapped ion without a light field present, and a time-dependent part $\hat{\mathcal{H}}^i$, representing the interaction with the field. Hence, the Hamiltonian is written as [70, 87]

$$\hat{\mathcal{H}} = \hat{\mathcal{H}}^0 + \hat{\mathcal{H}}^i = \hat{\mathcal{H}}^m + \hat{\mathcal{H}}^e + \hat{\mathcal{H}}^i. \quad (3.1)$$

Eq. 3.1 introduces the specific parts of the stationary Hamiltonian, which correspond to the mechanical energy due to confinement within the harmonic potential $\hat{\mathcal{H}}^m$, and the electronic energy $\hat{\mathcal{H}}^e$, originating from internal electronic transitions. Limiting the discussion to one dimension (along the z axis), the Hamiltonian terms are given by [70, 87]

$$\hat{\mathcal{H}}^m = \frac{\hat{p}_z^2}{2m} + \frac{m\omega_z^2}{2}\hat{z}^2 = \hbar\omega_z \left(\hat{a}^\dagger \hat{a} + \frac{1}{2} \right), \quad (3.2)$$

$$\hat{\mathcal{H}}^e = \frac{\hbar\omega_0}{2} \hat{\sigma}_z, \quad (3.3)$$

with m the mass of the ion, ω_z the motional frequency, and \hat{p}_z and \hat{z} the momentum and position operators. Furthermore, the ladder operators \hat{a} and \hat{a}^\dagger for the quantum harmonic oscillator have been introduced as [91]

$$\hat{a} = \sqrt{\frac{1}{2m\hbar\omega_z}} (m\omega_z \hat{z} + i\hat{p}_z), \quad \hat{a}^\dagger = \sqrt{\frac{1}{2m\hbar\omega_z}} (m\omega_z \hat{z} - i\hat{p}_z). \quad (3.4)$$

3.1. Light coupling to trapped ions

The energy difference of the two states is denoted by the spin-1/2 operator $\hat{\sigma}_z$ [70, 87]. This operator is part of the spin-1/2 operator basis¹ used to describe two-level systems [70, 89].

The interaction Hamiltonian between the light field and the two-level system is given by [70, 87, 89]

$$\hat{\mathcal{H}}^i = \frac{\hbar\Omega}{2} (\hat{\sigma}_+ + \hat{\sigma}_-) \left[e^{i(k_z z + \omega_L t + \phi)} + e^{-i(k_z z + \omega_L t + \phi)} \right], \quad (3.5)$$

with Ω the Rabi frequency that specifies the coupling strength between the ion's transition and the light field, and $\hat{\sigma}_+$ and $\hat{\sigma}_-$ the atomic transition operators.

Transformation into the interaction picture simplifies the analysis of the Hamiltonian (Eq. 3.5). The transformation is carried out by applying the unitary operator $\hat{\mathcal{U}}_0 = \exp(-i\hat{\mathcal{H}}^0 t/\hbar)$ to the interaction term of the Hamiltonian and yields [70, 92]

$$\hat{\mathcal{H}}^{\text{int}} = \hat{\mathcal{U}}_0^\dagger \hat{\mathcal{H}}^i \hat{\mathcal{U}}_0 = \frac{\hbar\Omega}{2} \left(\hat{\sigma}_+ e^{-i(\Delta t - \phi)} e^{i\eta(\hat{a} \exp(-i\omega_z t) + \hat{a}^\dagger \exp(i\omega_z t))} + H.c. \right). \quad (3.6)$$

In Eq. 3.6, the *rotating wave approximation (RWA)* has been applied, which neglects terms rotating at a frequency $\omega_L + \omega_0$ [70, 87, 89]. Also, the detuning parameter, $\Delta = \omega_L - \omega_0$, and the Lamb-Dicke parameter [70, 87],

$$\eta = k_z \sqrt{\frac{\hbar}{2m\omega_z}}, \quad (3.7)$$

have been introduced. The Lamb-Dicke parameter as given in Eq. 3.7, is the ratio between the wavelength of the laser light exciting the transition and the spatial extent of the ion's ground-state wave-packet. The interaction Hamiltonian (Eq. 3.6) leads to a coupling between the motional states of the ion and its electronic states via the light field, as depicted in Fig. 3.2.

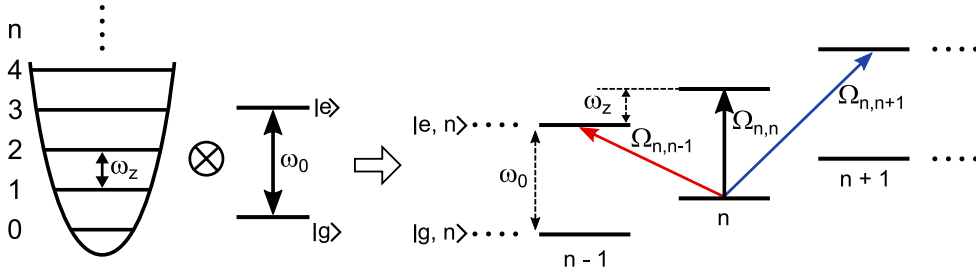


Figure 3.2. Coupling of a harmonic oscillator with frequency ω_z (representing the ion's motion within the trap) with a two-level system with transition frequency ω_0 (representing the ion's internal electronic transition). Due to the coupling of electronic states and vibrational states, transitions can be excited as indicated by the red, black and blue arrows (see main text for more information).

¹The spin-1/2 operator basis consists of the identity matrix $\mathbb{1}$ and the Pauli spin operators $\hat{\sigma}_x$, $\hat{\sigma}_y$, and $\hat{\sigma}_z$.

The general state of the system can be written as a superposition of the wave functions describing the ground state $|g, n\rangle$ and the excited state $|e, n\rangle$ [70, 71]:

$$\Psi(t) = \sum_n (c_{g,n}(t) |g, n\rangle + c_{e,n}(t) |e, n\rangle). \quad (3.8)$$

In Eq. 3.8, a summation over all n possible excitations of the motional modes is carried out, and the time-dependent probabilities for the ground state $c_{g,n}(t)$, and excited state $c_{e,n}(t)$, are introduced. The time evolution of the trapped ion interacting with electromagnetic radiation is governed by the Schrödinger equation and can be written as

$$i\hbar \frac{\partial \Psi(\mathbf{r}, t)}{\partial t} = \hat{\mathcal{H}} \Psi(\mathbf{r}, t), \quad (3.9)$$

setting the evolution of the system's state described by the wave vector $\Psi(\mathbf{r}, t)$ equal to the total energy of the system, represented by the Hamilton operator $\hat{\mathcal{H}}$ [89].

Eq. 3.9 can be transferred into a system of coupled differential equations for the coefficients $c_{g,n}(t)$, and $c_{e,n}(t)$. For the case of near-resonant laser interaction close to a transition $|g, n\rangle \leftrightarrow |e, n+p\rangle$ with low laser intensity ($\Omega \ll \omega_z$), the coupling acts pairwise on these transitions [71, 75]. The coupling strength is given by the Rabi oscillation frequency, Ω , and can be calculated as [70, 71]

$$\Omega_{n,n+m} = \Omega \langle n+m | e^{i\eta(\hat{a}+\hat{a}^\dagger)} | n \rangle, \quad (3.10)$$

with n the phonon number, i.e., the number of excited vibrational states of the motional mode, and m an integer.

Lamb-Dicke regime

The Lamb-Dicke regime is defined as the parameter range within which the spatial extent of the ground-state wave function describing the ion is much smaller than the wavelength of the laser exciting the ion's electronic transition. This relation can be expressed as $\eta\sqrt{2\langle n \rangle + 1} \ll 1$, which leads to the constraint $\eta \ll 1$. In this regime, it is possible to expand the interaction Hamiltonian (Eq. 3.6) in terms of this small parameter, η , using [70, 71]

$$e^{i\eta(\hat{a} \exp(-i\omega_z t) + \hat{a}^\dagger \exp(i\omega_z t))} \approx 1 + i\eta(\hat{a}e^{-i\omega_z t} + \hat{a}^\dagger e^{i\omega_z t}) + \mathcal{O}(\eta^2). \quad (3.11)$$

Hence, to first order, there are three possible transitions in the coupled system that can be excited. The transitions are as follows:

- *Carrier transition*

The detuning is set as $\Delta = 0$. Excitation of the internal state does not change the phonon number (black arrow in Fig. 3.2) and the coupling strength is independent of the vibrational quantum number. The Hamiltonian is given by [70]

$$\hat{\mathcal{H}}_{\text{CAR}}^{\text{int}} = \frac{\hbar}{2} \Omega (\hat{\sigma}_+ e^{i\phi} + \hat{\sigma}_- e^{-i\phi}). \quad (3.12)$$

3.1. Light coupling to trapped ions

- *Red-sideband transition*

The detuning is set as $\Delta = -\omega_z$. Excitation of the internal state is accompanied by a decrease in the phonon number by one (red arrow in Fig. 3.2). The Hamiltonian and the coupling strength are given by [70]

$$\hat{\mathcal{H}}_{\text{RSB}}^{\text{int}} = \frac{i\hbar}{2} \Omega \eta \left(\hat{a} \hat{\sigma}_+ e^{i\phi} + \hat{a}^\dagger \hat{\sigma}_- e^{-i\phi} \right), \quad (3.13)$$

$$\Omega_{n,n-1} = \Omega \eta \sqrt{n}. \quad (3.14)$$

- *Blue-sideband transition*

The detuning is set as $\Delta = +\omega_z$. Excitation of the internal state is accompanied by an increase of the phonon number by one (blue arrow in Fig. 3.2). The Hamiltonian and the coupling strength for $|n\rangle \leftrightarrow |n+1\rangle$ transitions are given by [70]

$$\hat{\mathcal{H}}_{\text{BSB}}^{\text{int}} = \frac{i\hbar}{2} \Omega \eta \left(\hat{a}^\dagger \hat{\sigma}_+ e^{i\phi} + \hat{a} \hat{\sigma}_- e^{-i\phi} \right), \quad (3.15)$$

$$\Omega_{n,n+1} = \Omega \eta \sqrt{n+1}. \quad (3.16)$$

3.1.2 Light coupling to a multi-ion crystal

The previous discussion holds true for a single trapped ion interacting with a monochromatic traveling wave laser field. An increase in the number of ions leads to coupling due to the Coulomb interaction between the trapped particles. This coupling manifests itself in modes of shared motion. A description for the case of an N -ion crystal can be carried out as follows. Again, the discussion is limited to one dimension.

The stationary part, $\hat{\mathcal{H}}^0$, can be rewritten by changing its components, the mechanical Hamiltonian, $\hat{\mathcal{H}}^m$, and the electronic Hamiltonian, $\hat{\mathcal{H}}^e$, to

$$\hat{\mathcal{H}}_N^m = \hbar \sum_{j=1}^N \omega_j \left(\hat{a}_j^\dagger \hat{a}_j + \frac{1}{2} \right), \quad (3.17)$$

$$\hat{\mathcal{H}}_N^e = \frac{\hbar \omega_0}{2} \sum_{l=1}^N \hat{\sigma}_z^l. \quad (3.18)$$

In Eq. 3.17, a summation over the possible eigenmodes of the system with frequency ω_j is introduced. In Eq. 3.18, a summation over all ions is executed. The interaction Hamiltonian, $\hat{\mathcal{H}}^{\text{int}}$, can be written as [75, 93]

$$\hat{\mathcal{H}}_N^{\text{int}} = \frac{\hbar}{2} \sum_{l=1}^N \Omega_l \left(\hat{\sigma}_+^l e^{-i(\Delta t - \phi_l)} e^{i \sum_{j=1}^N \eta_{l,j} (\hat{a}_j \exp(-i\omega_j t) + \hat{a}_j^\dagger \exp(i\omega_j t))} + H.c. \right). \quad (3.19)$$

Eq. 3.19 gives the interaction Hamiltonian for N ions in the interaction picture with the *rotating wave approximation* applied. Note that the Rabi frequencies, Ω_l , and phases, ϕ_l , need not be the same for all ions. Furthermore, the Lamb-Dicke parameter is dependent on the eigenmode [75, 80, 93]. In addition, the Lamb-Dicke parameter is proportional to the overlap between each ion's motion around its equilibrium position and the light's propagation direction [75, 80, 93].

3.2 Laser cooling

The cooling dynamics of a trapped ion are governed by three parameters: ω_m the ion's motional frequency due to its harmonic confinement²; Γ the linewidth of the electronic transition; and $\omega_R = \hbar k^2/(2m)$ the photon recoil frequency [87]. Within the Lamb-Dicke regime, $\omega_R < \omega_m$, which is assumed throughout the following discussion. Furthermore, the ratio between transition linewidth, Γ , and motional frequency, ω_m , leads to the following distinction:

- $\Gamma > \omega_m$ defines the *weak confinement limit* [87] or *unresolved sideband regime* [70].

The transitions described by the Hamiltonians of Eqs. 3.12 - 3.16 cannot be addressed individually as the linewidth of the electronic transition covers a much broader frequency range and spontaneous emission is non-negligible. Doppler cooling is carried out in this regime.

- $\Gamma < \omega_m$ defines the *strong confinement limit* [87] or *resolved sideband regime* [70].

The linewidth of the electronic state transition covers a narrow frequency range. Hence, individual transitions described by the Hamiltonians of Eqs. 3.12 - 3.16 can be resolved spectroscopically. Each mode's frequency can be individually addressed, and this property can be used for ground-state cooling.

All experiments presented in this thesis take advantage of a two-step cooling process. First, Doppler cooling is executed to reduce the kinetic energy of the trapped ion and cool it into the Lamb-Dicke regime. In a second step, a ground-state-cooling technique is applied in order to prepare the ion for possible gate operations. In the following, these cooling techniques will be introduced. However, a detailed description is beyond the scope of this thesis, and the reader is referred to the literature [70, 86–88].

3.2.1 Doppler cooling

Doppler cooling takes place in the weak confinement regime ($\Gamma > \omega_m$) [12, 13, 22]. If the ion's velocity induces a Doppler shift that compensates for the detuning between its internal electronic transition frequency and the laser frequency, a photon is absorbed and population transfer between the ground state and the excited state occurs [86]. Subsequent spontaneous emission of a photon leads to a recoil momentum acting in random direction on the ion. Averaging over a number of absorption-emission cycles leads to a deceleration of the ion.

The velocity-dependent light force responsible for the process cannot cool the particle into its motional ground state: In the unresolved sideband regime cooling to such an extent is prohibited as the random direction of the spontaneous emission process increases the velocity uncertainty in the transversal direction,

²Previously, the motional frequency was taken to be along the z axis and denoted as ω_z .

3.2. Laser cooling

causing heating of the ion [86]. Therefore, a lower limit exists on the possible outcome of cooling. In the ideal, one-dimensional, case a red detuning of a value equal to half the natural linewidth is chosen: $\Delta = -\Gamma/2$. With this choice, the minimum temperature, T_D , and hence the minimum mean phonon number, $\langle n \rangle_{\min}$ can be calculated as [88]

$$k_B T_D = \frac{\hbar\Gamma}{2}, \quad k_B T_D = \langle n \rangle_{\min} \hbar\omega_m, \quad (3.20)$$

with k_B , the Boltzmann constant. Temperature is in this case an expression of kinetic energy and not a statement about thermal equilibrium.

In this simplified, qualitative picture, micromotion present in RF traps is not considered, which is a valid assumption in a regime where micromotion sidebands are small compared to carrier sidebands. However, evaluations of Doppler cooling taking micromotion into account can be found in reference [94]. Furthermore, the assumption of a two-level system is only an approximation and does not correctly reflect experimental systems. This can be seen, for example, as an applied external magnetic field leads to a splitting of the the two-level system into Zeeman submanifolds. Detailed theoretical studies on multi-level ions can be found in reference [95], and an experimental investigation was published in reference [96].

For $^{40}\text{Ca}^+$, Doppler cooling is applied on the $S_{1/2} \leftrightarrow P_{1/2}$ transition with a linewidth of $\Gamma = 2\pi \times 21.57$ MHz [97]. After Doppler cooling such an ion, motional frequencies of $\omega_m = 2\pi \times 1$ MHz lead to an estimated minimum mean phonon number of $\langle n \rangle_{\min} \approx 11$. Hence, additional cooling processes are necessary to reach the vibrational ground state. Two schemes that achieve ground-state cooling are presented in the following section. For sideband cooling, the requirement $\Gamma < \omega_m$ to operate in the resolved sideband regime is met by using a quadrupole transition [14, 87]. EIT cooling is implemented on dipole-allowed transitions using quantum interference phenomena to access the underlying sideband substructure for the cooling process [48].

3.2.2 Sideband cooling

For sideband cooling of a single trapped ion with transition frequency ω_0 and motional frequency ω_m , a laser is tuned into resonance with the first red sideband ($\omega_L = \omega_0 - \omega_m$) of the electronic transition. Hence, the ion absorbs a photon with energy $\hbar(\omega_0 - \omega_m)$ and then emits a photon primarily on the carrier transition with energy $\hbar\omega_0$. Such a process leads to a reduction of the kinetic energy, and the mean phonon number decreases [14, 86], as illustrated in Fig. 3.3(a).

The rate at which sideband cooling takes place is given by [70, 71]

$$R = \Gamma \frac{(\Omega\eta\sqrt{n})^2}{2(\Omega\eta\sqrt{n})^2 + \Gamma^2}. \quad (3.21)$$

As indicated in Eq. 3.21, the linewidth of a transition sets an upper limit for the cooling rate. Thus, transitions with a long lifetime, which is synonymous with

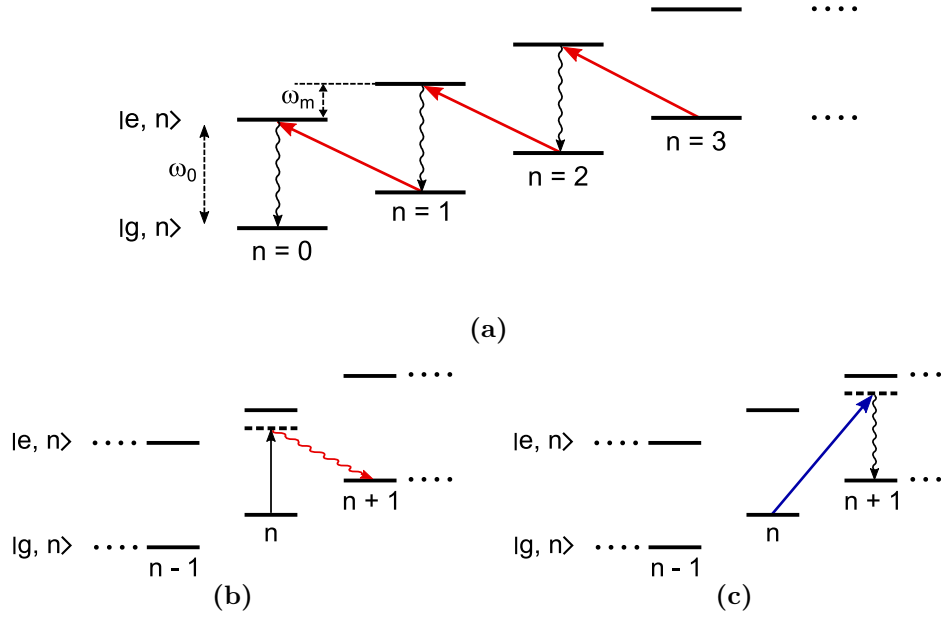


Figure 3.3. Sideband-cooling scheme and off-resonant heating processes. (a) In the Lamb-Dicke regime and the strong confinement limit, a laser can be tuned to the first red sideband ($\omega_L = \omega_0 - \omega_m$). Excitation of the ion on the red sideband reduces the phonon number by one. With high probability this absorption is followed by a spontaneous emission on the carrier transition, effectively reducing the kinetic energy of the ion and pumping the population into a dark state for the red-sideband excitation. (b) There is a small probability that an off-resonant absorption on the carrier transition occurs, followed by an emission process on the red-sideband transition. Such a process leads to heating of the ion. (c) There is a small probability that an off-resonant absorption on the blue-sideband transition occurs, followed by an emission process on the carrier transition. Such a process leads to heating of the ion.

a narrow linewidth, exhibit a slower cooling rate. In such cases, it is beneficial to shorten the upper level's lifetime by coupling it to an additional, short-lived state using a laser. This technique is called *quenching* and results in an effective linewidth for the coupled system denoted by [70, 71, 98]

$$\tilde{\Gamma} = \frac{\Omega_{\text{aux}}^2}{(\Gamma + \Gamma_{\text{aux}})^2 + 4\Delta_{\text{aux}}^2} \Gamma^2, \quad (3.22)$$

with the linewidth of the additional transition Γ_{aux} , the laser detuning from the upper, short-lived state Δ_{aux} , and the Rabi frequency at which the transition is driven Ω_{aux} . Thus the effective linewidth of the coupled transition is determined by the chosen laser parameters.

In the sideband-cooling scheme, the laser optically pumps the population to the vibrational ground state, which is a dark state for the process (Fig. 3.3(a)). Hence, the rate given in Eq. 3.21 decreases with decreasing phonon state, n , until a dark state, $n = 0$, is reached where the rate is zero. However, the “dark state” is not entirely dark because of off-resonant processes. These processes encompass excitation on the carrier transition followed by emission on the red-sideband transition, as shown in Fig. 3.3(b), as well as absorption on the blue sideband

3.2. Laser cooling

followed by emission on the carrier transition, as illustrated in Fig. 3.3(c). These off-resonant processes limit the ground-state population as they are effectively heating the system.

The minimum mean phonon number achievable by the scheme can be calculated as

$$\langle n \rangle_{\min} = \frac{\Gamma^2}{4\omega_m^2} \left(\frac{\tilde{\eta}^2}{\eta^2} + \frac{1}{4} \right). \quad (3.23)$$

Eq. 3.23 introduces the Lamb-Dicke factor $\tilde{\eta}$ for the spontaneous emission process, which can be defined as

$$\tilde{\eta} = \alpha \frac{2\pi}{\lambda_{\text{aux}}} \sqrt{\frac{\hbar}{2m\omega_m}}. \quad (3.24)$$

In Eq. 3.24, the spontaneous emission wavelength is denoted as λ_{aux} since, specifically for a quenched system, it does not have to equal the wavelength for the absorption process. In addition, the spatial distribution of the spontaneous emission is taken into account with the geometrical factor α . Isotropic spatial distribution yields $\alpha = 1/3$. Apart from the geometrical factor α , the two Lamb-Dicke parameters for spontaneous emission, $\tilde{\eta}$, and coherent excitation, η , (Eq. 3.7) differ as η depends on the projection of the laser beam propagation direction on the axis of the motional mode.

For sideband cooling, the steady-state population for a given mean phonon number can be calculated based on references [70, 98]. In these calculations, quenching of a long-lived excited state via an additional laser is taken into account by an effective linewidth of the two-level system, $\tilde{\Gamma}$ (Eq. 3.22).

Sideband cooling of $^{40}\text{Ca}^+$ is implemented on the $S_{1/2} \Leftrightarrow D_{5/2}$ transition with a linewidth of $\Gamma = 2\pi \times 1$ Hz. The slow cooling rate of this two-level system can be increased by coupling the $D_{5/2}$ state to the $P_{3/2}$ state with laser light at 854 nm. The corresponding effective linewidth $\tilde{\Gamma}$ (Eq. 3.22) depends on the intensity and detuning of the laser at 854 nm as well as on the linewidths of both transitions, $S_{1/2} \Leftrightarrow D_{5/2}$ and $D_{5/2} \Leftrightarrow P_{3/2}$.

The steady-state population, as discussed in references [98, 99], is illustrated for a single $^{40}\text{Ca}^+$ ion in Fig. 3.4. Fig. 3.4(a) presents the steady-state population for settings that allow comparison to the steady-state population for EIT cooling presented in Fig. 3.7. The frequency range over which the technique can lead to efficient cooling of the particle into the ground state is narrower than for EIT cooling.

Furthermore, Fig. 3.4(b) illustrates the application of experimentally feasible settings to reach lower minimum mean-phonon numbers, which also leads to a lower cooling rate. We see from Fig. 3.4 that it is necessary to tune the laser to within a few kHz to the red sideband of the motional mode to be cooled. Due to the narrow bandwidth for effective cooling, sideband cooling is limited to cooling single modes effectively. The increase of the ion number leads to a denser mode spectrum. Coupling of uncooled motional modes to the mode at which a gate operation is executed can reduce the gate operation's performance. Thus, it is beneficial to cool multiple modes. However, individual modes can be

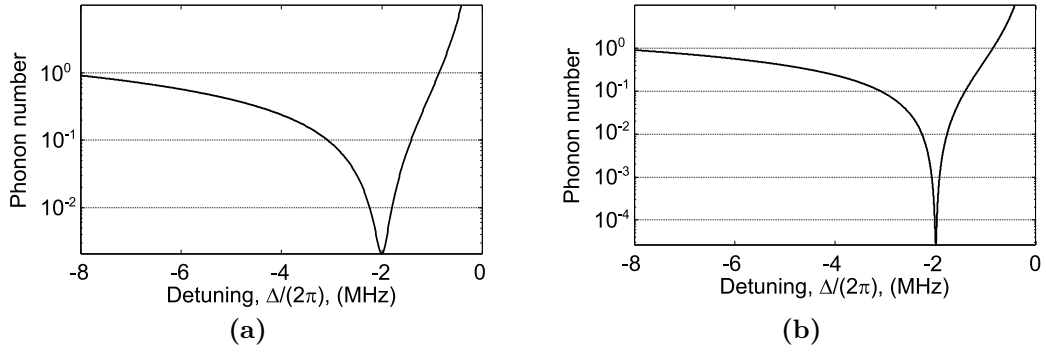


Figure 3.4. Steady-state population after sideband cooling with respect to laser detuning. (a) The parameters for the plot are chosen to reach a minimum mean phonon number of $\langle n \rangle_{\min} = 0.002$ for a single trapped $^{40}\text{Ca}^+$ ion to facilitate comparison with the steady-state population after EIT cooling (Fig. 3.7). Sideband cooling is implemented at 729 nm for the $S_{1/2} \leftrightarrow D_{5/2}$ transition with an effective linewidth, due to quenching, of $\tilde{\Gamma} = 2\pi \times 230$ kHz, a motional frequency $\omega_m = 2\pi \times 2$ MHz, and a Rabi frequency of $\Omega = 2\pi \times 1$ kHz. (b) A reduction of the effective linewidth to $\tilde{\Gamma} = 2\pi \times 26$ kHz leads to a lower minimum mean phonon number of $\langle n \rangle_{\min} = 4 \times 10^{-5}$, which is desirable in an experiment. However, this is accompanied by a reduction of the cooling rate since the rate is proportional to $\tilde{\Gamma}$.

cooled consecutively, that is one after the other. One drawback of this scheme is that sequential cooling leads to an unwanted increase in cooling time and a concomitant reheating of the modes that are addressed first in the sequence [87].

In trapped-ion experiments, sideband cooling of one motional mode into the vibrational ground state typically takes several ms [37]. Hence, if cooling of multiple modes is required, increasing the number of ions in the crystal quickly renders sideband cooling inefficient as the number of eigenmodes increases with the number of added ions³. Thus, alternate techniques that allow simultaneous cooling of multiple modes are favorable; EIT cooling is one such scheme.

3.2.3 EIT cooling

Electromagnetically induced transparency (EIT) refers to an effect that allows a laser beam to propagate through an optically dense medium as if the medium were transparent [100]. In this thesis, the term medium refers to a countable number of ions confined within an RF trap. Hence, a quantum mechanical description is justified, and under these circumstances, EIT is also known as *coherent population trapping* [100–102].

The EIT effect is observed in a three-level Λ atomic system consisting of two ground states, $|g\rangle$ and $|f\rangle$, and one short-lived excited state, $|e\rangle$, as depicted in Fig. 3.5(a). The two ground states are coupled to the excited state via two laser fields with Rabi frequencies Ω_g and Ω_f and a detuning Δ of the dressing laser. As a result, coherent population trapping occurs. The system can be described in terms of a superposition of the two ground states, which is not coupled to the

³As described in Ch. 2, every added ion increases the total number of motional modes three-fold — one additional mode for each degree of freedom.

3.2. Laser cooling

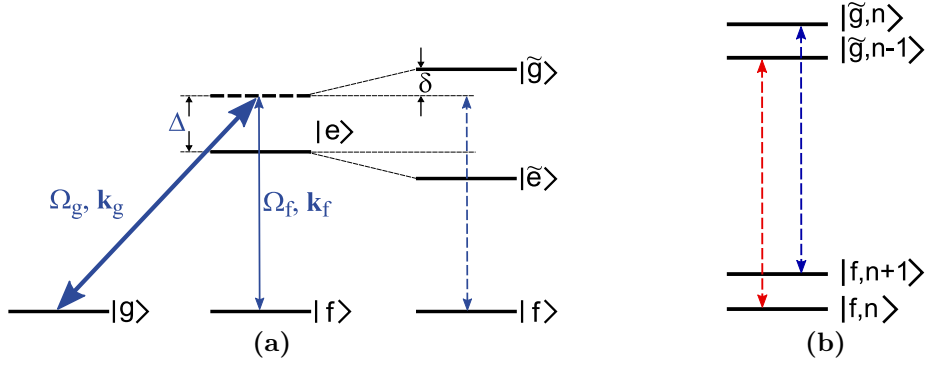


Figure 3.5. A scheme for the implementation of EIT cooling and the associated dressed states. (a) Λ -like energy levels with ground states $|g\rangle$ and $|f\rangle$ and excited state $|e\rangle$. The ground state and excited state are coupled $|g\rangle \leftrightarrow |e\rangle$ with a strong laser at Rabi frequency Ω_g , wave vector \mathbf{k}_g , and detuning Δ . Dressed states $|\tilde{g}\rangle$ and $|\tilde{e}\rangle$ are generated from this coupling and shifted by the light shift δ with respect to the original states. (b) Possible transitions that the weak probe beam can couple: there is a high probability for red-sideband transitions $|f, n\rangle \leftrightarrow |\tilde{g}, n-1\rangle$ and a low probability for blue sideband transitions $|f, n+1\rangle \leftrightarrow |\tilde{g}, n\rangle$ (see also Fig. 3.6, inset).

excited state and which is given by [101]

$$|a_0\rangle = \cos(\theta) |g\rangle - \sin(\theta) |f\rangle, \quad \tan(\theta) = \frac{\Omega_g}{\Omega_f}. \quad (3.25)$$

Cooling based on **electromagnetically induced transparency** uses this principle [48]. It works on a Λ system as in Fig. 3.5(a) and is mediated by a two-photon process. The first laser is used to couple the ground state $|g\rangle$ to the excited state $|e\rangle$. This process can be described as the creation of dressed states [89] $|\tilde{g}\rangle$ and $|\tilde{e}\rangle$, which combine the atomic states with the radiation field [102]. The second laser is applied with low intensity and can be used to probe $|\tilde{g}\rangle$ and $|\tilde{e}\rangle$. Note that the dressed states experience a light shift

$$\delta = \frac{1}{2} \left(\sqrt{\Omega_g^2 + \Delta^2} - |\Delta| \right). \quad (3.26)$$

Varying the detuning of the weak laser beam, Δ_f , creates an absorption profile as shown in Fig. 3.6. The depicted upper state population ρ_{ee} can be derived based on the formula [101, 102]

$$\rho_{ee} = \frac{4\Omega_g^2\Omega_f^2P(\Delta - \Delta_f)^2}{Q}, \quad (3.27)$$

$$Q = (\Delta - \Delta_f)^2 \left\{ 8\Omega_g^2\Omega_f^2P + 16\Omega_g^2\Gamma_f[P^2 + \Delta_f^2] + 16\Omega_f^2\Gamma_g[P^2 + \Delta^2] \right\} \\ + 8(\Delta - \Delta_f)(\Omega_g^4\Delta_f\Gamma_f - \Omega_f^4\Delta\Gamma_g) + (\Omega_g^2\Gamma_f + \Omega_f^2\Gamma_g)(\Omega_g^2 + \Omega_f^2)^2, \\ P = \Gamma_g + \Gamma_f.$$

In Eq. 3.27, the linewidth of the $|f\rangle \leftrightarrow |e\rangle$ transition is Γ_f , and the the linewidth of the $|g\rangle \leftrightarrow |e\rangle$ transition is Γ_g .

The resulting spectrum (Eq. 3.27, Fig. 3.6) exhibits a broad resonance where the probe beam is resonant with the transition to the bare state $|\tilde{e}\rangle$. Furthermore,

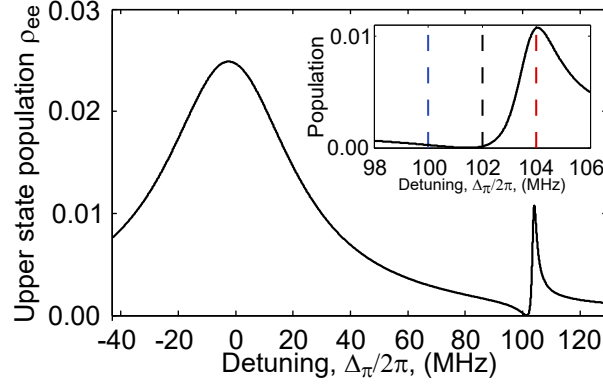


Figure 3.6. Line profile generated by scanning the detuning of the weak probe beam. This graph corresponds to the experimental situation as presented in Ch. 6. The cooling scheme is implemented on the $S_{1/2} \leftrightarrow P_{1/2}$ transition in $^{40}\text{Ca}^+$, with linewidth $\Gamma = 2\pi \times 21.57$ MHz, detuning of the σ^+ beam $\Delta = 4.7 \times \Gamma$, a Rabi frequency of $\Omega_\sigma = 1.45 \times \Gamma$ for the σ^+ beam, and a Rabi frequency of $\Omega_\pi = 0.2 \times \Gamma$ for the π beam. The inset shows a close-up around the zero crossing of the line profile. For $\delta = \omega_m$, the motional sidebands correspond to the dashed lines, leading to a high absorption probability for the red-sideband transition and a low absorption probability for the blue-sideband transition. Note that the parameters of the general formula given in Eq. 3.27 are related to the experimental parameters used for the graph as follows: $\Delta_\pi = \Delta_f$, $\Gamma = (\Gamma_g + \Gamma_f)$, $\Omega_\sigma = \Omega_g$, $\Omega_\pi = \Omega_f$;

a narrow Fano profile can be observed near the zero crossing of the curve, at which the detunings of both laser beams are the same [102].

An ion confined by a harmonic trapping potential oscillating at frequency ω_m is able to absorb photons at frequencies corresponding to motional sidebands, as presented in Sec. 3.1. For the EIT configuration, this means that the weak probe laser can drive transitions $|f, n\rangle \leftrightarrow |\tilde{g}, n-1\rangle$ and $|f, n+1\rangle \leftrightarrow |\tilde{g}, n\rangle$, as depicted in Fig. 3.5(b) (and avoids excitations on the carrier transition, which leads to heating).

The EIT cooling scheme requires the light shift induced by the strong coupling beam to be equal to the motional frequency $\delta = \omega_m$. If this condition is satisfied, the absorption probability on the red sideband $|f, n\rangle \leftrightarrow |\tilde{g}, n-1\rangle$ corresponds to the Fano feature (see inset Fig. 3.6). In addition, carrier transitions $|f, n\rangle \leftrightarrow |\tilde{g}, n\rangle$ are equal to the zero crossing and are suppressed since the overall detuning, Δ , is the same for both beams. Hence, heating processes are reduced to absorption on the blue sideband, for which the absorption probability is much lower than for red-sideband absorption.

The performance of the EIT cooling scheme can be controlled by the detuning, Δ , as this parameter sets the decay rate of the dressed state $|\tilde{g}\rangle$. A high detuning leads to very low minimum phonon numbers but a narrow cooling range, while a low detuning limits the lowest possible temperature but increases the frequency range over which the cooling works. Nevertheless, as heating processes due to carrier excitations are suppressed, cooling close to the ground state is possible. The cooling process can be described using rate equations and can be calculated as [49, 86, 87]

$$\langle \dot{n} \rangle = -\eta^2 (A_- + A_+) \langle n \rangle + \eta^2 A_+. \quad (3.28)$$

3.2. Laser cooling

Here, the Lamb-Dicke factor, $\eta = |\mathbf{e}_m \cdot (\mathbf{k}_f - \mathbf{k}_g)| \sqrt{\frac{\hbar}{2m\omega_m}}$, includes the Raman k vector $\mathbf{k}_f - \mathbf{k}_g$ with wave vector \mathbf{k}_g for the coupling laser, \mathbf{k}_f for the probe laser, and \mathbf{e}_m the direction of the oscillation. The rate coefficients A_{\pm} are given by [48]

$$A_{\pm} = \frac{\Omega_f^2}{\Gamma} \frac{\Gamma^2 \omega_m^2}{\Gamma^2 \omega_m^2 + 4 \left(\frac{\Omega_g^2}{4} - \omega_m (\omega_m \mp \Delta) \right)^2}, \quad (3.29)$$

with Γ the linewidth of the transition. The steady-state solution of Eq. 3.28 is found to be [86, 87]

$$\langle n \rangle = \frac{A_+}{A_- - A_+}, \quad (3.30)$$

and the cooling rate is given by [86]

$$R = \eta^2 (A_- - A_+). \quad (3.31)$$

The frequency range over which cooling can be achieved is plotted in Fig. 3.7 by evaluation of Eq. 3.30. In addition, the blue dashed line in Fig. 3.7 corresponds to the steady-state population after sideband cooling, as illustrated in Fig. 3.4(a). In order to facilitate easy comparison of both situations, the sideband cooling graph is inverted along the x axis. The settings chosen for EIT cooling allow cooling to $\langle n \rangle_{\min} = 0.1$ over a range of 2.5 MHz and cooling to $\langle n \rangle_{\min} = 0.01$ over a range of 0.7 MHz. Although both curves behave in a similar fashion, the frequency range over which sideband cooling is effective is up to 35% narrower than the frequency range over which EIT cooling is effective. Furthermore, sideband cooling is renowned for its efficiency in reaching low minimum

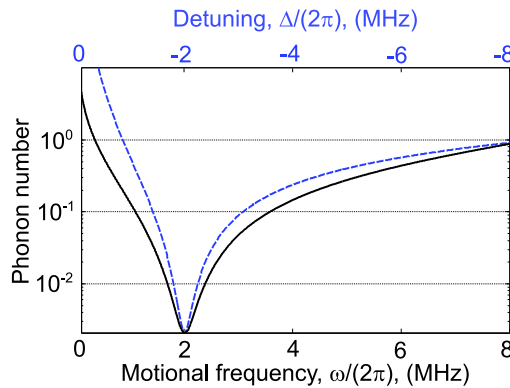


Figure 3.7. Steady-state mean phonon number $\langle n \rangle$ as a function of the motional trap frequency. The graph shows a tip around a motional frequency of 2 MHz, which is chosen on the basis of the experimental settings presented in Ch. 6. The minimum mean phonon number reached is $\langle n \rangle_{\min} = 0.0021$. The parameters for the plot are based on the $S_{1/2} \leftrightarrow P_{1/2}$ transition in $^{40}\text{Ca}^+$, with linewidth $\Gamma = 2\pi \times 21.57$ MHz, detuning $\Delta_\sigma = 5.5 \times \Gamma$ and Rabi frequency of $\Omega_\sigma = 1.45 \times \Gamma$ for the σ^+ beam. In addition, the blue dashed curve depicts the steady-state population after sideband cooling, as illustrated in Fig. 3.4(a). The sideband cooling parameters, as given in the caption of Fig. 3.4(a), are chosen to achieve the same minimum mean phonon number as with the EIT cooling. Note that the sideband cooling curve is inverted along the x axis (indicated by the blue axis labels).

mean phonon numbers. However, as illustrated in Fig. 3.4(b), the trade-off between low minimum mean phonon numbers and the achieved cooling range leads to even narrower cooling bandwidths. In general, the property of effective cooling over a larger frequency range than, for example, with sideband cooling, makes EIT cooling attractive as a way to simultaneously address the multiple motional frequencies corresponding to long strings of ions. Such ion strings could also be confined within anharmonic trapping potentials, where the mode spacing differs from the harmonic case.

3.3 Measuring motional states of trapped ions

As presented in Sec. 3.1, the interaction between a trapped ion and a radiation field couples the internal electronic states of the ion and its motional states. As the coupling between the laser and the trapped ion depends on the ion's internal and vibrational state, it is possible to map the phonon state onto the electronic state of the ion [70]. In the following, measurements to determine the mean phonon number are discussed.

3.3.1 Red-sideband and blue-sideband excitation

For a single trapped ion as a two-level system, solutions of the Schrödinger equation (Eq. 3.9) give the probabilities to find the ion in the ground state or the excited state. These probabilities depend on the transitions participating in the interaction. Within the Lamb-Dicke regime, the only transitions it is necessary to take into account are the carrier transition, the red-sideband transition and the blue-sideband transition. If we start in the electronic ground state $|\psi(0)\rangle = \sum_n c_{g,n}|g, n\rangle$ and drive the ion on the blue-sideband transition ($\Delta = +\omega_m$), the probability P_e^{BSB} to find the ion in the excited state at time t is given by [70, 103, 104]

$$P_e^{\text{BSB}}(t) = \frac{1}{2} \left(1 - \sum_{n=0}^{\infty} \tilde{\rho}_n \cos(\Omega_{n,n+1}t) \right). \quad (3.32)$$

Eq. 3.32 introduces the probability distribution $\tilde{\rho}_n$ for the motional state of the ion. Directly after laser cooling, this probability can be modeled as a thermal distribution of motional states, denoted by

$$\tilde{\rho}_n = \frac{\langle n \rangle^n}{(\langle n \rangle + 1)^{n+1}}, \quad (3.33)$$

with $\langle n \rangle$ the mean phonon number. The probability to find the ion in the ground state, P_g^{BSB} , can be calculated from $P_e^{\text{BSB}} + P_g^{\text{BSB}} = 1$.

For red-sideband excitation ($\Delta = -\omega_m$) starting from the same ground state as before $|\psi(0)\rangle$, the probability P_e^{RSB} , to find the ion in the excited state at time t is given by [71, 84, 104]

$$P_e^{\text{RSB}}(t) = \frac{1}{2} \left(1 - \sum_{n=0}^{\infty} \tilde{\rho}_n \cos(\Omega_{n,n-1}t) \right). \quad (3.34)$$

3.3. Measuring motional states of trapped ions

Both excitation probabilities can be experimentally determined. Their ratio can be used to express the mean phonon number as [70, 105]

$$R = \frac{P_e^{\text{RSB}}}{P_e^{\text{BSB}}} = \frac{\langle n \rangle}{\langle n \rangle + 1}, \quad (3.35)$$

$$\Rightarrow \langle n \rangle = \frac{R}{1 - R}. \quad (3.36)$$

This derivation is independent of the time t at which the measurement is executed, which allows one to choose a time that optimizes the signal-to-noise ratio.

So far, the discussion has been limited to the case of first-order sidebands whose transition probability scales with η^2 . However, the expression in Eq. 3.36 holds also true for higher-order sidebands (higher order in η). As mentioned in reference [105], the sensitivity of the method depends on choosing the order of the sideband used corresponding to the expected mean phonon number (i.e., using the first sidebands for $\langle n \rangle \approx 1$, the second for $\langle n \rangle \approx 2$, and so on). Especially in cases where higher phonon numbers are expected, this behavior is disadvantageous because the coupling between ion and laser scales as η^s , with s being the order of the sideband and $\eta < 1$. Thus, the probability to drive the transition decreases for a fixed amount of optical power. Therefore, the method's scope of application is often limited to the case of $\langle n \rangle < 1$.

The advantage of the method comparing the excitation on the red-sideband transition and the blue-sideband transition is its independence from the Lamb-Dicke factor, η , the carrier Rabi frequency, Ω and interaction time, t [70, 105]. If higher mean phonon numbers are expected, the method can be extended in the following way: Instead of varying the laser frequency ω_L for a fixed pulse length, t , and thereby extracting the ratio of the sideband excitations, the laser frequency is set to the red sideband and blue sideband respectively, $\omega_L = \omega_0 \pm \omega_m$, and the pulse length is varied. Such a setting leads to Rabi oscillations that represent the variation of the probability to find the ion in the excited state. These Rabi oscillations can be expressed as [70, 84]

$$P_e^{\text{RSB}} = \frac{1}{2} \left(1 - \sum_n \tilde{\rho}_n \cos(\Omega \eta_{\text{eff}} \sqrt{n} t) \right), \quad (3.37)$$

$$P_e^{\text{BSB}} = \frac{1}{2} \left(1 - \sum_n \tilde{\rho}_n \cos(\Omega \eta_{\text{eff}} \sqrt{n+1} t) \right), \quad (3.38)$$

with the effective Lamb-Dicke factor $\eta_{\text{eff}} = \eta \cos(\theta)$ defined by the angle θ between the propagation direction of the laser and the mode's direction of motion. A simultaneous fit to the Rabi oscillations on the red sideband and the blue sideband with one free parameter, $\Omega_{\text{eff}} = \Omega \eta_{\text{eff}}$, allows the extraction of the mean phonon number. In Fig. 3.8, theory curves for Rabi oscillations on the red sideband and blue sideband for increasing mean phonon number are presented. The decreasing probability to excite the ion on the blue sideband is accompanied by an increasing excitation probability on the red sideband, both tending towards 0.5.

Another technique that works to determine mean phonon numbers reached after Doppler cooling (typically $\langle n \rangle > 1$) is the observation of carrier Rabi oscillations. As described in reference [71] and more detailed in reference [106], the

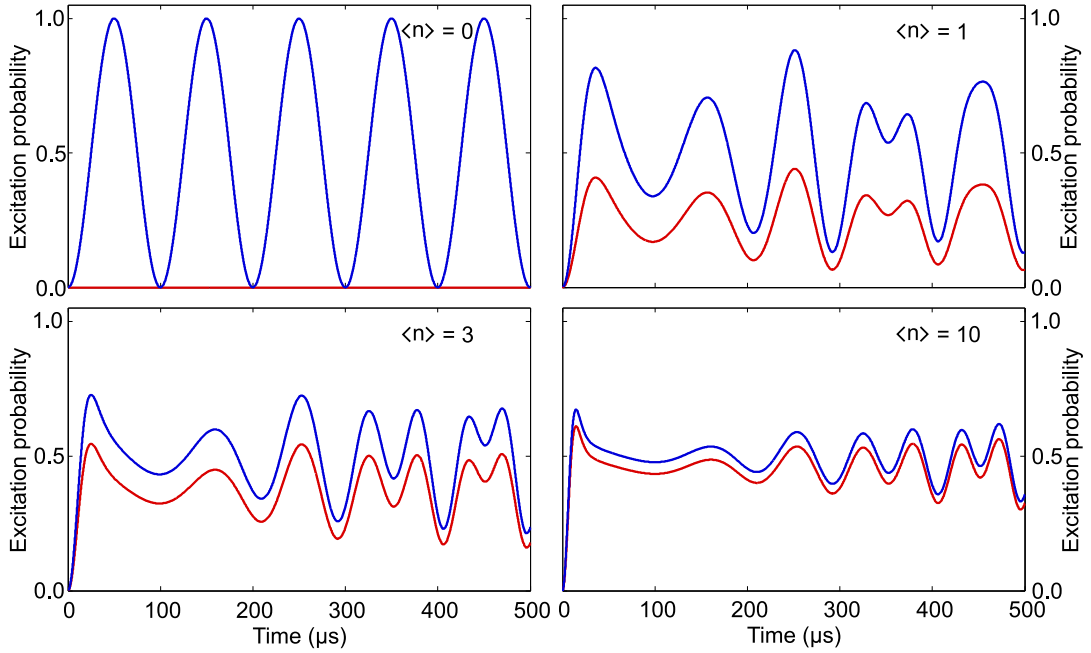


Figure 3.8. Rabi oscillations on red-sideband and blue-sideband transitions for varying mean phonon numbers $\langle n \rangle$. The thermal-state distribution $\tilde{\rho}_n$ sums over $n = 0 - 100$ and the effective Rabi frequency containing the effective Lamb-Dicke factor is set to $\Omega_{\text{eff}} = 2\pi \times 10$ kHz.

amplitude of these oscillations is damped due to the dependence of the Rabi frequency, $\Omega_{n,n}$, on the mean phonon number. From this dependence, it is possible to extract $\langle n \rangle$. This method relies on the coupling of a single motional mode to the laser.

While the methods presented are standard procedures used in ion trap experiments, they can only be applied to a single ion. Increasing the number of trapped ions leads to difficulties, as the vibrational excitations of the motional modes are shared between all the ions in the chain. For the single ion case, $n = 0$ is a dark state for the red-sideband excitation. With increasing ion number, the number of vibrational states not coupling to the red sideband increases. Thus, the measured ratio of the red-sideband and blue-sideband excitation probability does not allow the extraction of the mean phonon number.

Experimentally, it is possible to create a situation where only one ion within a multi-ion crystal is used for vibrational state measurements. A tightly focused laser beam is applied to one ion within the chain in order to carry out the mean phonon number measurement. This approach can be combined with previous laser pulses that transfer all other ions into an electronic state which does not couple to the tightly focused laser beam.

In the following subsections, two methods that do not rely on single-ion addressing are presented. The extraction of the mean phonon number from the global dynamics on the blue sideband relies on comparison of a theoretical simulation to the experimental data. The [rapid adiabatic passage \(RAP\)](#) method instead uses a direct mapping of the vibrational state onto the electronic excitation.

3.3. Measuring motional states of trapped ions

3.3.2 Motional-state dynamics on the blue sideband

Laser pulses acting on all ions in a crystal simultaneously yield a more complicated state evolution than for the single ion case as the ladder-scheme introduced in Fig. 3.2 has to be extended. In the following, a change in notation is carried out, denoting the ground state $|g\rangle = |0\rangle$ and the excited state $|e\rangle = |1\rangle$. For a two-ion crystal, a blue-sideband excitation on both ions simultaneously couples the ground state $|00, n=0\rangle$ with two singly excited states $|01, n=1\rangle$, $|10, n=1\rangle$. However, this intermediate state is also coupled to the excited state $|11, n=2\rangle$. Such a coupling is depicted in Fig. 3.9(a). Hence, the dynamics of the two-ion system driven by a global blue-sideband pulse which acts on both ions simultaneously can be presented as the probability to find none, one or two ions excited at a given time t , as illustrated in Fig. 3.9(b).

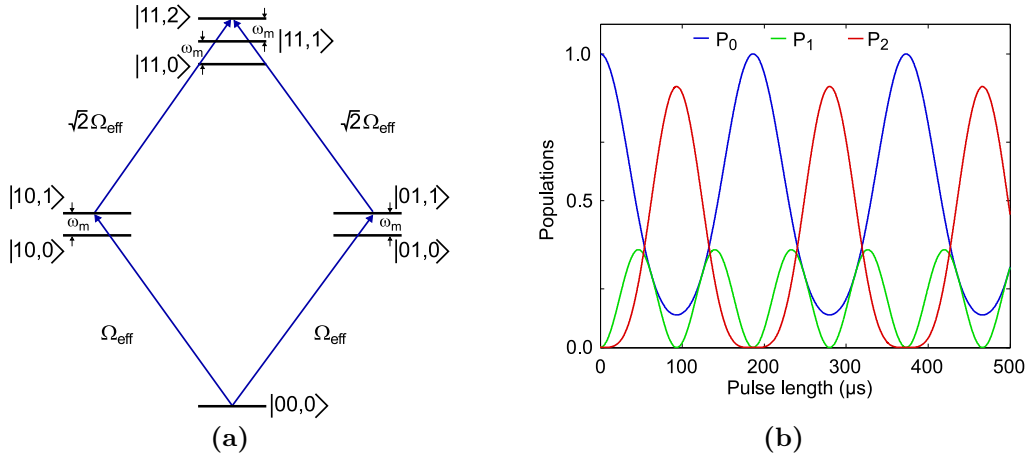


Figure 3.9. Global blue-sideband excitation of a two-ion crystal. (a) Application of a blue-sideband pulse on a two-ion crystal links the state where no ion is excited ($|00, n=0\rangle$) to those where one ion is excited and a phonon is added ($|01, n=1\rangle$, $|10, n=1\rangle$) and finally, to the state where both ions are excited and another phonon is added ($|11, n=2\rangle$). The coupling strength changes depending on the phonon number of the states and is proportional to $\sqrt{n+1}$ ($\Omega_{\text{eff}} = \Omega\eta_{\text{eff}}$). (b) State dynamics for a two-ion crystal interacting with a global blue-sideband pulse. The Rabi frequency on the blue sideband for both ions is $\Omega = 2\pi \times 150$ kHz, the Lamb-Dicke factor is $\eta = 0.0413$, and the detuning is set to zero. Initially, both ions are prepared in the electronic ground state and in the motional ground state: $|00, n=0\rangle$. The probabilities over time are plotted to find both ions in the ground state ($P_0(t)$), one ion excited ($P_1(t)$) or both ions excited ($P_2(t)$).

Extracting the vibrational state of the ion chain for a given mode that is excited by a blue-sideband excitation can be handled as a least-squares fitting problem. A theoretical simulation allows one to determine the expected oscillation frequencies for varying initial phonon numbers. For the two-ion crystal example, the probability amplitudes can be written as

$$P_{\text{gg}}(t) = P_0(t) = \sum \tilde{\rho}_n f_{\text{gg}}(t, n), \quad (3.39)$$

$$P_{\text{eg}}(t) = P_{\text{ge}}(t) = P_1(t) = \sum \tilde{\rho}_n f_{\text{ge}}(t, n), \quad (3.40)$$

$$P_{\text{ee}}(t) = P_2(t) = \sum \tilde{\rho}_n f_{\text{ee}}(t, n). \quad (3.41)$$

In these equations, the oscillating, time-dependent solution of the Schrödinger equation is represented by $f_{\text{gg}}(t, n)$ for no ion excited, $f_{\text{ge}}(t, n)$ for one ion excited and $f_{\text{ee}}(t, n)$ for both ions excited, with $\tilde{\rho}_n$ the probability weight representing the phonon-number distribution.

A least-squares fitting routine can be used to minimize the deviation between the simulated probability function and the experimentally measured evolution as

$$F(t) = \sum_{i,j} (P_i(t_j, n) - P_i^{\text{expt}}(t_j, n))^2 \quad (3.42)$$

with i an index over all possible populations and j an index over the time steps.

A more direct method of measuring the mean phonon number for a multi-ion crystal is represented by RAP, which is introduced in the following.

3.3.3 Rapid adiabatic passage

Rapid adiabatic passage (RAP) uses a chirped laser pulse, i.e., a laser pulse that changes in frequency and intensity, to transfer population from an initial state to a desired final state without population remaining in the intermediate states at the end of the experimental cycle. The laser frequency is changed in a way that allows an adiabatic following of the wave function. *Rapid* refers to the fact that the time scales on which the change takes place are small compared to the timescales defining the system, that is radiative lifetime and coherence time, i.e., the frequency chirp is faster than the system times [107, 108]. The method has been studied because of its ability to create non-classical states such as Fock states in the context of CQED [109], trapped single ions [110] and trapped N -ion crystals [111]. RAP has also been implemented as a robust technique to enable state preparation of a trapped ion in the field of quantum computing [112]. Furthermore, the technique offers the opportunity to create multipartite entangled states, like the so-called symmetric Dicke states [113]. The considerations on collective adiabatic passage to create Fock states [111] and Dicke states [113] serve as the starting point to introduce the mapping of the vibrational excitation shared between the ions within the chain onto the ions' electronic excitation.

For an N -ion crystal, we now study the case of exciting all ions simultaneously on the blue sideband with a single laser pulse. The laser detuning from resonance is set to $\Delta = +\omega_m - \tilde{\delta}(t)$, with $\tilde{\delta}(t)$ the linearly varying detuning of the laser. Furthermore, the Rabi frequency is assumed to be the same for all the ions in the chain, and it also exhibits a time dependence connected to the pulse shape [111]. For the experimental conditions studied in Ch. 6, the Rabi frequency pulse has a Blackman shape⁴ and can be written as [114, 115]

$$\Omega(t) = \frac{\Omega}{2} \left(0.84 - \cos\left(\pi \frac{t}{t_{\text{slope}}}\right) + 0.16 \cos\left(2\pi \frac{t}{t_{\text{slope}}}\right) \right), \quad (3.43)$$

with the carrier Rabi frequency, Ω , corresponding to the plateau of the pulse and a rising and falling slope with duration t_{slope} . Assuming that off-resonant

⁴In the following, the term Blackman shape refers to the definition as used in references [114, 115].

3.3. Measuring motional states of trapped ions

coupling to modes other than the COM mode is suppressed ($\tilde{\delta}(t) \ll \omega_m$ and $\Omega(t) < \omega_m$), the Hamiltonian in the *rotating wave approximation* is given by [111]

$$\hat{\mathcal{H}} = \frac{\hbar\Omega(t)}{2} \sum_{j=n}^N \left\{ \sigma_{+,j} \exp \left[i \left(\int_{t_i}^t \tilde{\delta}(\tau) d\tau - \omega_m t - \phi_j \right) \right] \right. \\ \left. \times \exp \left[i \frac{\eta}{\sqrt{N}} \left(\hat{a} e^{-i\omega_m t} + \hat{a}^\dagger e^{i\omega_m t} \right) \right] + H.c. \right\}. \quad (3.44)$$

In the Lamb-Dicke limit, this equation can be simplified as introduced in Sec. 3.1. Note that the single ion Lamb-Dicke factor η is used in Eq. 3.44. Since the equation is considering the COM mode, all ions couple to the light field in the same fashion altering the Lamb-Dicke factor by $1/\sqrt{N}$ [80, 111].

Simultaneous application of a chirped blue-sideband pulse on all ions leads to a system evolution from the common ground state $|0_1 0_2 \dots 0_{N-1} 0_N\rangle |n=0\rangle$ via time-dependent eigenstates to the final state $|1_1 1_2 \dots 1_{N-1} 1_N\rangle |n=N\rangle$, similar to the effect presented in the previous subsection. In general, the total system of N ions, n excited vibrations and one motional mode can be reduced to a system of smaller subspaces by a suitable change of basis. These subspaces are not interconnected by the Hamiltonian thus allowing a closed dynamic within each subspace. The basis transformation underlying this process is called *Morris-Shore factorization* [116, 117]. Its result is depicted in Fig. 3.10(a) for three ions, which are subject to a RAP process on the COM mode of the blue-sideband transition. The dynamics of the system is restricted to a four-state chain, with the detuning from the bottom increasing with increasing phonon number n . The coupling between the states scales with $\sqrt{n+1}$. The application of the Morris-Shore factorization allows a description of the problem in terms of an $(N+1)$ -level ladder coupling of the initial and final symmetric product states via $(n=1, \dots, N-1)$ multipartite entangled states.

A blue-sideband pulse acting on all ions leads to oscillations of the probability amplitudes for finding the crystal in a certain state, as presented in Sec. 3.3.2. However, if the laser parameters are changing slowly and thereby satisfy the requirements of adiabaticity⁵, as in RAP, the initial eigenstate adiabatically follows the excitation and the population is completely transferred to one final state. Fig. 3.10(b) shows the population evolution for a three-ion crystal from all ions in the ground state and zero phonons, $|000\rangle |n=0\rangle$, to all ions in the excited state and three phonons, $|111\rangle |n=3\rangle$.

Due to the symmetry properties of the Hamiltonian, interchanging two particles has no effect on the result of the calculation. Therefore, it is possible to generate symmetric Dicke states if RAP on the red sideband is used for an excitation number $n < N$ [113], as illustrated in Fig. 3.11.

However, this statement is only true for *rapid adiabatic passage* on a COM mode as in this case the coupling strength to the light field is equal for all ions. If a different mode is used, as was the case in the experiments presented in Ch. 6,

⁵The requirement to execute an adiabatic transfer is $|d\mathbf{W}/dt|/|\mathbf{W}| \ll |\mathbf{W}|$, with $\mathbf{W}(t) = (\Omega(t), 0, \tilde{\delta}(t))$ [112, 118].

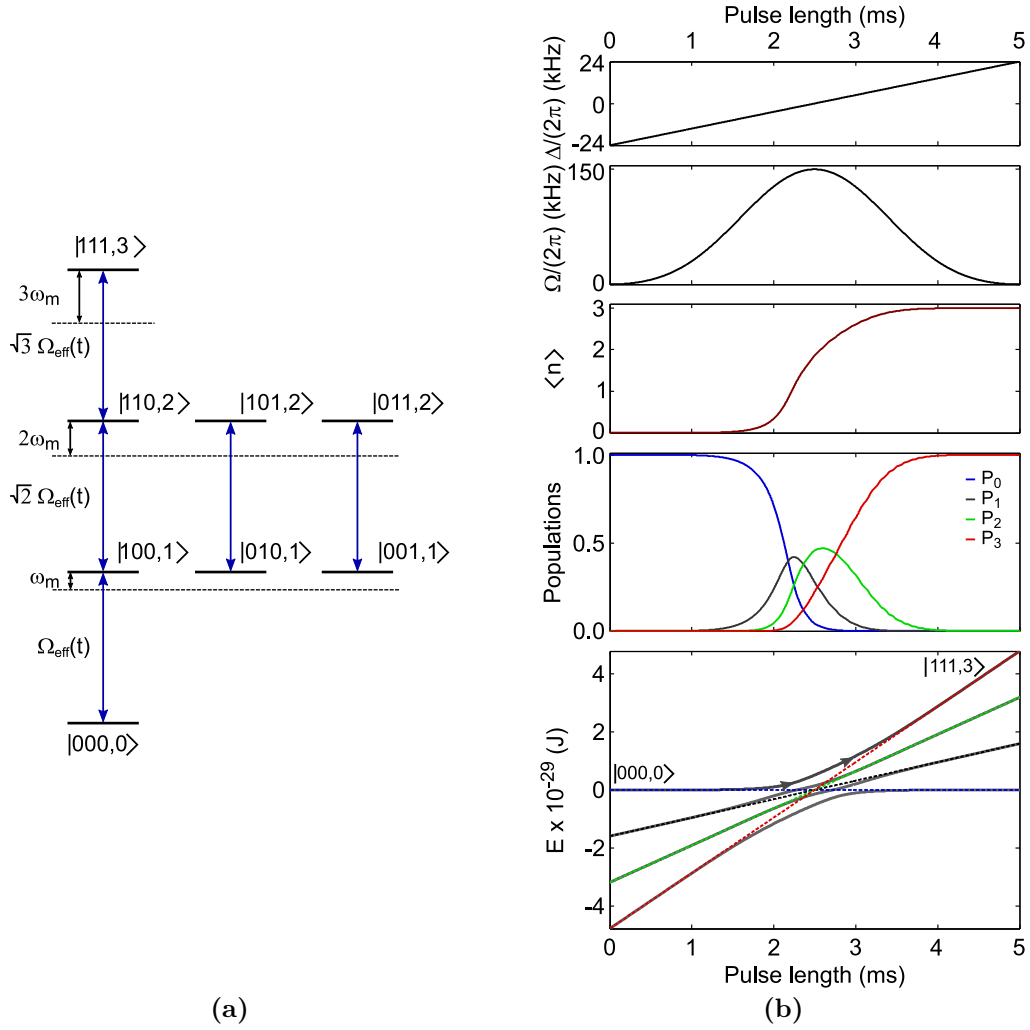


Figure 3.10. RAP applied across a blue-sideband at $2\pi \times 2.76$ MHz for a three-ion crystal. (a) Morris-Shore factorization, $\Omega_{\text{eff}}(t) = \Omega(t)\eta_{\text{eff}}$. RAP drives the three-ion crystal from the electronic and vibrational ground state $|000\rangle|n=0\rangle$ into a state in which all ions are excited and a Fock state of $n=3$ is reached ($|111\rangle|n=3\rangle$). Coupling strengths between the ladder rungs, which correspond to the number of phonons in the system, are proportional to $\sqrt{n+1}$. (b) Population evolution for RAP. The detuning is swept linearly across the transition frequency from $-2\pi \times 24$ kHz to $2\pi \times 24$ kHz. The Lamb-Dicke parameter is $\eta = 0.0413$, and the maximum Rabi frequency is $2\pi \times 150$ kHz, applied as a Blackman-shaped pulse. The ions are prepared in the ground state $|000, n=0\rangle$ and adiabatically follow the possible dressed states corresponding to one or two ions excited to reach the final state, $|111, n=3\rangle$, where all ions are excited and three phonons have been added to the system. The plotted eigenenergies represent the bare system (dashed lines) and the dressed system (solid lines), with arrows indicating the curve corresponding to the system evolution.

the coupling strength to the light field depends on the mode excursion for each ion and the resulting entanglement is weaker than for the COM mode.

For the measurement of the phonon number distribution, the process to create Fock states is inverted. RAP is applied across the red-sideband transition. Application of the red-sideband chirp allows a mapping of the phonon number onto the electronic excitation of the ions. After starting in an initial state

3.3. Measuring motional states of trapped ions

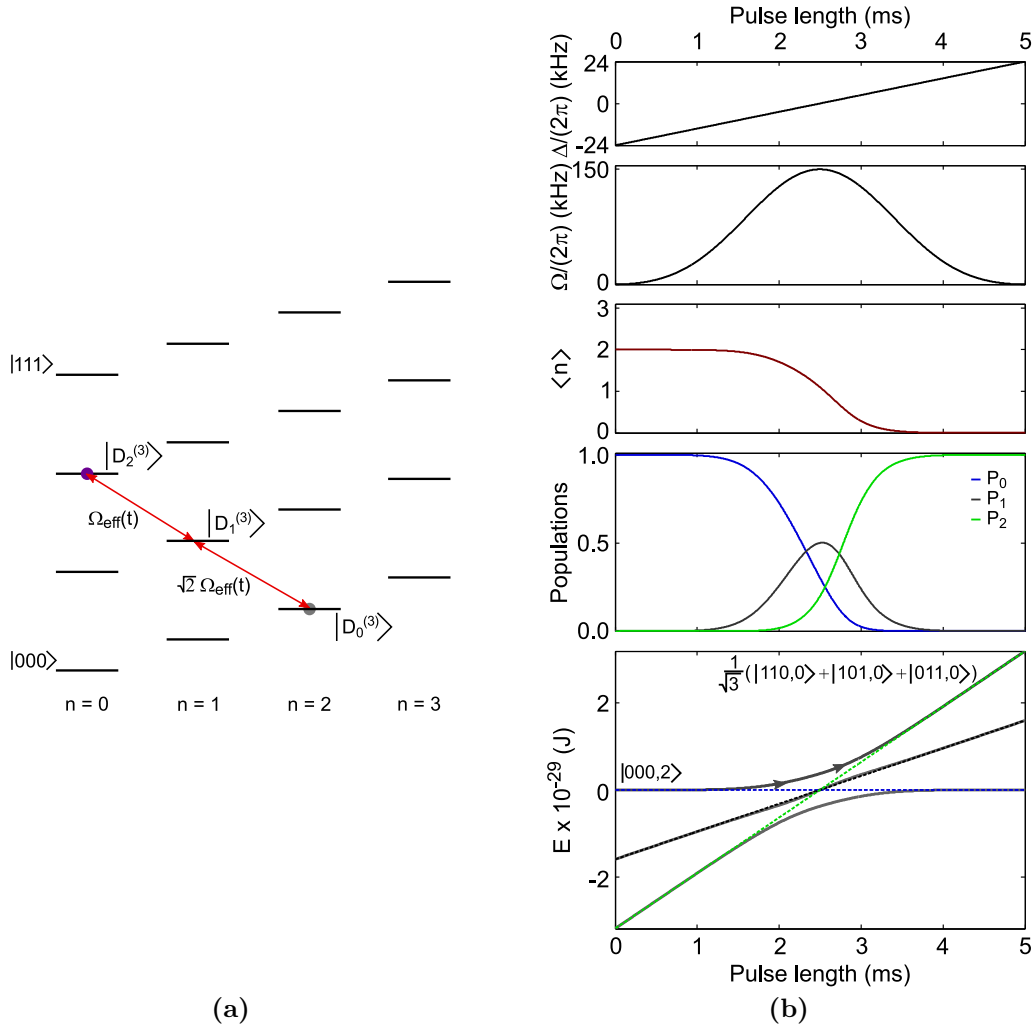


Figure 3.11. Dicke-state generation by RAP on the red-sideband transition of a three-ion crystal for $n = 2$. (a) Starting from a state $|000, n = 2\rangle$, RAP on the red sideband conserves the excitation number and maps the phononic excitation onto electronic excitations. The initial state is transferred to a multipartite entangled state corresponding to $|D_2^{(3)}\rangle = 1/\sqrt{3}(|110, 0\rangle + |101, 0\rangle + |011, 0\rangle)$. (b) RAP implemented on the red-sideband transition of the COM mode at 2.76 MHz for a three-ion crystal. The detuning is swept linearly across the transition frequency from $-2\pi \times 24$ kHz to $2\pi \times 24$ kHz. The Lamb-Dicke parameter is $\eta = 0.0413$, and the maximum Rabi frequency is $2\pi \times 150$ kHz, applied as a Blackman-shaped pulse. The ions are prepared in the electronic ground state but share an excitation corresponding to two phonons in the system: $|000, n = 2\rangle$. The plotted eigenenergies represent the bare system (dashed lines) and the dressed system (solid lines), with arrows indicating the curve corresponding to the system evolution.

$|0_1 0_2 \dots 0_{N-1} 0_N\rangle |n = N\rangle$, the system adiabatically follows the laser frequency chirp into an excited state $|1_1 1_2 \dots 1_{N-1} 1_N\rangle |n = 0\rangle$, as illustrated in Fig. 3.12. Then, the electronic excitation of the ions is read out using fluorescence detection [119–121]. The derived histogram for the number of excited ions reflects the phonon number distribution and allows the extraction of the mean phonon number $\langle n \rangle$ using a model fit. RAP allows the determination of the phonon number distribution for a multi-ion crystal with a single-shot measurement irrespective of the state’s

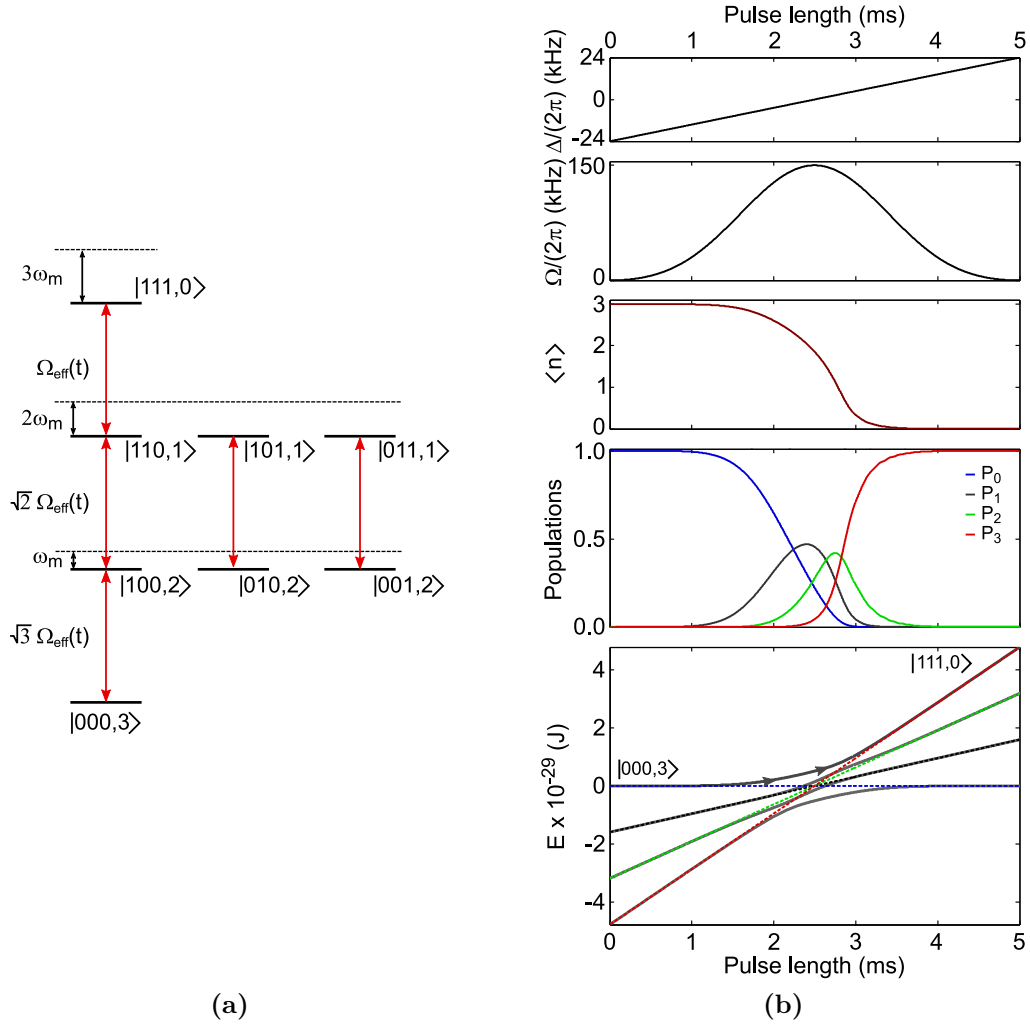


Figure 3.12. RAP applied across a red-sideband of a three-ion crystal at $2\pi \times 2.76$ MHz. (a) Morris-Shore factorization, $\Omega_{\text{eff}}(t) = \Omega(t)\eta_{\text{eff}}$. RAP drives the three-ion crystal with a Fock state of $n = 3$ ($|000\rangle|n = 3\rangle$) into a state in which all three ions are excited and zero phonons are in the chain ($|111\rangle|n = 0\rangle$). Coupling strengths between the ladder rungs, which correspond to the number of phonons in the system, are proportional to \sqrt{n} . (b) Population evolution for RAP. The detuning is swept linearly across the transition frequency from $-2\pi \times 24$ kHz to $2\pi \times 24$ kHz. The Lamb-Dicke parameter is $\eta = 0.0413$, and the maximum Rabi frequency is $2\pi \times 150$ kHz, applied as a Blackman-shaped pulse. The ions are prepared in the electronic ground state but share an excitation corresponding to three phonons in the system: $|000, n = 3\rangle$. Application of RAP allows a mapping of the three phononic excitations to three electronic excitations with a final state $|111, n = 0\rangle$. The plotted eigenenergies represent the bare system (dashed lines) and the dressed system (solid lines), with arrows indicating the curve corresponding to the system evolution.

nature.

The RAP process is simple to implement, robust against fluctuations of the laser frequency and intensity and allows fast state preparation since one single application allows the preparation of a large Fock state. It is versatile: implementation on the blue sideband allows preparation of large Fock states, while implementation on the red sideband allows the creation of multipartite entangled

3.3. Measuring motional states of trapped ions

states. Furthermore, RAP on the red sideband can be used to measure the mean phonon number in a multi-ion crystal. However, [rapid adiabatic passage](#) is limited concerning the mean phonon number extraction, since it is only possible to read out mean phonon numbers that are less or equal to the number of ions in the chain ($\langle n \rangle \leq N$).

Summary

This chapter presents theoretical considerations on the interaction between ions trapped in a harmonic potential and fields. For both a single ion and multi-ion crystals, the interaction Hamiltonian is introduced and a description of the state is given. Furthermore, laser cooling of trapped ions is reviewed as one important application of the atom-light interaction.

For a single-ion crystal and in cases where only a single or few modes need to be prepared close to the motional ground state, sideband cooling is commonly used. This technique uses excitation on the red-sideband transitions to pump the ion into the vibrational ground state, which is a dark state. For more ions and thus a denser mode spectrum, it is advantageous to use a different method that is capable of addressing several modes simultaneously.

In cooling processes, there is an interplay between the frequency range over which a method works and the minimum mean phonon number achievable. [EIT](#) cooling works efficiently over a broader frequency range than sideband cooling. The trade-off is that the minimum mean phonon numbers achieved by the process are in general higher than for sideband cooling. EIT cooling is implemented on two dipole-allowed transitions in a Λ -like level system. For trapped ions, EIT cooling uses destructive interference of two possible pathways to suppress the carrier transitions. Furthermore, a suitable choice of the induced light shift ($\delta = \omega_m$) leads to a cooling effect, as absorption on the red-sideband transition is more probable than other processes that induce heating for trapped ions.

Characterization of the cooling techniques requires measurement of the mean phonon number in the system. For a single trapped ion, this measurement relies on the different coupling strengths of the ion on the blue-sideband transition and the red-sideband transition. Measuring these quantities allows the extraction of the mean phonon number. However, for a multi-ion crystal the task is not as easily achieved as the vibrational state of the motional mode is shared over the whole crystal. Thus, measuring the excitation probability on red-sideband and blue-sideband transitions does not allow one to extract the mean phonon number. This is the case, as an inherent imbalance of the coupling strengths of the red-sideband and blue-sideband transitions leads to an asymmetry in the measured excitation probability even for $\langle n \rangle > 1$ (see also [Ch. 6](#)). The same holds true for Rabi oscillations on the red-sideband and blue-sideband transitions. However, the application of a tightly focused laser beam addressing only a single ion within the chain enables the extraction of the mean phonon number through Rabi oscillations.

Two methods to extract the mean phonon number for multi-ion crystals have

been introduced. One is based on the ion crystal interacting with a global blue-sideband pulse, leading to oscillating probability amplitudes that can be used to extract the mean phonon number by comparing experimental results with simulations. Furthermore, RAP has been presented, in which the phonon state is mapped onto the electronic excitation of the ion chain, and allowing the mean phonon number to be directly extracted.

4

The Microion-trap setup

A physical system that is used to realize a quantum computer has to fulfill a number of requirements [32]. While systems of trapped atomic ions in linear Paul traps have already been demonstrated to meet most of these criteria, it remains an outstanding issue whether these systems can be scaled up to larger numbers of trapped ions [68]. One way to increase the scalability of linear Paul traps is to use new trap designs based on “segmented trap arrays” [67]. With these new trapping geometries, the linear Paul traps’ limitations on effective manipulation of qubits can be overcome [122]. Additionally, the ability to shape the axially confining potential is gained. This property is of special interest for long ion chains, which can be more easily stabilized by an anharmonic trapping potential [57]. Furthermore, the use of higher-order multipole terms to generate the trapping potential enables confinement of equidistant ion chains [57].

This chapter introduces the segmented-trap setup used for the experiments presented in Ch. 5. In Sec. 4.1 both the trap and its vacuum system are presented. Sec. 4.2 introduces the laser systems necessary for experimental procedures and the optical setup to implement EIT cooling. Additional information on the construction of the system introduced in Sec. 4.1 and Sec. 4.2 can be found in M. Harlander’s thesis [84].

4.1 The trap and vacuum setup

One way of realizing three dimensional confinement of charged particles is by applying appropriate RF and DC fields [59]. The RF field provides trapping in the radial direction, and the DC field ensures confinement along the axial direction, as described in Ch. 2.

One condition for successful trapping is the absence of background particles, which if present would collide with the trapped ions. Such collisions would lead to chemical reactions or would disturb the ions from their equilibrium positions or change their energy or the electronic state. Hence, it is important to shield the ions from collisions by conducting experiments under ultra-high vacuum (UHV) conditions, typically at pressures of 10^{-10} mbar or lower.

Two-layer gold-on-alumina trap

The trap used for the results presented in Ch. 5 is a microtrap, which means that its dimensions are smaller than those of macroscopic linear Paul traps. Techniques from chip-fabrication have been applied in the manufacturing process. The trap is a product of joint European efforts within the STREP-Microtrap project and will be referred to as the Microion trap after the company which fabricated it¹. A trap from the same fabrication batch is described in detail in S. Schulz's thesis [123] and a review can be found in M. Harlander's thesis [84]. Here, the basic design parameters will be summarized.

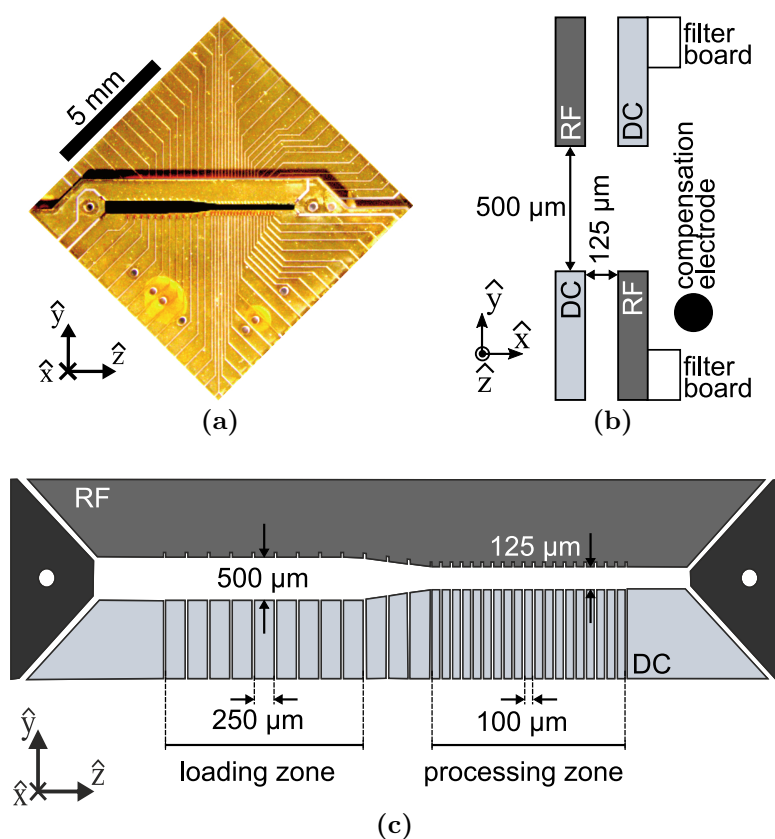


Figure 4.1. Microion trap schematic in plan view and cross section. (a) Plan-view photograph of the Microion trap. Ions align themselves along the z -axis, which is the trap axis. (b) Cross section of the Microion trap, depicting the two wafers consisting of RF electrodes and segmented DC electrodes, facing each other. In addition, both the filter board used to mount the trap (white) and the electrode added at the backside for micromotion compensation (black) are indicated. (c) Plan view of the Microion trap schematic with RF electrodes and segmented DC electrodes indicated. This illustration was adapted from reference [84].

The Microion trap is a two-layer gold-on-alumina sandwich trap, as illustrated in Fig. 4.1. It consists of two wafers that are separated by a $125\ \mu\text{m}$ thick spacer. Each wafer consists of an RF blade (non-segmented) and an array of DC electrodes (segmented), as shown in Fig. 4.1(c). The aperture separating the blades varies in width between $500\ \mu\text{m}$ in the so-called loading zone and $125\ \mu\text{m}$ in the so-called

¹Microion GmbH, Hannover

4.1. The trap and vacuum setup

processing zone. The two zones are separated by a tapered region in which the aperture width decreases linearly. The width of the DC electrodes varies from 250 μm in the loading zone and tapered zone to 100 μm in the processing zone. This trap geometry leads to an ion-electrode distance of 258 μm in the loading zone and 63 μm in the processing zone. A lower heating rate due to larger ion-electrode distance can be expected in the loading zone, which is why all experiments in the Micreon trap have been carried out in this region [73].

The RF voltage for radial confinement is provided by a digital synthesizer², after which it is amplified³ and sent through a helical resonator with a resonance frequency of 29.8 MHz. In this way, voltages oscillating at [radio frequency](#) with an amplitude of up to 800 V_{pp} are generated and applied to the electrodes.

The DC voltages used for axial confinement and micromotion compensation are provided by a commercial high-voltage power supply⁴ with a maximum voltage of ± 500 V. The trap can be operated with DC voltages of up to ± 15 V. However, the high-voltage power supply provides more stable voltages at higher output values. For this reason, a voltage divider (input:output ratio of 11:1) is implemented: the voltage output of the high-voltage power supply is on the order of several tens of volts, thereby exhibiting a lower noise level than at smaller voltage values, while only the eleventh part of this voltage is supplied to the trap. Hence, the high-voltage power supply provides voltage with a lower noise level while simultaneously preventing the Micreon trap from damage.

All applied DC voltages undergo two stages of low-pass filtering: The first stage is a home-built low-pass resistor-capacitor (RC) filter outside of vacuum (resistance of 160 Ω , capacitance of 1 μF , resulting in a cutoff frequency of 1 kHz). The second stage of RC filters is fabricated on an in-vacuum filter board manufactured at the University of Siegen (resistance of 2.8 k Ω , capacitance of 55 pF, resulting in a cutoff frequency of 1 MHz), where the filter board also serves as trap holder. These low-pass filters are necessary to reduce noise coupled to the electrodes from the driving electronics, as such noise can lead to heating of the ion. It was initially envisaged that the trap would be used for fast shuttling experiments, hence the high cutoff frequency of the in-vacuum filters.

A significant issue in the Micreon-trap setup is micromotion compensation. With the available DC electrodes, the ion's micromotion can only be compensated along one radial direction. Compensation in an additional direction is introduced by a gold-plated steel wire with a diameter of 2 mm that is attached to the backside of the in-vacuum filter board, as depicted in Fig. 4.1(b). Due to the segmentation of the DC electrodes, micromotion in one direction can be independently minimized in each trapping region. However, as the gold wire is not segmented, only a single compensation voltage can be applied to reduce the micromotion in the other direction.

²Rohde & Schwarz GmbH, SMB-01

³Mini-Circuits, ZHL-1-5W

⁴iseg Spezialelektronik GmbH, EHS-F-205x-F

Vacuum setup

The trap is mounted vertically on its filter board, i.e., with the y direction pointing physically upwards within a stainless steel vacuum chamber, as depicted in Fig. 4.2. All subsequent indications of direction refer to the physical lab frame as illustrated by the compass star in Fig. 4.2.

The trap axis is aligned at an angle of 15° to the east-west axis. The major vessel is a CF200 octagon with eight CF63 flanges attached to the sides. Six of these flanges can be used for optical access, while one has a blind flange attached (west side), and the one opposite (east side) connects to the vacuum-pump setup.

The pumps used are a $20\frac{1}{s}$ ion-getter pump⁵ and a titanium sublimation pump⁶. In addition, a Bayard-Alpert UHV gauge⁷ is used to monitor the pressure. All these devices can be separated from the rest of the vacuum vessel by a gate valve, if necessary. After the initial bake-out, the pressure within the vacuum vessel was measured to be 3×10^{-11} mbar and did not change significantly over a period of four years. In order to keep the pressure at this low value, the titanium sublimation pump was fired about once a year.

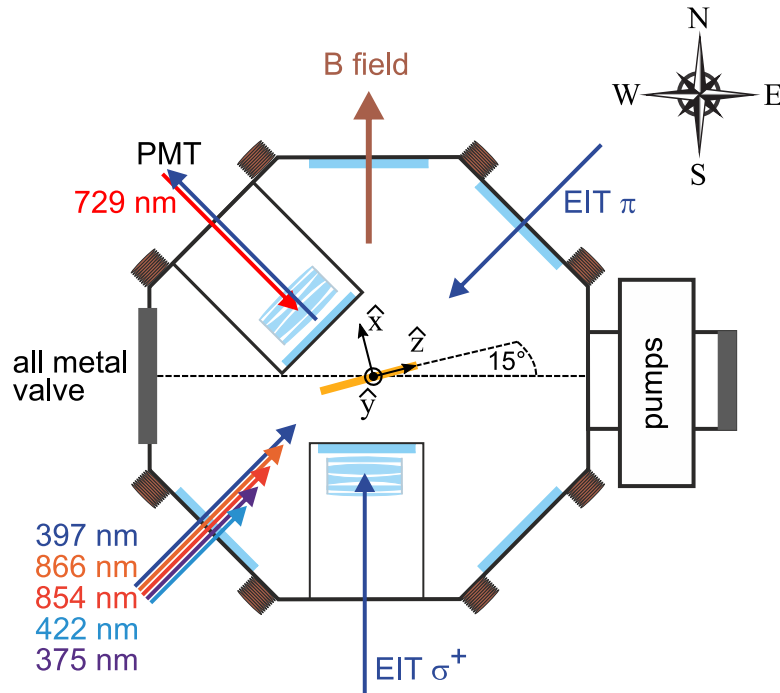


Figure 4.2. Top-view schematic of the vacuum vessel with orientation in the physical lab frame indicated by the compass star in the upper right corner. The lasers and their respective applications are introduced in Sec. 4.2. Four magnetic-field coils (brown) face north-east, south-east, south-west and north-west, generating a magnetic field pointing north. Of the eight viewports available, six offer optical access and two of these are inverted viewports.

Of the six flanges available as viewports, two are designed as inverted viewports (directed to the south and the north-west). These inverted viewports fa-

⁵Varian Inc., Starcell

⁶Varian Inc., TSP

⁷Varian Inc., UHV-24p

4.2. Laser setup

facilitate the positioning of optics close to the trapped ions (the distance between the trapped ions and the used objectives' ends are about 6 cm). A minimization of intensity losses is ensured by using windows that possess anti-reflection coating matched to the wavelengths used in the experiment (397 nm, 854 nm, 866 nm, and 729 nm; The photoionization lasers are not taken into account).

The top flange of the chamber (CF200) is used to mount the trap and offers three additional feedthroughs. The RF voltage is coupled into the vacuum chamber from a home-built helical resonator via a two-pin high-voltage connector within a CF40 flange. Another CF40 flange provides an electrical feedthrough for the home-built calcium oven, while a CF100 flange is used to connect the DC voltage supply with two D-Sub 50 connectors to the segmented trap electrodes.

4.2 Laser setup

In the experiments presented in this thesis, laser light is used to address selected electronic transitions of ^{40}Ca and $^{40}\text{Ca}^+$. The interaction of the ^{40}Ca atoms with the light field is used to generate ions. Subsequently, manipulation of the ions' electronic states is executed through the atom-light interaction to facilitate cooling, gate operations and imaging. The energy levels used during the interaction are depicted in Fig. 4.3.

In this section, the laser sources, major optical components and the sample-and-hold stabilization for the Doppler-cooling beams are presented. Furthermore, the setup built for EIT cooling is detailed.

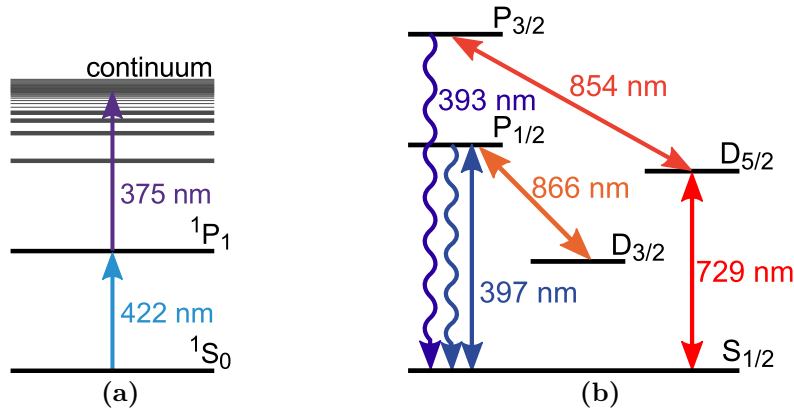


Figure 4.3. Level schemes of ^{40}Ca relevant for the experiments presented in this thesis. (Not to scale.) (a) Schematic of the levels and lasers involved in the photoionization process. As a first step, resonant light at 422 nm excites the atom to the $1P_1$ level. As a second step, off-resonant light at 375 nm excites the electron to the continuum. A singly ionized $^{40}\text{Ca}^+$ ion is thereby generated. (b) Level scheme and lasers used for the manipulation of $^{40}\text{Ca}^+$. Light at 397 nm in combination with light at 866 nm serves to cool and detect the ion. Quantum information processing and ground-state cooling are facilitated by the laser at 729 nm in combination with the laser at 854 nm. The transition at 393 nm is not externally driven, but photons at this wavelength are created due to spontaneous emission processes.

4.2.1 Photoionization lasers

The generation of ions from atomic calcium vapor is carried out by applying lasers at 422 nm and 375 nm wavelengths [124]. The process is comprised of two steps, as depicted in Fig. 4.3(a): a resonant excitation from the $4s^1S_0$ level to the $4p^1P_1$ level at 422 nm, followed by a non-resonant excitation at 375 nm to the continuum.

The light sources providing the necessary wavelengths are grating-stabilized diode lasers⁸ that are overlapped on a beam splitter (BS) and coupled into a multi-mode optical fiber to the experimental table. The output of the multi-mode fiber is overlapped with light at 397 nm on a band-pass filter⁹. Furthermore, light at 866 nm is added to these beams using another band-pass filter¹⁰. All four collinear beams are sent to the center of the trap's loading region.

4.2.2 Laser driving the $S_{1/2} \Leftrightarrow P_{1/2}$ transition

The laser operating at 397 nm couples the $S_{1/2}$ and $P_{1/2}$ state (see Fig. 4.3(b)). In combination with the 866 nm laser as a repumping beam, the 397 nm light is applied for Doppler cooling, to detect the internal state of the ion, to implement state initialization, and to implement EIT cooling.

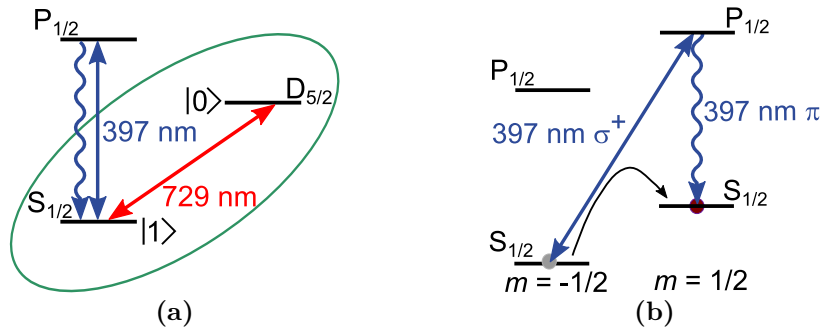


Figure 4.4. Level scheme of $^{40}\text{Ca}^+$ relevant for state discrimination and optical pumping. (a) Light at 397 nm is applied to distinguish whether the ion is in the $S_{1/2}$ state or has been excited by light at 729 nm to the $D_{5/2}$ state. If the ion is in the $S_{1/2}$ state (bright, $|1\rangle$), it can be coupled to the $P_{1/2}$ state, and a fluorescence signal is detected. However, if the ion is in the $D_{5/2}$ state (dark, $|0\rangle$), no coupling via 397 nm light can occur, and no fluorescence signal is measured. This scheme is the so-called electron-shelving method [119–121]. (b) Optical pumping using the 397 nm laser with σ^+ polarization. Population is accumulated in one electronic state to set the initial state of a quantum computation deterministically. Here, population is transferred from $|S_{1/2}, m = -1/2\rangle$ to $|S_{1/2}, m = +1/2\rangle$ and accumulates there.

4.2.2.1 State detection and state initialization

State detection distinguishes between a so-called bright state, the $S_{1/2}$ state, also referred to as $|1\rangle$, and a so-called dark state, the $D_{5/2}$ state, or $|0\rangle$, as illustrated

⁸TOPTICA Photonics AG, DL100

⁹Semrock Inc., FF01-395/11-25

¹⁰Semrock Inc., FF01-839/270-25

4.2. Laser setup

in Fig. 4.4(a). If population resides in the $S_{1/2}$ state, it will be excited to the $P_{1/2}$ state by light at 397 nm. The absorption of a photon at 397 nm excites the ion to the $P_{1/2}$ state from where it decays. The decay is accompanied by spontaneous emission of a photon at 397 nm. Thus, if the population is in the bright state ($S_{1/2}$), a fluorescence signal can be detected, for example, on a [photomultiplier tube \(PMT\)](#). However, if population is in the $D_{5/2}$ state due to prior excitation with the 729 nm laser, no photons at 397 nm can be scattered, and the fluorescence signal vanishes. This approach to state discrimination is known as the electron-shelving technique [119–121].

Additionally, the 397 nm light can be used for *state initialization* or optical pumping. The term *state initialization* refers to a process that deterministically prepares the starting state from which a quantum computation is executed. In $^{40}\text{Ca}^+$, such an experimental step can be carried out through accumulation of population in one of the two Zeeman sublevels of the $S_{1/2}$ state. In particular, by applying the 397 nm light with circular polarization, we implemented optical pumping, as depicted in Fig. 4.4(b).

4.2.2.2 EIT cooling

With ever more ions being used as resources in quantum information schemes and quantum simulation experiments, the need is growing for techniques that are able to cool several modes simultaneously. One auspicious candidate is EIT cooling [48, 49, 87]. The EIT cooling technique is based on quantum-interference effects within a Λ -type three-level scheme, as described in Ch. 3.

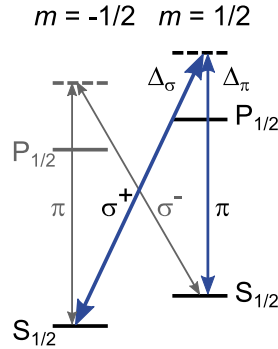


Figure 4.5. In $^{40}\text{Ca}^+$, the Λ -type level scheme to implement EIT cooling relies on the Zeeman sublevels of the $S_{1/2} \leftrightarrow P_{1/2}$ transition. Laser light at 397 nm drives the transition. The σ^+ beam induces strong coupling, creating dressed states of the $|S_{1/2}, m = -1/2\rangle$ level and the $|P_{1/2}, m = +1/2\rangle$ level, while the π beam is weak and used to access the Fano-type absorption profile created between the dressed states and the $|S_{1/2}, m = +1/2\rangle$ state.

For $^{40}\text{Ca}^+$, the Zeeman sublevels of the $S_{1/2}$ and $P_{1/2}$ manifolds are used to implement the Λ scheme necessary for EIT cooling, as depicted in Fig. 4.5. The linewidth of the $S_{1/2} \leftrightarrow P_{1/2}$ transition is $\Gamma = 2\pi \times 21.57 \text{ MHz}$ [97]. Efficient EIT cooling can be achieved for a detuning of the EIT beams from the $P_{1/2}$ level of $\Delta \approx 5\Gamma$.

4.2.2.3 The 397 nm setup

The following optical setup is presented in Fig. 4.6. Light at 397 nm is generated by frequency doubling the output of a **titanium-sapphire laser (Ti:Sa)**¹¹ at 794 nm. The Ti:Sa is pumped with light from a **diode-pumped solid-state (DPSS) laser**¹² at 532 nm. For frequency stabilization, a part of the 794 nm light is sent through an **electro-optical modulator (EOM)** to an external reference cavity and stabilized with a lock in **Pound Drever Hall (PDH)** configuration [125]. An external frequency reference of the same built is described in reference [126] and parameters for the system used here are given in reference [127]. Most of the 794 nm light is coupled into a frequency-doubling cavity in a bow-tie configuration¹³ with an integrated **lithium triborate (LBO)** crystal. This setup enables efficient frequency doubling from 794 nm to 397 nm light: For an input power of 720 mW, 80 mW of light are generated.

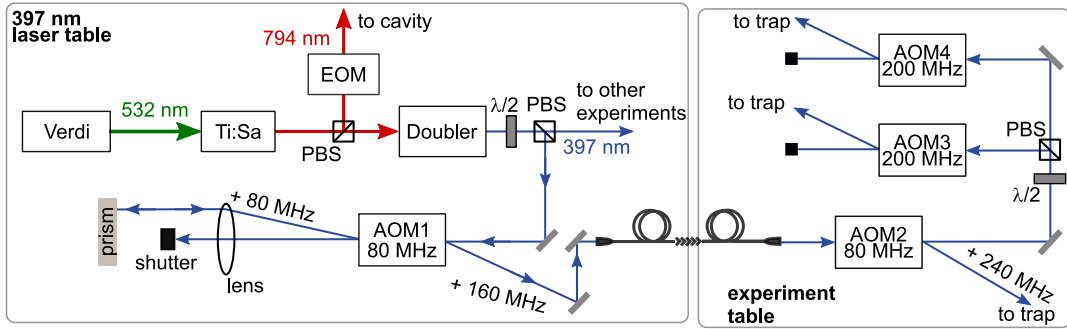


Figure 4.6. Optical setup for the laser at 397 nm used for Doppler cooling, detection, and EIT cooling. Detailed information of the setup can be found in Sec. 4.2.2.

The light generated by the doubling process is shared between four experiments. The light distribution is achieved by dividing the laser output using a cascaded system of $\lambda/2$ wave plates and **polarizing beam splitter (PBS)** cubes. An **acousto-optic modulator (AOM)**¹⁴ operating at 80 MHz and used in double-pass configuration enables individual frequency control for each experiment (AOM1 in Fig. 4.6). Therefore, the light at 397 nm picks up an additional frequency of 160 MHz before being coupled into a single-mode fiber to the experimental table. There, the light passes through another AOM at 80 MHz (AOM2), with which we shift the optical power within experimental sequences. Then, the light is coupled into a single-mode fiber and sent through the trap. Hence, due to the **AOMs** in the optical setup, the total frequency shift with respect to the cavity-stabilized light from the laser is 240 MHz.

After a mechanical shutter the undiffracted order of the double-pass AOM (AOM1) is coupled into the fiber to the experimental table. This red-detuned light (i.e., 160 MHz red-detuned from the ion's resonance frequency) is useful for

¹¹Coherent Inc., CR-899-21

¹²Coherent Inc., Verdi V10

¹³Spectra Physics, Wavetrain

¹⁴Brimrose Corporation of America, QZF-80-20-397

4.2. Laser setup

Doppler cooling of hot ions during loading and recrystallization of an ion chain after background-gas collisions.

As illustrated in Fig. 4.6, for the EIT cooling setup, the undiffracted order of the AOM at 80 MHz (AOM2) is sent through a PBS cube and split into two paths. Both paths are set up in a similar fashion, using the “+1” diffraction order of an AOM¹⁵ at a center frequency of 200 MHz (AOM3 and AOM4 in Fig. 4.6). The AOMs used are not ideal for the task at hand, since they are anti-reflection-coated at 850 nm instead of at 397 nm. While those AOMs were planned as an interim solution until AOMs with suitable anti-reflection coating could be purchased, a later exchange was not necessary: The additional light losses, which result in a coupling efficiency of about 50% in single-pass configuration, do not limit the performance of the EIT cooling scheme, for which only a few μW of optical power suffice. In the Microion setup, the maximum optical power used to achieve cooling of the highest motional mode at $\omega = 2\pi \times 4$ MHz corresponded to a Rabi frequency for the σ^+ beam of $\Omega_\sigma = 2\pi \times 40$ MHz. The Rabi frequency of the π beam was typically kept at a much lower value of approximately $\Omega_\pi = 2\pi \times 5$ MHz.

The light modulated by the AOMs is coupled into two single-mode fibers and thereby transferred to the relevant viewports. The π -polarized light is sent through a standard viewport at an angle of 45° to the magnetic field axis, and the σ^+ -polarized light is sent through an inverted viewport parallel to the magnetic field, as presented in Fig. 4.7.

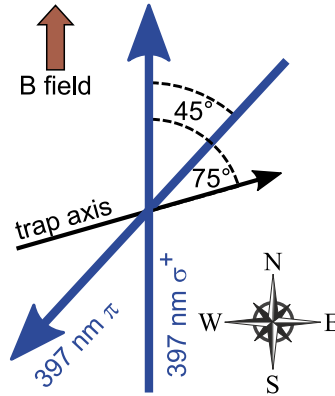


Figure 4.7. Top-view schematic of the laser beam alignment with respect to the trap axis. The orientation in the physical lab frame is indicated by the compass star in the lower right corner. The σ^+ -polarized light at 397 nm is oriented parallel to the magnetic field axis while the π -polarized light forms an angle of 45° with the magnetic-field axis. The resulting Raman k vector ($\mathbf{k}_\pi - \mathbf{k}_\sigma$) is in the plane of the table and has an angle of 52.5° with the trap axis, allowing the cooling of all motional modes. Compare Fig. 4.2 for a more complete overview.

The generation of purely π -polarized light would call for an angle of 90° with the magnetic field axis. However, due to the present limitations in the geometry of the vacuum setup, such a configuration is not easily achieved without breaking vacuum. Another possible solution, a change in magnetic field orientation, would lead to reduced coupling efficiencies for the quantum logic transitions at 729 nm.

¹⁵Crystal Technology Inc., 3220 120 for σ^+ , 3200 121 for π

Nonetheless, the difference between the ideal case and the real case is not a limiting factor for the experiments presented in Ch. 5.

4.2.3 Laser driving the $S_{1/2} \Leftrightarrow D_{5/2}$ transition

The laser at 729 nm is used to drive transitions between the states of the $S_{1/2}$ and $D_{5/2}$ manifolds, in which the qubit is encoded. As the $S_{1/2} \Leftrightarrow D_{5/2}$ transition is a dipole-forbidden transition, the lifetime of the $D_{5/2}$ state, 1.16 s [54], is determined by the quadrupole transition probability. The long lifetime of the metastable state is beneficial, since the decoherence rate for information stored in the qubit is not limited by it. Instead, processes on faster timescales such as fluctuations of the laser phase and the magnetic field limit the decoherence rate. However, the long lifetime also imposes stringent requirements on the linewidth and stability of the laser that drives the transition [128]. Hence, the 729 nm laser is a key feature for the implementation of quantum computations and quantum simulations.

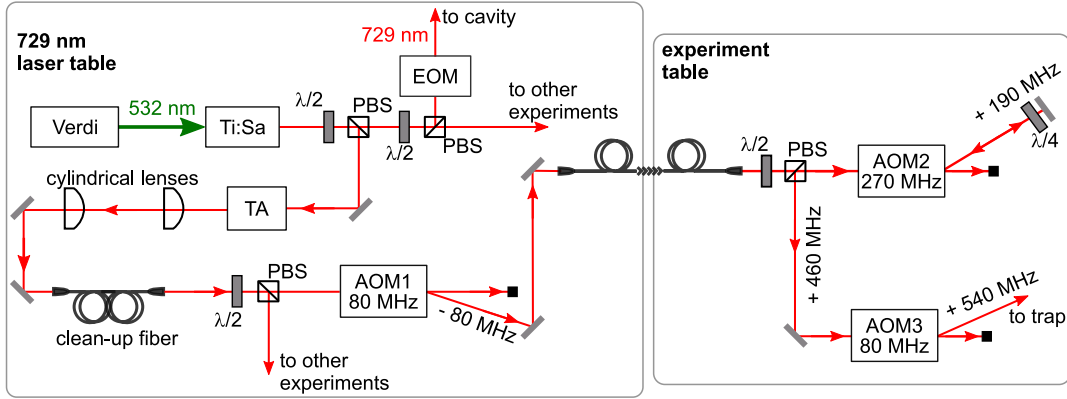


Figure 4.8. Optical setup of the quadrupole laser at 729 nm used for manipulation of the qubit. Detailed information of the setup can be found in Sec. 4.2.3.

The optical setup described in the following is depicted in Fig. 4.8. The light at 729 nm is generated by pumping a [titanium-sapphire laser](#)¹⁶ using a DPSS laser¹⁷ running at 532 nm. A fraction of the light produced is sent through an EOM to an external high-finesse resonator (finesse $\mathcal{F} = 479500(1600)$, linewidth $\Delta\nu = 4034(19)$ Hz [128]), to which it is locked via the PDH scheme. The resonator consists of ultra-low expansion (ULE) material. A frequency stability to within a few hertz and less can only be achieved with an active stabilization of the resonator's temperature as well as stabilization of mechanical vibrations. In addition, the frequency of the 729 nm laser is compared to the resonance of the $^{40}\text{Ca}^+$ ions using Ramsey spectroscopy in one of the experiments. The derived long-term drift of the cavity, which is on the order of a few Hz/s, is compensated for by adjusting the laser frequency using an [acousto-optic modulator](#) (not depicted in Fig. 4.8). Detailed information on the laser, the locking scheme and the high finesse reference cavity can be found in M. Chwalla's thesis [128].

¹⁶Coherent Inc., CR-899-21

¹⁷Coherent Inc., Verdi V10

4.2. Laser setup

With 8.5 W of pump power, the Ti:Sa produces 450 mW of light, which is distributed between the reference cavity, one experiment using a linear trap apparatus and a [tapered amplifier](#)¹⁸. With an input power of 25 mW and an operating current of 1.5 A, the [tapered amplifier \(TA\)](#) typically generates 200 mW of 729 nm light after a clean-up setup consisting of two cylindrical lenses and a single-mode fiber. This light is split between the three remaining experiments, of which one is the Microon experiment, using a cascaded system of $\lambda/2$ wave plates and PBS cubes.

Each experiment uses an AOM¹⁹ in double-pass configuration with a center frequency of 270 MHz for individual frequency control (AOM2 in Fig. 4.8). Therefore, the external reference cavity is required to be red detuned from the ion's resonance frequency by 540 MHz. In addition, an AOM²⁰ with a center frequency of 80 MHz (AOM1) is used to stabilize intensity. The stabilization scheme consists of this AOM (AOM1), a [photodiode \(PD\)](#) picking up part of the light after the fiber on the experimental table and a commercial [proportional-integral-differential \(PID\)](#) controller²¹. Intensity fluctuations at the experimental table are detected with the [photodiode](#). The voltage signal is compared to an internal voltage setting by the [PID](#) and the voltage determining the optical output power of the AOM is altered in order to match both settings. The unwanted additional frequency shift is canceled by another AOM²² with a center frequency of 80 MHz (AOM3) which is built into the setup using the reversed diffraction order (i.e., AOM1 is used in the -1 diffraction order and AOM3 is used in the $+1$ diffraction order). Finally, the 729 nm light is coupled through a custom-made objective²³ (focal length of 67 mm and numerical aperture (NA) of 0.28) that allows the beam to be focused onto a single ion within a string of several ions. Details of an objective with the same lens configuration but slightly different parameters can be found in reference [126].

4.2.4 Laser driving the $D_{3/2} \Leftrightarrow P_{1/2}$ transition

The laser at 866 nm couples the $D_{3/2}$ and $P_{1/2}$ manifolds. It recycles population that is lost via spontaneous emission to the $D_{3/2}$ state after an initial excitation on the $S_{1/2} \Leftrightarrow P_{1/2}$ transition by the laser at 397 nm (see Fig. 4.3(b)).

The optical setup described here is presented in Fig. 4.9. For some of the experiments presented in this thesis (those carried out before June 2013), the light was generated using a grating-stabilized diode laser²⁴. However, due to the need for more optical power, the system was exchanged for a grating-stabilized diode laser combined with TA²⁵. Frequency stabilization is carried out by sending part of the laser light through an EOM to an external reference cavity and implementing

¹⁸TOPTICA Photonics AG, TA100

¹⁹Brimrose Corporation of America, TEF-270-100

²⁰Crystal Technology Inc., 3080-122

²¹Stanford Research System, Inc., SIM960

²²Crystal Technology Inc., 3080-122

²³Sill Optics GmbH & Co. KG

²⁴TOPTICA Photonics AG, DL100

²⁵TOPTICA Photonics AG, TApr0

the PDH technique. An external frequency reference of the same built is described in reference [126] and parameters for the system used here are given in reference [127].

The laser output is shared between four experiments by a cascaded system of $\lambda/2$ wave plates and PBS cubes. In each experiment path, an AOM²⁶ in double-pass configuration with a center frequency of 200 MHz (AOM1) is used to control the 866 nm laser frequency. A total frequency shift of 400 MHz requires the frequency of the external reference cavity to be red detuned by the same amount from the resonance frequency of the ion.

The frequency-shifted light is coupled through a single-mode fiber to the experimental table, where it is overlapped with the 397 nm laser using a band-pass filter²⁷ as a dichroic mirror, then it is sent to the trap.

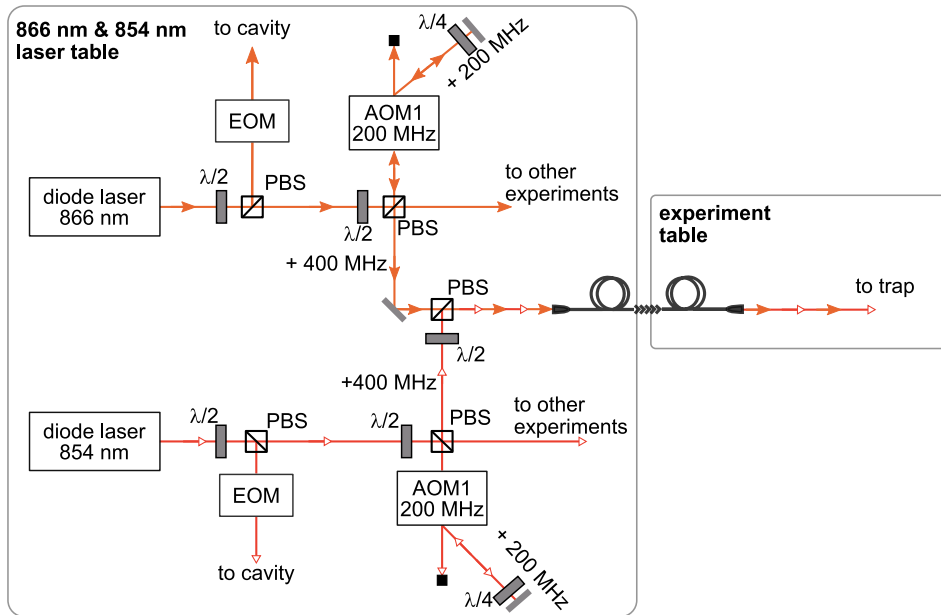


Figure 4.9. Optical setup for the 866 nm and 854 nm lasers used to recycle population from the $D_{3/2}$ state and to shorten the lifetime of the $D_{5/2}$ state, respectively. Detailed information of the setups can be found in Sec. 4.2.4 and Sec. 4.2.5.

4.2.5 Laser driving the $D_{5/2} \Leftrightarrow P_{3/2}$ transition

The laser at a wavelength of 854 nm couples the $D_{5/2}$ and $P_{3/2}$ manifolds. It is used to recycle population to the $S_{1/2}$ level via the $P_{3/2}$ level to shorten the lifetime of the $D_{5/2}$ level (1.16 s [54]) (see Fig. 4.3(b)).

The optical setup described here is depicted in Fig. 4.9 and is built in the same way as the setup for the laser at 866 nm. The light at 854 nm is provided by a diode laser²⁸, and frequency stabilization is achieved by sending part of the light through an EOM to an external reference cavity and applying the PDH locking

²⁶Crystal Technology Inc., 3200-124

²⁷Semrock Inc., FF01-839/270-25

²⁸TOPTICA Photonics AG, DL100

4.2. Laser setup

scheme. An external frequency reference of the same built is described in reference [126] and parameters for the system used here are given in reference [127]. Most of the 854 nm light is shared between four experiments using a cascaded system of $\lambda/2$ wave plates and PBS cubes.

Frequency control for each experiment is achieved by sending the 854 nm light through an AOM²⁹ with a center frequency of 200 MHz (AOM1), set up in double-pass configuration. The modulated light is then overlapped on a PBS cube with the 866 nm light and sent through a single-mode fiber to the experimental table. There, it is overlapped with the 397 nm light on a band-pass filter³⁰ and sent through the trap.

4.2.6 System control and data accumulation

With the exception of some manual adjustment procedures, the experimenter handles the major part of data taking using the experimental-control computer with a LabVIEW-based [graphical user interface \(GUI\)](#). The computer and software allow remote control of the following system components:

- analog and digital input/output cards³¹, which allow the direct control of frequency and amplitude of [AOMs](#);
- fast counter card³² for photon detection in connection with a [PMT](#)³³;
- digital signal generator³⁴, which supplies and controls the RF oscillation of the trap drive;
- pulse-sequencer box, which generates sequences of RF pulses with controlled frequency, amplitude and phase relationships (more details on the pulse-sequencer box can be found in the P. Schindler’s thesis [115]).

The experimental-control computer is furthermore connected via a controller-area-network (CAN) bus system to the voltage supply³⁵ for the trap’s DC electrodes that can be controlled with an additional LabVIEW-based GUI.

Aside from fluorescence data recorded by the PMT, visualization of the trapped ions is achieved by an [electron-multiplying charged-coupled device \(EMCCD\)](#) camera³⁶, which is controlled on a separate computer via the manufacturer’s original software³⁷.

²⁹Crystal Technology Inc., 3200-121

³⁰Semrock Inc., FF01-839/270-25

³¹National Instruments Corporation, NI-PCI6733 and PCI6703

³²National Instruments Corporation, NI-PCI6733

³³ET Enterprises Ltd, electron tube 9111B

³⁴Rohde & Schwarz GmbH, SMB-01

³⁵iseg Spezialelektronik GmbH, EHS-F-205x-F

³⁶Andor Technology Ltd., iXon

³⁷Andor Technology Ltd., Solis

4.2.7 Introduction of the sample-and-hold stabilization

In the Microeion setup, scans over several minutes revealed fluctuations in the maximum $D_{5/2}$ -state population, as depicted in Fig. 4.10 [data12a], [data12b]. Moreover, a variation in Rabi frequency was observed.

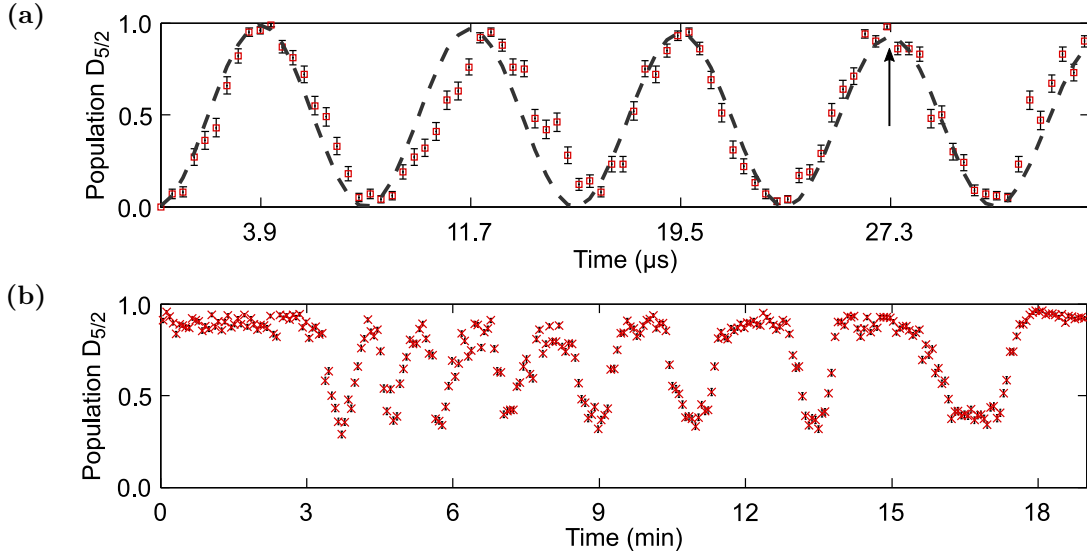


Figure 4.10. Rabi oscillations [data12a] and fluctuations of the maximum $D_{5/2}$ state population [data12b] on the carrier transition $|S_{1/2}, m = -1/2\rangle \leftrightarrow |D_{5/2}, m = -1/2\rangle$. (a) Rabi oscillations measured after Doppler cooling using a dark resonance. The Doppler limit at the trap frequency of $2\pi \times 1.6$ MHz is $\langle n \rangle \approx 6$ but due to the adjusted cooling technique the experimental value is lower [84]. A quantitative statement on the mean phonon number cannot be given for the presented measurement, as the damping necessary to achieve a significant fit was not observed on the observation's timescale (see Ch. 3). Error bars in the figure represent the uncertainty due to the finite number of measurements, so-called projection noise [129]. The observed oscillation frequency is $\Omega = 2\pi \times 127.2(6)$ kHz, derived from a fit, depicted as a dashed line. Even on time scales of several ten μ s, a comparison of the ideal Rabi oscillation as represented by the fit with the data shows discrepancies. (b) Long-term scan of the $D_{5/2}$ state population for a pulse length of 27.3μ s, indicated in (a) by an arrow. Over the scan time of 19 min, the population fluctuates between a maximum of 1.0 and a minimum of 0.3. Every data point corresponds to seven times more data per point than in (a).

The Rabi frequency is proportional to the electric field of the laser driving the transition and the transition dipole moment [49]. A variation of the maximum value of the Rabi contrast between 1.0 and 0.3, as depicted in Fig. 4.10(b), corresponds to a Rabi frequency variation of 9%. Such a fluctuation corresponds to a laser intensity fluctuation of 3%. However, the 729 nm light used for the measurement was intensity stabilized using a PID controller³⁸ excluding this as possible source for the observed behavior.

Another reason for the observed fluctuations could have been a deviation between the laser frequency and the transition frequency of the ion. Such a mismatch could be attributed to either the laser frequency or the magnetic field at the ion position being unstable. Again, the 729 nm laser could be ruled out

³⁸Stanford Research Systems, Inc., SIM960

4.2. Laser setup

as cause as it was stabilized to the resonance frequency of the ion [128]. The magnetic field that lifts the degeneracy between Zeeman sublevels was stabilized with a current stabilization from our institute’s electronics workshop with an achieved regular current stability on the order of 10^{-5} .

Furthermore, a change in the ion position during measurements thus changing the beam intensity seen by the ion was ruled out by observation of the ion position on the camera. Also, all electronic connections and the sources for the RF and DC voltages were checked to verify their stability.

Another possible source for the experimental observations was a fluctuation of the Doppler cooling beams. For Doppler cooling, the lasers at 397 nm and 866 nm are applied, as described in Ch. 3. After successful cooling to the Doppler limit, the ion is in the Lamb-Dicke regime. The quality of the cooling achieved relies on the frequency and the power of the Doppler cooling beams.

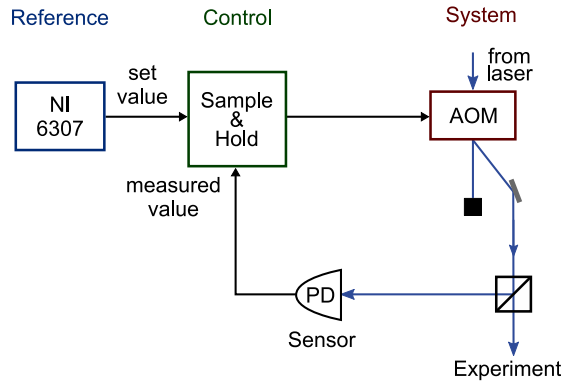


Figure 4.11. Sample-and-hold loop schematic. A reference is set with an analogue-output card (NI-PCI6703), which is compared to the signal measured by a photodiode (PD) with the sample-and-hold circuit. Accordingly, changes in the voltages applied to the system (AOM) are introduced to counteract differences between reference and measured signal.

In addition, the cooling scheme implemented in the Microon trap used *dark resonances* to improve Doppler cooling to below the Doppler limit [84]. The term *dark resonance* describes the situation, when a three-level Λ -like system coupled by two laser sources exists in a superposition of the two ground states, without any contributions from the excited state. For $^{40}\text{Ca}^+$, such a situation arises in the Zeeman sublevels of the Doppler cooling and repumping transitions, when there are no contributions of the $P_{1/2}$ level and the population exists in a superposition of the $S_{1/2}$ and $D_{3/2}$ states. The properties of dark resonances depend on a number of parameters as are: the intensity and frequency of both coupling lasers, their directions of propagation and polarizations as well as the direction and strength of the applied magnetic field [130]. “Dark resonance cooling” is achieved by choosing the parameters for the 397 nm and 866 nm laser in a way that creates an overlap between a dark resonance and a blue sideband. Thus, heating due to blue-sideband excitation is suppressed, and a final temperature below the Doppler limit can be achieved [84, 95]. However, cooling based on this effect is more susceptible to frequency and intensity fluctuations of the Doppler cooling beams.

Both the 397 nm laser and the 866 nm laser were frequency stabilized to an external reference cavity. However, both beams were coupled through fibers without

additional intensity stabilization, leading to intensity fluctuations of up to 20% for the 397 nm laser and of up to 5% for the 866 nm laser. Hence, a stabilization scheme on both optical paths was introduced.

The best stability at the location of the ion can be reached if the intensity of the Doppler cooling beams is monitored as close to it as possible. Thus, both PDs were introduced in the optical path at the experimental table, as close to the vacuum chamber housing the trap as could be achieved. However, the light in these paths, especially during experimental sequences, is not constantly on but pulsed with pulse durations varying between several tens of μs and several ms.

In order to allow the generation of light pulses with constant intensity within an experimental sequence, a sample-and-hold circuit was implemented. Such a device is favorable compared to a PID controller as it offers the functionality of a constant voltage output without continuous sampling events. The schematics of the system are illustrated in Fig. 4.11.

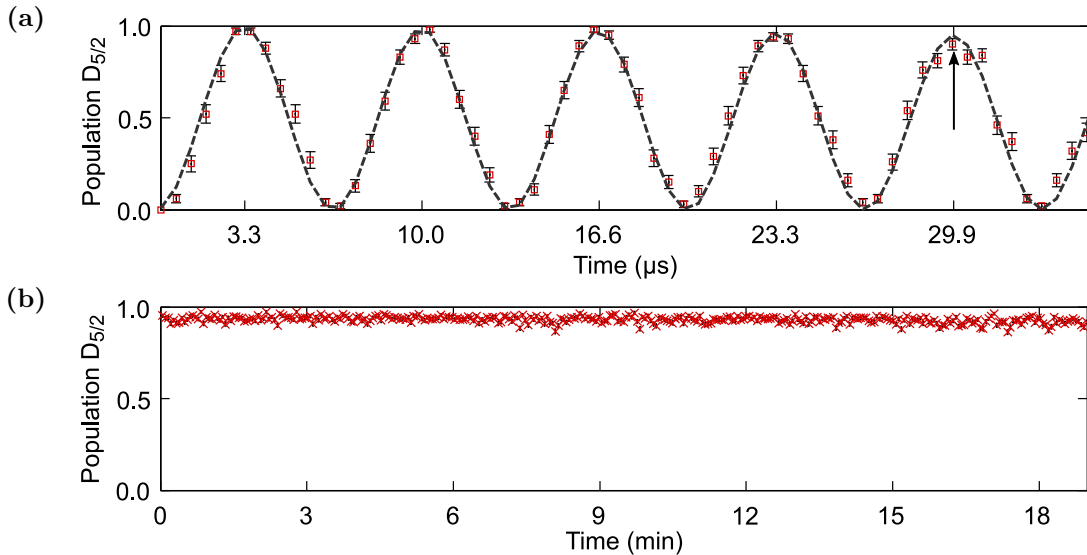


Figure 4.12. Rabi oscillations [data12c] and fluctuations of the maximum $D_{5/2}$ state population [data12d] on the carrier transition $|S_{1/2}, m = -1/2\rangle \leftrightarrow |D_{5/2}, m = -1/2\rangle$. (a) Rabi oscillations measured after Doppler cooling using a dark resonance [84]. The Doppler limit at the trap frequency of $2\pi \times 1.4 \text{ MHz}$ is $\langle n \rangle \approx 7$ but due to the adjusted cooling technique the experimental value is lower [84]. A quantitative statement on the mean phonon number cannot be given for the presented measurement, as the measurement was limited to a timescale on which no damping was observed (see Ch. 3). Error bars represent projection noise. The observed oscillation frequency is $\Omega = 2\pi \times 150.5(3) \text{ kHz}$, derived from a fit, depicted as a dashed line. (b) Long-term scan of the maximum $D_{5/2}$ state population for a pulse-length of $29.9 \mu\text{s}$, indicated in (a) by an arrow. Over the scan time of 19 min, the population fluctuates between a maximum of 1.00 and a minimum of 0.85. The measured fluctuations mark an improvement from the previous behavior illustrated in Fig. 4.10(b). Every data point corresponds to seven times more data point than (a).

Intensity stabilization of the Doppler cooling lasers used a small amount of light (around 4% of the total light in the path) picked off by a glass plate inserted into each beam path. This light was sent onto a photodiode³⁹ whose signal was

³⁹Thorlabs Inc., PDA36A-EC

4.2. Laser setup

compared by the sample-and-hold circuit to a set value, which was provided by an analog output device⁴⁰. The comparison of set value and measured value resulted in a feedback voltage that adjusted the amplitude of the signal fed into the double-pass AOMs of the 397 nm and 866 nm lasers. The sample-and-hold circuit was provided by our institute's electronic workshop.

Fig. 4.12 [data12c] [data12d] shows the improved behavior of the system after the sample-and-hold stabilization was implemented. Note that a quantitative comparison of Fig. 4.10 and Fig. 4.12 is not carried out, as the measurements have been executed at different trap frequencies.

Summary

In this chapter, an overview of the experimental setup used to achieve the results detailed in Ch. 5 is given. The ion trap and its vacuum system are introduced, followed by an overview of the laser sources used to drive the ion's electronic transitions.

The Microon trap is a two-layer gold-on-alumina sandwich trap that consists of segmented DC electrode pairs and one pair of RF blade electrodes. For the results presented here, segmented-electrode pairs within the loading zone with an aperture width of 500 μm and an ion-electrode distance of 258 μm are used to perform experiments. The microtrap is mounted vertically within a vacuum vessel, whose major part is a stainless-steel octagon with six viewports.

The generation and manipulation of calcium ions is achieved using diode and solid-state laser sources. All lasers except those for photoionization are frequency stabilized with a PDH locking scheme. The laser light is shared between four experiments.

During this thesis research, we improved the setup for the laser systems at 397 nm and 866 nm by implementing an intensity stabilization in a sample-and-hold configuration. In addition, we extended the 397 nm setup to enable EIT cooling.

⁴⁰National Instruments Corporation, NI PCI 6703

5

Multi-mode cooling in the Microion apparatus

The following results were measured using the Microion-trap apparatus, presented in Ch. 4. Sec. 5.1 summarizes the intended purpose and measurements for the Microion trap. It serves to motivate the course of action for the investigated cooling techniques: repetitive sideband cooling, as presented in Sec. 5.2, and [electromagnetically induced transparency \(EIT\)](#) cooling, as presented in Sec. 5.3.

5.1 Objectives for the Microion trap

The ion-heating rate is a measure for the vibrational excitation, i.e., the number of phonons, the ions accumulate per unit time. In general, it is advantageous that the ion-heating rate is slow with respect to the gate operation time. Thus, entangling-gate operations, which demand precise control of the vibrational excitation of the motional modes, can be carried out without a loss of information due to decoherence or dephasing effects.

The ion-heating rate is dependent on the trap type used in the experiments: For microtraps, it is higher than for macroscopic Paul traps [73]. Due to the higher heating rates in microtraps, it can even be difficult to carry out a trap characterization using a single ion: high vibrational excitation of neighboring motional modes leads to a heating of the mode employed in the experiments [37].

The Microion trap showed heating rates in axial direction, dependent on the trap frequency, between 300 phonons/s at a frequency of about $2\pi \times 1.6$ MHz and 4000 phonons/s at a frequency of about $2\pi \times 0.8$ MHz [84]. Despite the high heating rates observed, we envisioned the use of the Microion trap to generate higher-order multipole potentials that could confine equidistant ion crystals of at least ten ions. These ion strings would then be used to implement simulations like the quantum Ising spin model, which was recently investigated with up to eighteen ions [131–133]. The equal spacing and thus coupling between nearest neighbors that is provided by a higher-order multipole potential does not alter the results of the simulations for up to thirty ions confined in the potential. However, there will be a deviation for larger ion crystals where the equidistant spacing provided by, for example, a quartic potential, mimics the ideal case more closely. The Microion trap should provide a proof of principle experiment, which could later be scaled up to larger ion numbers.

Since sideband cooling a single ion was problematic in the early Microion trap characterization, Doppler cooling was modified to incorporate a dark resonance.

Chapter 5. Multi-mode cooling in the Microon apparatus

Application of this technique achieved temperatures below the Doppler cooling limit. More details on the method can be found in M. Harlander's thesis [84]. This cooling scheme improved the system performance and cooling well into the ground state was observed ($\langle n \rangle = 0.1$).

However, as reported in Ch. 4, Sec. 4.2.7, the system stability deteriorated. The implementation of the sample-and-hold circuit on the Doppler cooling beams improved the visibility of dark resonances on the transitions used for Doppler cooling ($S_{1/2} \Leftrightarrow P_{1/2}$ and $D_{3/2} \Leftrightarrow P_{1/2}$). In addition, the sudden fluctuations of the Rabi oscillation frequency were no longer observed. In spite of these improvements, the ground-state cooling capability could not be optimized to the previously observed level.

Therefore, an investigation of the system's heating rates was executed, incorporating not only the heating rate in axial direction but also in both radial directions for a single trapped ion. For this reason, a first measurement of the axial heating rate with axial sideband cooling only was carried out, to compare to the previous value given in reference [84]. Then, sideband cooling on the radial modes was implemented to allow heating rate measurements in this case. However, this did not prove successful as Rabi oscillations were only visible for the higher radial motional frequency.

We suspected that coupling to the uncooled modes with high vibrational excitation occurred, thus heating the cooled mode [37]. Therefore, we implemented repetitive sideband cooling to allow the observation of Rabi oscillations in all three motional directions. Results on these steps are summarized in Sec. 5.2.

Although the observed axial heating-rate measurements were comparable with the previously determined results, the achieved mean phonon numbers on the axial mode were still at $\langle n \rangle = 1$. Furthermore, the cooling time for repetitive sideband cooling prolonged the experimental cycle to more than 15 ms. Due to the high heating rates, it is preferable to have as short an experimental cycles as possible. Thus, we decided to implement EIT cooling as a means to shorten the cooling time duration by simultaneously cooling multiple modes.

Sudden loss of ions, which was already notable during our measurements using a double-well potential [55], increased over time. This prevented measurements involving more than two ions. In addition, the instability of quartic potentials prevented confinement of ions for longer than two hours. Since micromotion compensation in the Microon trap had to be adjusted after every ion-loading cycle, this behavior rendered measurements in the anharmonic configuration unfeasible.

For all mean phonon number measurements presented here, a different fit routine than in M. Harlander's thesis [84] was used, though the discrepancy in the mean phonon numbers cannot be attributed to this. The data presented in the following do not take into account an exponential decay depending on the mean phonon number and single ion coherence time. However, the data obtained for this work show no difference within the given error irrespective of the incorporation of such an exponential decay.

5.2. Repetitive sideband cooling

5.2 Repetitive sideband cooling

As described in Ch. 3, sideband cooling is implemented by driving a trapped ion with the 729 nm laser turned to a red-sideband transition frequency. The interaction of the ion with the red-detuned laser leads to a pumping of the vibrational excitation into a dark state, which is the vibrational ground state. This technique achieves low mean phonon numbers, but efficient cooling into the ground state works only for a narrow frequency range (approximately a few kHz).

As sideband cooling operates effectively only within the Lamb-Dicke regime, a pre-cooling scheme is necessary. In the Microon trap, a modified method of Doppler cooling has been introduced to achieve temperatures below the Doppler limit. Here, this method is referred to as dark-resonance cooling. It is described in detail in M. Harlander's thesis [84].

We have investigated sideband cooling using both one motional mode and all motional modes of a trapped single ion. The general experimental sequence used in the Microon trap is illustrated in Fig. 5.1.

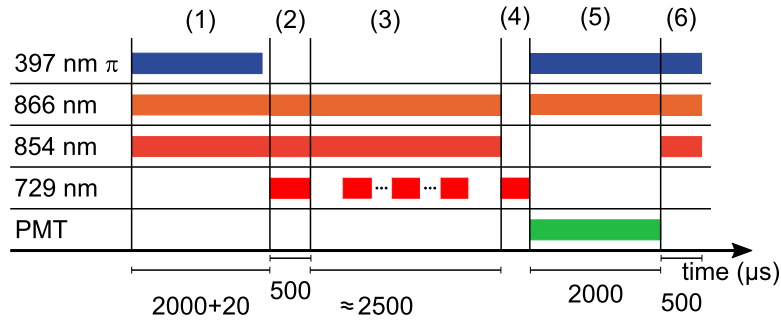


Figure 5.1. Experimental sequence for the Microon experiment. (1) The ion is initially cooled using dark-resonance cooling on the Doppler transition ($S_{1/2} \leftrightarrow P_{1/2}$). The closing of the cooling cycle is ensured by applying the infrared lasers at 866 nm and 854 nm for an additional 20 μs . (2) Thereafter, the population is accumulated in one of the ground states by optical pumping using the laser at 729 nm [128]. (3) For the experiments in this section, the ions were ground-state cooled using sideband cooling. One sideband cooling cycle consists of several 729 nm pulses on the red-sideband transition frequency accompanied by illumination with the infrared lasers. Furthermore, frequency-selective optical pumping is carried out in the beginning and the end of the sideband cooling cycle as well as between the red-sideband pulses. The duration of the cooling cycle varies depending on the number of red-sideband pulse repetitions and the number of modes cooled. (4) After these initial steps, the quadrupole laser is applied to manipulate the qubit state. (5) The electronic state of the ion is read out with the PMT using the electron-shelving method. (6) Each experimental sequence is ended by a repumping step, ensuring that the ion no longer populates the long-lived $D_{5/2}$ state.

5.2.1 Axial sideband cooling

Axial sideband cooling was implemented on a single trapped ion with trap frequencies $\{\omega_x, \omega_y, \omega_z\} = 2\pi \times \{4.59, 3.90, 1.38\}$ MHz. Rabi oscillations on the red sideband and blue sideband were observed and used to determine the heating rate for the motional mode at $2\pi \times 1.38$ MHz. The mean phonon number was extracted from the Rabi flops by fitting a thermal distribution simultaneously to

the red-sideband and blue-sideband traces, using an effective Rabi frequency Ω_{eff} , which incorporates the Lamb-Dicke factor η (see Ch. 3).

The ion was first cooled using the dark-resonance cooling scheme. Frequency-selective optical pumping using the 729 nm laser ensured state preparation in the $|S_{1/2}, m = -1/2\rangle$ state [128]. State initialization was followed by sideband cooling for 5 ms: The total sideband cooling cycle consisted of five repetitions with optical pumping using the 729 nm laser for 250 μs before and after a red-sideband pulse, which took 500 μs , each. Rabi oscillations on either the red sideband or the blue sideband were measured. The experimental cycle was closed by a repumping step, ensuring that all population was transferred back into the $S_{1/2}$ state.

Previous to the measurements presented here, the frequency of the 729 nm laser as well as the power of the 854 nm laser were optimized to achieve the lowest possible mean phonon number. Then, the described sequence was repeated for varying waiting times between the cooling step and the step where Rabi oscillations were driven. From this data, the heating rate induced by the noise coupling to the ion could be determined using a linear regression formula.

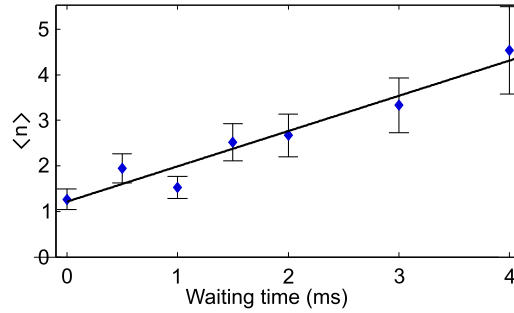


Figure 5.2. Heating-rate measurement for a single trapped ion with an axial frequency of $2\pi \times 1.38$ MHz [data12e]. The mean phonon number is obtained by fitting the measured Rabi oscillations on the red-sideband and blue-sideband transition simultaneously using an effective Rabi frequency of $\Omega_{\text{eff}} = 2\pi \times 20$ kHz. The heating rate is then obtained by fitting a linear regression model to the mean phonon number measured after different waiting times. Error bars are extracted from the covariance matrix of the fitting routine. The heating rate is determined to be 770(90) phonons/s.

A heating rate of 770(90) phonons/s was observed, as illustrated in Fig. 5.2 [data12e]. An effective Rabi frequency of $\Omega_{\text{eff}} = \Omega\eta_{\text{eff}} = 2\pi \times 20$ kHz was used to fit the red-sideband and blue-sideband oscillations simultaneously. The minimum mean phonon number observed without any delay between the cooling and the measurement step was $\langle n \rangle_{\text{min}} = 1.3(2)$.

The data obtained show cooling close to the vibrational ground state. The observed heating rate matches the expected value from previous measurements of approximately 700 phonons/s. However, the measured mean phonon number after cooling was higher by more than a factor of ten than for previous experiments, as described in Sec. 5.1.

Sideband cooling of a single motional frequency only allowed us to observe Rabi oscillations in one radial direction only. Thus, repetitive sideband cooling was implemented to allow the measurement of heating rates in all three directions of motion and in an attempt to decrease the mean phonon number after cooling.

5.2. Repetitive sideband cooling

5.2.2 Repetitive sideband cooling

Repetitive sideband cooling is based on consecutive application of sideband cooling on multiple modes. However, as the number of modes that are to be cooled increases, the cooling cycle duration increases as well. Modes cooled early in the cooling sequence have a longer time during which they can heat up compared to modes cooled later in the sequence. Therefore, modes that do not participate directly in the quantum computation as a means to mediate entanglement should be cooled first, and the mode to be used in the experiment should be cooled last. It is possible to implement gate operations using multiple motional mode frequencies since they factor out at the end of the computation. However, in most experimental implementations a single motional mode is used to mediate entanglement as this is more feasible.

A single ion with trap frequencies $\{\omega_x, \omega_y, \omega_z\} = 2\pi \times \{4.64, 3.90, 1.38\}$ MHz was used to test this cooling technique. Instead of the sideband cooling applied to the axial mode at $2\pi \times 1.38$ MHz only, the radial modes were also subsequently cooled. In total, the ground-state cooling step took 11.25 ms. The total cooling cycle consisted of five repetitions of the following steps: 500 μ s of optical pumping with the 729 nm laser, 500 μ s sideband cooling on the axial, 500 μ s sideband cooling on the first radial mode each, 250 μ s sideband cooling on the second radial sideband and again 500 μ s of frequency-selective optical pumping.

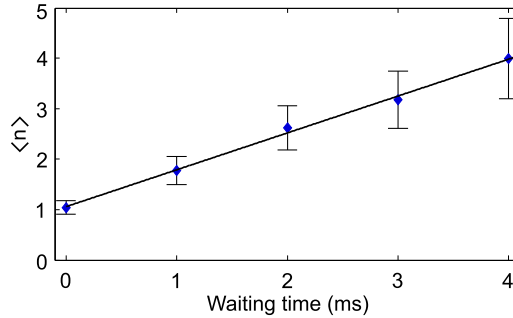


Figure 5.3. Heating-rate measurement on the axial mode for a single trapped ion [data12f]. The mean phonon number is determined by fitting the measured Rabi oscillations on the red-sideband and blue-sideband transitions simultaneously using an effective Rabi frequency of $\Omega_{\text{eff}} = 2\pi \times 28$ kHz. The heating rate is obtained by fitting a linear regression model to the mean phonon number measured after different waiting times. Error bars are extracted from the covariance matrix of the fitting routine. The heating rate is determined to be 730(10) phonons/s.

The frequency of the 729 nm laser and the power of the 854 nm laser was optimized previous to the experiments to achieve the lowest mean phonon number possible. After sideband cooling, Rabi oscillations were driven either on the red-sideband or the blue-sideband transition, followed by state detection. The results for the axial sideband at $2\pi \times 1.38$ MHz [data12f] are presented in Fig. 5.3, and the data for the radial sidebands at $2\pi \times 3.90$ MHz [data12g] and at $2\pi \times 4.64$ MHz [data12h] are shown in Fig. 5.4. The parameters extracted from the measurements are summarized in Table 5.1.

As Fig. 5.3 illustrates, the heating rate on the axial mode of $2\pi \times 1.38$ MHz after cooling all three motional modes is found to be 730(10) phonons/s. As

Chapter 5. Multi-mode cooling in the Microon apparatus

expected, this value is consistent within the stated error with the measurement presented in Fig. 5.2, in which only the axial mode was cooled to the ground state. Also, it is close to the heating rate of approximately 700 phonons/s, determined from earlier measurements detailed in reference [84]. The mean phonon number reached directly after cooling is $\langle n \rangle_{\min} = 1.0(1)$, which is lower by approximately 20% than for the case of axial sideband cooling only.

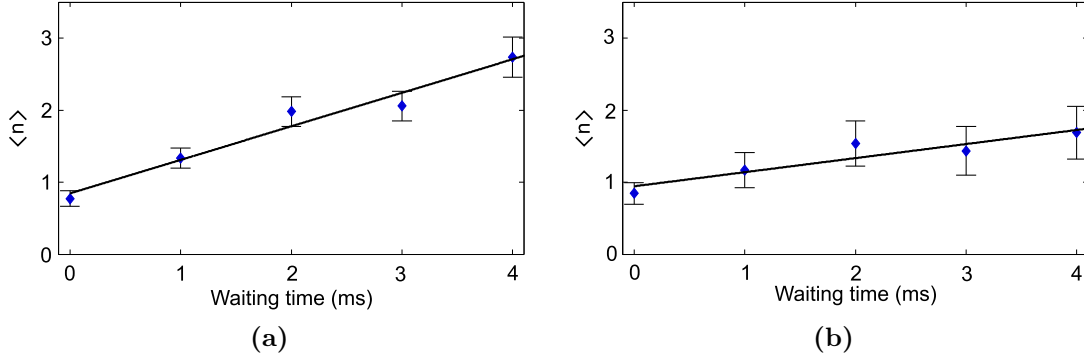


Figure 5.4. Heating-rate measurement on the radial modes for a single trapped ion. (a) Data obtained for the mode at $2\pi \times 3.90$ MHz [data12g]. The resulting heating rate is 470(50) phonons/s. (b) Data obtained for the mode at $2\pi \times 4.64$ MHz [data12h]. The resulting heating rate is 140(50) phonons/s. For both figures, the mean phonon number is determined by fitting the measured Rabi oscillations on the red-sideband and blue-sideband transitions simultaneously. The heating rate is obtained by fitting a linear regression model to the mean phonon number measured after different waiting times. Error bars are extracted from the covariance matrix of the fitting routine.

Fig. 5.4 illustrate the heating rates on both radial modes, which are 470(50) phonons/s for the mode at $2\pi \times 3.90$ MHz and 140(50) phonons/s for the mode at $2\pi \times 4.65$ MHz. The derived data show the expected linear increase of the mean phonon number with increasing waiting time between cooling step and measurement step. For the Microon trap, the presented data were the first characterization of the heating rate for the radial directions of motion. Note further that only through repetitive sideband cooling, which decreased the vibrational excitation of all motional modes, was it possible to record Rabi oscillations and thus heating rate measurements on the radial mode at $2\pi \times 3.90$ MHz.

mode frequency (MHz)	Heating rate (phonon/s)	$\langle n \rangle_{\min}$	$\Omega_{\text{eff}}/(2\pi)$ (kHz)
1.38	730(10)	1.0(1)	28
3.90	470(50)	0.8(1)	17
4.65	140(50)	0.7(1)	29

Table 5.1. Summary of the heating rates, minimum mean phonon numbers and effective Rabi frequencies obtained from the linear regression fits, which correspond to the solid lines in Fig. 5.3, Fig. 5.4(a), and Fig. 5.4(b).

The results presented in Table 5.1 show that the heating rate decreases with increasing mode frequency. It has been established for the Microon trap that the heating rate in the axial direction increases inversely proportional with the trap frequency [84]. The results summarized in Table. 5.1 mimic this behavior.

5.3. EIT cooling of a two-ion crystal

Note, however, that the presented heating rates are related to three different directions. Thus, it is also possible that there is different coupling to noise sources, which could also decrease the heating rate. Furthermore, the orientation of the directions of ion motion with respect to the 729 nm laser light leads to a difference in the coupling strength, since the overlap between each motional mode and the laser's propagation direction is different.

For the measurements presented in Fig. 5.3 and Fig. 5.4, the experimental cycle was optimized for the highest radial mode as the sideband cooling sequence always ended with this mode. Due to the ion-heating rate of 730 phonons/s observed previously on the axial mode (Fig. 5.2), that order leads to a heating of approximately 1.3 phonons for the axial mode at the end of the cycle. However, the minimum observed mean phonon number of $\langle n \rangle = 1.0(1)$ is lower than for sideband cooling of the axial mode only. One possible explanation for this behavior is that due to the cooling of the radial modes, vibrational excitation can also be extracted from the axial mode, thus counteracting the ion-heating and effectively decreasing the mean phonon number. This theory is supported by the fact, that only the implementation of the repetitive sideband cooling scheme allowed measurement of Rabi oscillations on the motional mode at $2\pi \times 3.90$ MHz.

Although the axial mean phonon number achieved with repetitive sideband cooling decreased in comparison to the axial sideband cooling case, it still deviated from older measurements by a factor of ten. Furthermore, the cooling cycle took in total 11.25 ms, which is unfavorable for the realization of a quantum computation, especially for traps with high heating rates. Thus, we focused on the implementation of EIT cooling, a technique that enables cooling of multiple motional modes simultaneously thereby shortening the total cooling time and preventing possible heating of modes during a repetitive cooling cycle.

5.3 EIT cooling of a two-ion crystal

As described in Sec. 5.2, the implementation of repetitive sideband cooling allowed the observation of heating rates on all motional modes of a single trapped ion. However, the cooling duration increased as well. Furthermore, the system could not be cooled as effectively as reported in earlier experiments (where $\langle n \rangle \approx 0.1$ [84]). Thus, the implementation of a cooling scheme that works on shorter timescales due to cooling multiple modes simultaneously, was envisioned. This consideration resulted in the implementation of **electromagnetically induced transparency (EIT)** cooling, which is a cooling technique that has a broad cooling bandwidth. Furthermore, EIT cooling is a versatile technique, which can also be implemented in anharmonic trapping potentials and for large numbers of ions [48]. These properties were well suited to achieve the objectives for the Microon trap (Sec. 5.1).

EIT cooling was first realized in Innsbruck in 2000 [49]. Although the technique proved to be easy to implement and working on a broad range of frequencies, sideband cooling, which achieves lower mean phonon numbers (see Ch. 3), was more widely used in the Innsbruck group. This can be attributed mostly to

the rigorous conditions of the Cirac-Zoller gate operation on the quality of the achieved ground state [28]. Although spin-dependent force gate operations have less strict requirements and also work on thermal states, it could be shown that the lower the achieved mean phonon number the better the gate operation performance [44, 47]. However, and especially for larger ion strings, the EIT cooling method regained popularity, due to its broadband cooling behavior.

Recently, a number of applications using EIT cooling have been reported: cooling of a nanomechanical resonator [53], cooling of a quantum-gas microscope [51], cooling of neutral atoms in cavity-QED experiments [52], and also as a cooling technique for mixed species multi-ion crystals in ion trap experiments [50].

In quantum computation, the broadband cooling property is especially interesting in conjunction with large ion crystals and gate operations based on the transversal motional modes [134]. As the transversal modes cover a narrower frequency range than the axial modes (see Ch. 2), one EIT cooling pulse is expected to allow addressing of all transversal modes simultaneously. This statement has been verified for up to eighteen ions in a macroscopic Paul trap, as is shown in Ch. 6.

However, EIT cooling has also been implemented for up to two ions in the Microon trap, enabling basic characterization of the technique's properties. This is, to our knowledge, the first successful implementation of EIT cooling in a microtrap of this type. Details on the experimental implementation concerning the beam setup in the Microon trap can be found in Ch. 4.

5.3.1 EIT beam characterization

Successful EIT cooling relies on the optimization of the cooling beams' frequencies, polarizations and intensities.

Frequency optimization

The frequencies of the cooling beams have to be set such that they are both equally blue detuned from their respective $S_{1/2} \leftrightarrow P_{1/2}$ resonance. A magnetic field of 0.33 mT is applied to generate a level splitting of 9.3 MHz between the $S_{1/2}$ Zeeman sublevels. This level splitting has to be taken into account in determining the frequency difference between the two beams. A measurement of the spectral line profile on the $S_{1/2} \leftrightarrow P_{1/2}$ Doppler cooling transition was used to set the detuning of $\Delta/(2\pi) \approx 105(10)$ MHz. Systematic errors, including a deviation between the used wavelength according to the wavemeter and the effective wavelength, during the line-center measurement accounted for the error estimate.

Optimization of the polarization

The magnetic field determines the splitting of the Zeeman sublevels and is chosen as quantization axis for the experiments presented. When an external magnetic field is applied, it is possible to address transitions between Zeeman sublevels with a difference in magnetic quantum number m of one ($\Delta m = \pm 1$) with circularly polarized light. Circular polarization is realized by aligning the light propagation

5.3. EIT cooling of a two-ion crystal

direction with the magnetic field axis. In the Microon setup, a quarter wave plate in front of the viewport was used to generate circularly polarized light from linearly polarized light at the output of an optical fiber. In order to achieve circular polarization, this wave plate was rotated. Optimization of the σ^+ polarization component was executed by minimizing the $|S_{1/2}, m = -1/2\rangle$ state population. The optimization was carried out by detecting the population in the $D_{5/2}$ state after executing a π pulse on the $|S_{1/2}, m = -1/2\rangle \Leftrightarrow |D_{5/2}, m = -1/2\rangle$ transition.

Due to the geometrical constraints of the setup, the π beam forms an angle of 45° with the magnetic field axis. As the ideal configuration for pure π -polarized light corresponds to a 90° angle between the magnetic field axis and the laser beam, the unwanted polarization components arising in this configuration cannot be completely suppressed. As discussed in reference [49], such a situation leads to an increase in the minimum achievable mean phonon number.

Determination of the induced light shift

Cooling of a distinct mode is achieved if the light shift induced by the σ^+ beam is equal to the motional frequency of this mode. Furthermore, the light shift induced by the π beam has to be kept much smaller than the σ^+ light shift. Therefore, determination of the induced light shift is integral to the characterization of the cooling beams and to setting up EIT cooling. The approach applied in the segmented trap setup determined the light shift from the optical pumping rate between the Zeeman sublevels of the $S_{1/2}$ state [97], as described in more detail in the following.

Fig. 5.5 presents the scheme and data [data14a] for the optimization of the light shift. Doppler cooling and preparation of the ion in the $|S_{1/2}, m = -1/2\rangle$ state are followed by illumination with the σ^+ EIT beam, which addresses the $|S_{1/2}, m = -1/2\rangle \Leftrightarrow |P_{1/2}, m = 1/2\rangle$ transition. In the next step of the experimental sequence, a π pulse on the $|S_{1/2}, m = -1/2\rangle \Leftrightarrow |D_{5/2}, m = -1/2\rangle$ transition is applied. This is followed by readout employing the electron-shelving technique and a repumping step to transfer all population from the D state to the S state.

For longer σ^+ pulses, more population is transferred to the $|S_{1/2}, m = 1/2\rangle$ state. Correspondingly, the population measured in $|D_{5/2}, m = -1/2\rangle$ is reduced, as presented in Fig. 5.5(c). The depletion of population by the σ^+ beam is determined by the spin flip rate, R , between the $S_{1/2}$ states [97]. This rate is in turn related to the induced light shift, δ , through the relations [97]

$$R = \frac{\epsilon_+^2}{3} \frac{\Gamma}{3} \left(\frac{\Omega_\sigma}{2\Delta} \right)^2,$$

$$\delta = \frac{\epsilon_+^2}{3} \frac{\Omega_\sigma^2}{4\Delta}.$$

The presented technique allows the extraction of the σ^+ Rabi oscillation frequency, Ω_σ , if the laser detuning, Δ , and the decay rate of the excited state, Γ are precisely known. In addition, a combination of both equations allows the extraction of the light shift, δ , from the spin flip rate, while the polarization amplitude,

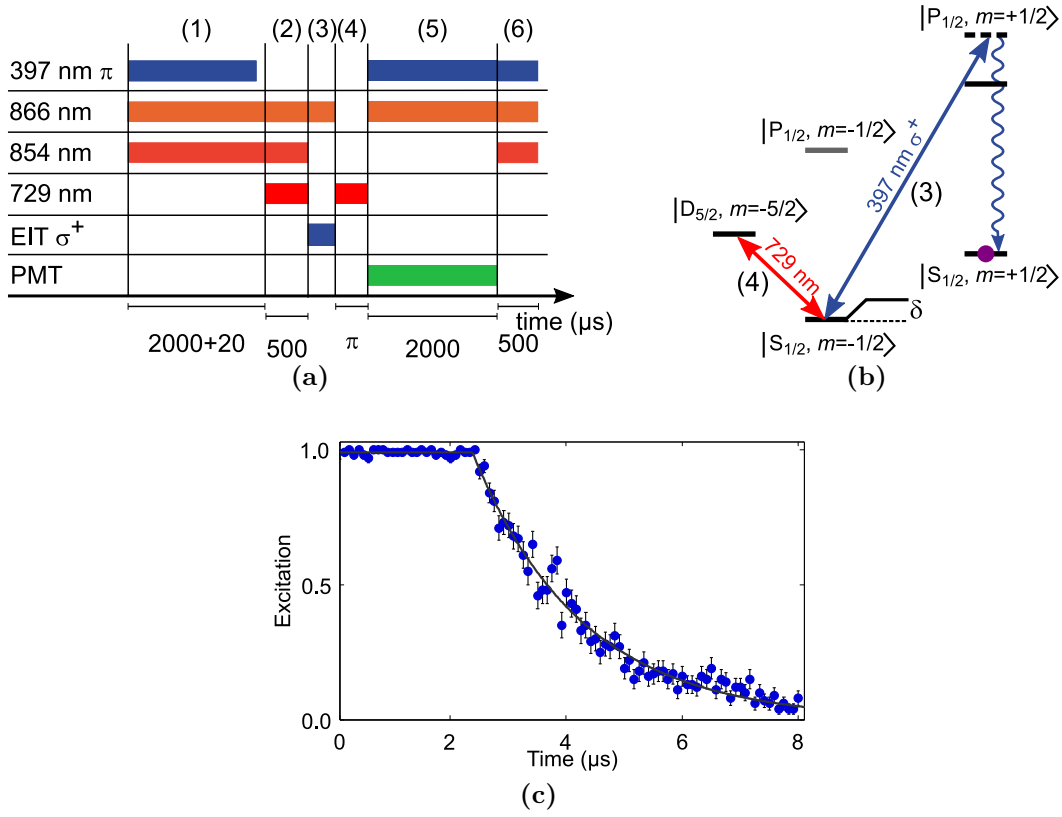


Figure 5.5. EIT light-shift optimization. (a) Pulse sequence detailing the steps to optimize the induced light shift. (1) Doppler cooling is applied, (2) followed by optical pumping using the 729 nm laser [128]. (3) Next, the population is transferred from the $|S_{1/2}, m = -1/2\rangle$ state to the $|S_{1/2}, m = 1/2\rangle$ state using the σ^+ light for EIT cooling together with the 866 nm laser as a repump. The duration of this step is varied between 0 μs up to 8 μs . (4) How much population remains in the $|S_{1/2}, m = -1/2\rangle$ state is measured by applying a π pulse on the $|S_{1/2}, m = -1/2\rangle \leftrightarrow |D_{5/2}, m = -1/2\rangle$ transition (5) and performing state detection with the PMT. (6) The experimental cycle is closed with a repumping step. (b) Level scheme used to optimize the light shift induced by the EIT σ^+ beam. (c) Experimental data of the $D_{5/2}$ population pump-out for increasing σ^+ pulse duration [data14a]. The delay of 2.5 μs corresponds to a signal delay in the sequence. Error bars represent projection noise. The black curve is a fit to the data as described in the main test, yielding an induced light shift of $\delta = 2\pi \times 1.22(5)$ MHz for a detuning $\Delta = 2\pi \times 104$ MHz and a fitted rate of $R = 530(20)$ kHz.

ϵ_+ , drops out. However, it is necessary to set the polarization exactly since the formulas are more complicated for mixed polarizations.

The light shift induced by the π -polarized beam is determined using the same method with adjusted equations. However, the expected signal for the state depletion, as shown in Fig. 5.5(c), approaches a steady state of 0.5 since π -polarized light leads to an equal population of both ground states. Ch. 6 presents a measurement technique that allows direct measurement of the light shift.

5.3.2 EIT cooling results

Typically, EIT cooling is applied in the sequence shown in Fig. 5.6. In the following, the characterization of EIT cooling applied to a two-ion crystal is presented.

5.3. EIT cooling of a two-ion crystal

Initial tests compared the efficiency of EIT cooling using either Doppler cooling or dark-resonance cooling as a first step. The efficiency of the EIT cooling scheme was independent of the pre-cooling method used. Hence, given that Doppler cooling is simpler and more robust than dark-resonance cooling, Doppler pre-cooling was used for the results shown here.

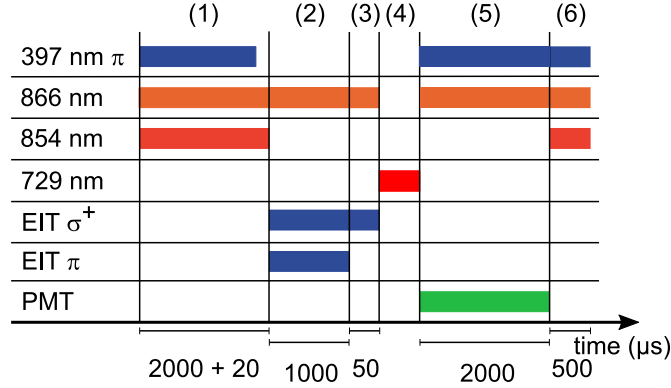


Figure 5.6. Experimental sequence for all measurements carried out with the Microon apparatus using EIT cooling. (1) Each experiment starts by Doppler cooling. (2) Thereafter, EIT cooling is the ground-state cooling technique used. (3) State initialization is performed by applying the EIT σ^+ beam for an additional $50 \mu\text{s}$ together with its repumper at 866 nm . (4) After these steps, the quadrupole laser is applied to manipulate the quantum-bit state. (5) The electron-shelving technique is used to determine the electronic state of the ion using the PMT. (6) A repumping step ensures that the ion's long-lived $D_{5/2}$ state is entirely depopulated.

The two-ion crystal used for testing the EIT cooling technique exhibited COM mode trap frequencies $\{\omega_x, \omega_y, \omega_z\} = 2\pi \times \{3.85, 3.29, 1.13\}$ MHz and rocking mode and stretch mode frequencies $\{\omega_{\text{rock}2}, \omega_{\text{rock}1}, \omega_{\text{stretch}}\} = 2\pi \times \{3.67, 3.09, 1.96\}$ MHz. Following the cooling step, the σ^+ beam was applied for an additional $50 \mu\text{s}$ to ensure state initialization. Then, Rabi oscillations on either the red sideband or the blue sideband of the $|S_{1/2}, m = 1/2\rangle \leftrightarrow |D_{5/2}, m = 1/2\rangle$ transition were observed. A simultaneous fit of a thermal distribution to the data obtained on both sidebands with an effective Rabi frequency Ω_{eff} resulted in the determination of the mean phonon number (see Ch. 3 and reference [104]).

As mentioned in Ch. 3, the method of comparing the Rabi oscillations measured after simultaneous excitation of both ions within a two-ion crystal cannot be used to extract the mean phonon number directly. One way to circumvent this problem is to address only one ion out of the two-ion crystal with the 729 nm beam and proceed with the comparison just as for the single-ion case. This approach was implemented for the results presented here, using a focused beam of 729 nm light on one ion, which resulted in a Rabi frequency on the carrier transition of $2\pi \times 1 \text{ MHz}$ for 7 mW of optical power. The distance between the ions was $5.5 \mu\text{m}$ (see Ch. 2, Eq. 2.12), and there is a residual part of the focused light that interacts with the neighboring ion. As a way to characterize the effect of this unwanted excitation, the ratio of the Rabi frequencies was determined, comparing the Rabi frequencies for the addressed ion and the neighboring ion [38]. For the measurements presented here, this so-called addressing error was 2% .

The cooling efficiency has been determined based on three measurements for

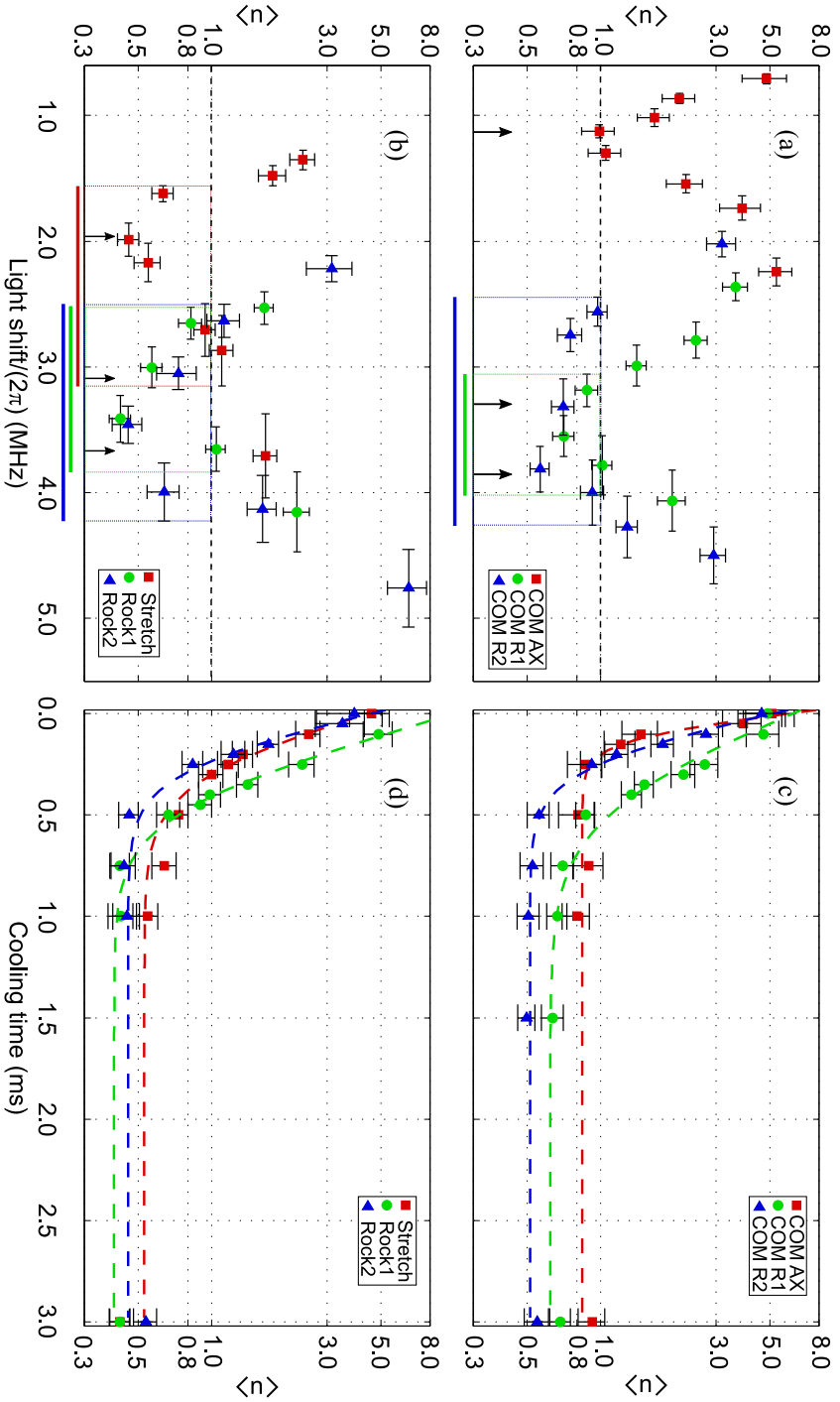


Figure 5.7. Cooling efficiency and cooling dynamics for all motional modes of a two-ion crystal. Measured minimum mean phonon number $\langle n \rangle$ with respect to varying light shift δ for the COM modes at $2\pi \times \{3.84, 3.29, 1.13\}$ MHz [data14b] (a) and for the stretch and rocking modes at $2\pi \times \{3.67, 3.09, 1.96\}$ MHz [data14b] (b); the light shifts resonant with the mode frequencies are indicated by arrows. The observed cooling range over which the mean phonon number is below 1 covers at least a bandwidth of 1 MHz with the exception of the axial COM mode. For better visibility, the cooling bandwidth for $\langle n \rangle < 1$ is boxed in and emphasized by colored lines along the x axis. Measured minimum mean phonon number $\langle n \rangle$ with respect to varying cooling times for the COM modes [data14c] (c) and for the stretch and rocking modes [data14c] (d). EIT cooling is a fast method compared to sideband cooling; here, cooling to the vibrational ground state is achieved within approximately 0.5 ms. The cooling rates are extracted from exponential fits, shown as dashed lines (see main text for details on the fit routine).

5.3. EIT cooling of a two-ion crystal

each data point presented in Fig. 5.7 (a) and (b): one to determine the induced light shift due to the σ^+ beam, and two to measure Rabi oscillations on the blue-sideband and red-sideband transitions for the extraction of the mean phonon number after applying the EIT beams for 1 ms. The mean phonon number achieved by EIT cooling with a given light shift can then be extracted. The light shift induced by the π beam is calibrated at the beginning of the measurement cycle and is not changed between individual measurements.

In both Fig. 5.7 (a) and (b) the mean phonon number decreases for a convergence of the σ^+ -induced light shift towards the motional mode frequency indicated by the arrows. In general, the cooling scheme achieves mean phonon numbers below $\langle n \rangle = 1$ for a frequency range of approximately 1 MHz around the motional mode frequency. The axial COM mode, which could only be cooled close to $\langle n \rangle = 1$, represents the only exception here. For optimized σ^+ light shift, minimum mean phonon numbers between 0.6 and 1.0 can be achieved for the COM modes and around 0.4 for the modes with out-of-phase ion motion. Note that the mean phonon number could be determined for all motional modes without the need for additional repetitive cooling steps. We attribute this to the broad cooling bandwidth — cooling acts on several modes simultaneously.

The general behavior of the curves matches the theory (compare Ch. 3, Fig. 3.7). As expected, for motional modes at lower frequencies the bandwidth to achieve low mean phonon numbers ($\langle n \rangle < 1$) is narrower. The cooling bandwidth, as indicated by the boxed-in areas and colored lines along the x axis, show clearly one advantage of EIT cooling as compared to sideband cooling: all modes with out-of-phase motion of the ions can be cooled simultaneously with one single EIT cooling pulse with an induced light shift frequency of about $2\pi \times 2.8$ MHz (Fig. 5.7 (b)).

The theoretically calculated values for the minimum mean phonon number obtained are on the order of $\langle n \rangle \approx 10^{-3}$. Comparison of the theory values with the measured values clearly show a discrepancy of more than two orders of magnitude. These deviations of the measurements presented in Fig. 5.7 (a) and (b) from the theoretically predicted minimum mean phonon numbers can be attributed to three main causes:

- The geometrical constraints of the Microon setup render perfect π polarization of the light field impossible. As described in reference [49], such imperfections lead to an increase in the minimum mean phonon number by approximately half an order of magnitude after cooling.
- The Zeeman sublevels of $^{40}\text{Ca}^+$ are an imperfect realization of the ideal Λ level scheme. The additional level ($|P_{1/2}, m = -1/2\rangle$) represents a deviation from the theory. Off-resonant coupling to this level increases the minimum achievable mean phonon number by at most half an order of magnitude as compared to the ideal three-level case.
- The heating rate present in ion traps — especially in microtraps — counteracts cooling but is not incorporated in the theory (Ch. 3, Sec. 3.2.3). The heating rate is identified as the main contributor to the deviation between

Chapter 5. Multi-mode cooling in the Microon apparatus

expected cooling behavior and experimental observations. We draw this conclusion as the contribution from the previously mentioned sources of deviation are too small to account for the total mismatch between experiment and theory.

mode frequency (MHz)	identifier	Cooling rate (10^3 phonons/s)
1.13	COM AX	17(7)
1.96	Stretch	7(2)
3.08	Rock1	7(1)
3.29	COM R1	5(1)
3.67	Rock2	9(2)
3.84	COM R2	9(2)

Table 5.2. Summary of the cooling rates obtained from the exponential fits, dashed lines in Fig. 5.7 (c) and (d), and the respective mode frequencies.

Results for the cooling dynamics [data14c] are presented in Fig. 5.7 (c) and (d). For each mode, the light shift, δ , was chosen to match the mode frequency. The cooling pulse duration was varied for each measurement and the mean phonon number was extracted from a simultaneous fit to the measured Rabi oscillations on the red-sideband and the blue-sideband transitions. The cooling rates for the various modes, summarized in Table 5.2, were determined using exponential fits to the data.

An exponential fit is appropriate because the dynamics of the mean phonon number can be described by the rate equation, $\dot{\langle n \rangle} = -r \langle n \rangle + r_h$, taking into account both the laser cooling rate, r , and the heating processes, r_h . The solution to this equation is $\langle n(t) \rangle = Ae^{-rt} + n_{\text{eq}}$ with A a constant and n_{eq} an offset term. A least-square fitting routine to the logarithm of the data ensured proper weighting of data points for longer cooling times.

All motional modes can be cooled below a mean phonon number of $\langle n \rangle = 1$ within 0.5 ms. Furthermore, the steady state after EIT cooling is reached within maximally 1 ms. Both plots show that the steady state after cooling is reached faster along the axial (AX) or second radial (R2) direction of motion as compared to the first radial (R1) direction of motion, specifically for the COM modes. The steady-state mean phonon numbers measured are higher by up to 30 % and more for the COM motional modes than for the modes with out-of-phase ion motion. We attribute this effect to the higher ion-heating rates for the [center of mass](#) modes.

The observations match the expected curve progression for $\langle n(t) \rangle$. The overlap between the Raman k vector and the direction of motion determines the coupling strength for the cooling scheme and thus, how efficiently a mode is cooled. However, the cooling rate values calculated from the theory (Ch. 3, Eq. 3.31) do not match the experimentally determined values. We attribute this mainly to the fact that the calculated coupling strengths are based on estimates of the overlaps between the Raman k vector and the directions of motion.

Due to the fast cooling rates, a 1 ms EIT cooling pulse was sufficient to effectively cool the ions into a steady state. This property, in combination with

5.3. EIT cooling of a two-ion crystal

the large cooling bandwidth depicted in Fig. 5.7 (a) and (b), advocate the use of EIT cooling for experiments with long ion crystals. As mentioned in Sec. 5.1, trapping instabilities for larger numbers of ions, i.e., more than two, prevented the characterization of the cooling technique for such cases in the Microtron trap. Thus, Ch. 6 presents observations for up to eighteen ions trapped stably in a macroscopic linear trap.

Summary

In this chapter, two approaches that allow cooling to the ground state of a motional mode are presented, both of which were implemented in the Microtron trap. Since the trap is a microtrap with a small electrode-ion distance, it exhibits high heating rates compared to macroscopic linear Paul traps. Thus, the trap operation can be improved by fast and effective cooling techniques to achieve ground-state cooling.

After our first sideband-cooling attempts failed due to the high heating rate, a pre-cooling step taking advantage of a modified Doppler cooling scheme was implemented, and sideband cooling of the axial mode into the ground state was achieved [84]. However, during the work presented here, the trap's stability deteriorated (see Ch. 4, Sec. 4.2.7) and higher mean phonon numbers were measured after axial sideband cooling. Thus, heating rate measurements were executed in order to compare them with previous values. The determined heating rate for axial sideband cooling was in accordance with the pre-determined value but the minimum mean phonon number was more than ten times larger than expected.

As a next step, repetitive sideband cooling was set up for the Microtron trap. This technique enabled heating rate measurements along all three axes. While only a slight improvement could be observed for the axial COM mode previously investigated with sideband cooling, the scheme allowed the first observation of Rabi oscillations and heating-rate measurements on both radial modes in the Microtron trap setup.

The cooling order for the various modes is sequential, and the first mode in the sequence, once cooled, will heat up until the cooling of the last mode in the sequence is finished. Therefore, simultaneous cooling of modes emerges as a desirable capability, particularly for systems with many motional modes. EIT cooling was implemented and analyzed, as it is a technique that satisfies this requirement.

From the results obtained with a two-ion crystal, it was determined that EIT cooling effectively cools the ions' motion to the ground state over a frequency range of approximately 1 MHz. Also, the cooling rates show that a reduction in cooling time compared to sideband cooling can be expected: For repetitive sideband cooling, about 65% of the experimental sequence duration is attributed to the ground-state cooling of three modes. This percentage increases for more modes cooled with this scheme. For EIT cooling, our findings show that one single pulse of 1 ms should suffice to cool all four radial modes of a two-ion crystal. Thus, the total duration of the experimental cycle decreases and the time

Chapter 5. Multi-mode cooling in the Microon apparatus

span attributed to ground-state cooling is about 15% of the complete sequence duration. These results demonstrate the feasibility of the EIT cooling scheme for increasing numbers of trapped ions as the cooling bandwidth is broad.

6

EIT cooling of long ion strings

The use of trapped atomic ions as quantum bits for a quantum computation offers a range of benefits like long coherence times and high readout efficiencies. However, an increase in the number of ions available as resources to expand the computational power poses a challenge [135]. There are varying approaches to increase the number of particles participating in a computation based on segmented traps: such traps can be used to facilitate shuttling [67, 136, 137] or to generate higher-order multipole potentials like, for example, potential wells with close proximity [55, 56]. However, it is also possible to trap multi-ion crystals (of twenty ions and more) in macroscopic linear Paul traps.

It is difficult to trap long ion strings in a stable one-dimensional crystal configuration: a lower limit for the ratio of radial to axial frequencies is based on the number of trapped ions [78, 79]. For fixed axial frequency, the radial frequency has to increase with a larger number of ions trapped. However, achieving high radial frequencies to counteract the repulsive Coulomb forces is experimentally difficult [75]. For macroscopic linear traps, thermal effects are one major obstacle that appear with high radial frequencies. For microtraps, the high voltages connected with high radial frequencies lead to a break down of the trap, most often starting with breaking wire bonds. For fixed radial frequencies, the axial frequency has to decrease with more ions confined. However, the duration to perform a gate operation is inversely proportional to the axial frequency. This drawback can be counteracted by implementing gate operations on the radial mode spectrum, which, in general, exhibits higher frequencies than the axial mode spectrum [134]. The use of the transverse mode spectrum is also beneficial since it is less sensitive to gate operation errors based on thermal motion and ion heating. There is still the challenge of cooling more modes in a reliable and fast fashion, as the mode spectrum density increases threefold with every ion added to the potential. In this situation, EIT cooling is a promising candidate to enable ground-state cooling.

While Ch. 5 presents the cooling scheme implemented for two ions in a segmented trap, in this chapter the full extent of the broadband cooling property of EIT cooling is explored for up to eighteen ions. Furthermore, novel means to characterize the cooling performance are introduced. These methods are applicable to multi-ion crystals. The mean phonon number, which is a parameter that quantifies the cooling process's impact, is determined based on an investigation of the dynamics for a global blue sideband excitation and rapid adiabatic passage.

All results presented in this chapter were obtained using the quantum simulation experiment (QSim) apparatus at the Institute for Quantum Optics and

Quantum Information (IQOQI), which due to the stability of trapped multi-ion crystals offers excellent conditions to test EIT cooling. Sec. 6.1 introduces the QSim setup; (a detailed description can be found in C. Hempel’s thesis [138]). Sec. 6.2 discusses the motional state analysis, and Sec. 6.3 presents the EIT cooling results.

6.1 The linear-trap setup

The principles of operation of the Microion setup presented in Ch. 5 and the linear trap setup of QSim at IQOQI are very similar. In both experiments, trapped $^{40}\text{Ca}^+$ ions serve as a physical realization of quantum bits, and laser-ion interactions enable cooling, information processing and detection. Details on the electronic transitions used are given in Sec. 4.2 and, together with more information on the QSim setup, in reference [138].

In the following, an overview of the QSim setup is given. A brief presentation of the trap and vacuum system is followed by a summary of the laser sources. In addition, the EIT cooling setup is introduced.

6.1.1 The linear ion trap and vacuum vessel

The linear Paul trap

In contrast to the ion trap described in Ch. 4, which is a segmented microtrap, the QSim trap is a macroscopic linear Paul trap, designed and manufactured by S. Haslwanter of IQOQI. A schematic is depicted in Fig. 6.1. The trap consists of four blades and two endcap electrodes secured within a Macor[®] holder that provides precise alignment and electrical isolation.

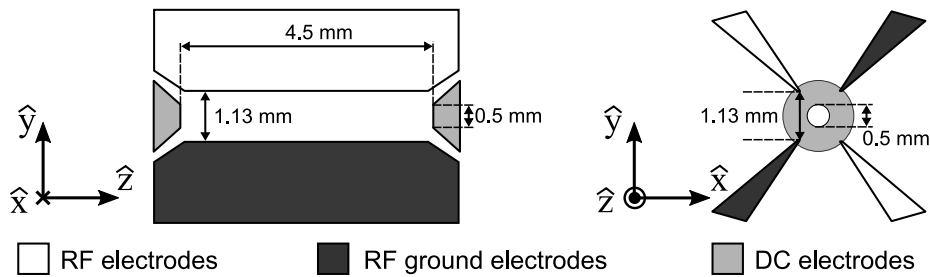


Figure 6.1. Schematic of the linear Paul trap used in the QSim experiment. The trap consists of four blade electrodes, two of which are grounded; an RF voltage is applied to the two remaining electrode blades to confine ions in the radial direction. In addition, axial confinement is generated by a DC voltage applied to two endcap electrodes, each of which has a center hole for optical access along the trap axis. Not shown in this illustration are the four electrodes for micromotion compensation.

The distance between the endcap electrodes is 4.5 mm, the distance from blade to neighboring blade is 1.131 mm, and each blade’s length is 4.02 mm. This geometry leads to a minimum expected electrode-ion distance of $565\ \mu\text{m}$ [138].

6.1. The linear-trap setup

Ions are confined in the radial plane by a quadrupole potential generated by RF voltage applied to two blade electrodes diagonally opposed to one another. The two remaining blades are held at ground (GND). The RF voltage is generated by a digital synthesizer¹ and amplified² before it is coupled to a helical resonator with a resonance frequency of 28.8 MHz. This resonator transforms the power provided by the amplifier (typically several W) to high voltages at low currents.

The axial confinement is generated by DC voltages applied to the two endcap electrodes. Each endcap is machined with a hole of 500 μm diameter in its tip, which enables optical access to the ions along the trap axis. The DC voltage source is a commercial high-voltage power supply³. The voltage passes through an RC low-pass filter (resistance of 33 k Ω , capacitance of 820 pF, resulting in a cutoff frequency of 5.9 kHz) before it reaches the endcap electrodes in order to suppress the heating of the ions due to electrical noise.

Compensation of micromotion is achieved by applying DC voltages to four additional electrodes to counteract possible stray fields. The voltages for micromotion compensation are provided by two laboratory power supplies⁴. These voltages are also filtered (resistance of 2 M Ω , capacitance of 820 pF, and cutoff frequency of 100 Hz).

The vacuum setup

The linear trap is mounted in the center of a stainless steel octagon with eight CF63 flanges (see Fig. 6.2), all of which can be used for optical access, and two CF200 flanges above and below. The trap holder is connected to the top CF200 flange.

A six-way cross mounted on the flange on the west side connects the chamber to the major part of the vacuum-maintenance system. This system consists of a Bayard-Alpert ion gauge⁵, a titanium-sublimation pump⁶ and a 20^{1/s} ion pump⁷. Furthermore, a non-evaporable getter (NEG) pump⁸ is mounted on the CF200 flange below the trap. When necessary, monitoring of the vacuum conditions is carried out using a residual gas analyzer (RGA)⁹ that is installed on a CF40 flange, welded to the top flange (CF200).

Of the eight CF63 flanges, three have inverted viewports. These viewports are recessed and pointing into the chamber to allow closer optical access to the trap. In two of the inverted viewports, objectives¹⁰ are recessed for imaging the ion's fluorescence onto a PMT and an EMCCD camera. These objectives are also used to focus light that is used to address single ions within an ion crystal.

¹Rohde & Schwarz GmbH, SML-01

²Mini-Circuits, LZY-1

³iseg Spezialelektronik GmbH, 16EHS8020x-K2

⁴EA Elektro-Automatik GmbH & Co. KG, PS 3646A and 3644A

⁵VARIAN; UHV-24p

⁶VARIAN; cartridge model 916-0050

⁷VARIAN; VacIon Plus 20 StarCell

⁸SAES; Capacitorr D100

⁹Stanford Research Systems, Inc.; RGA 100

¹⁰Silloptics GmbH

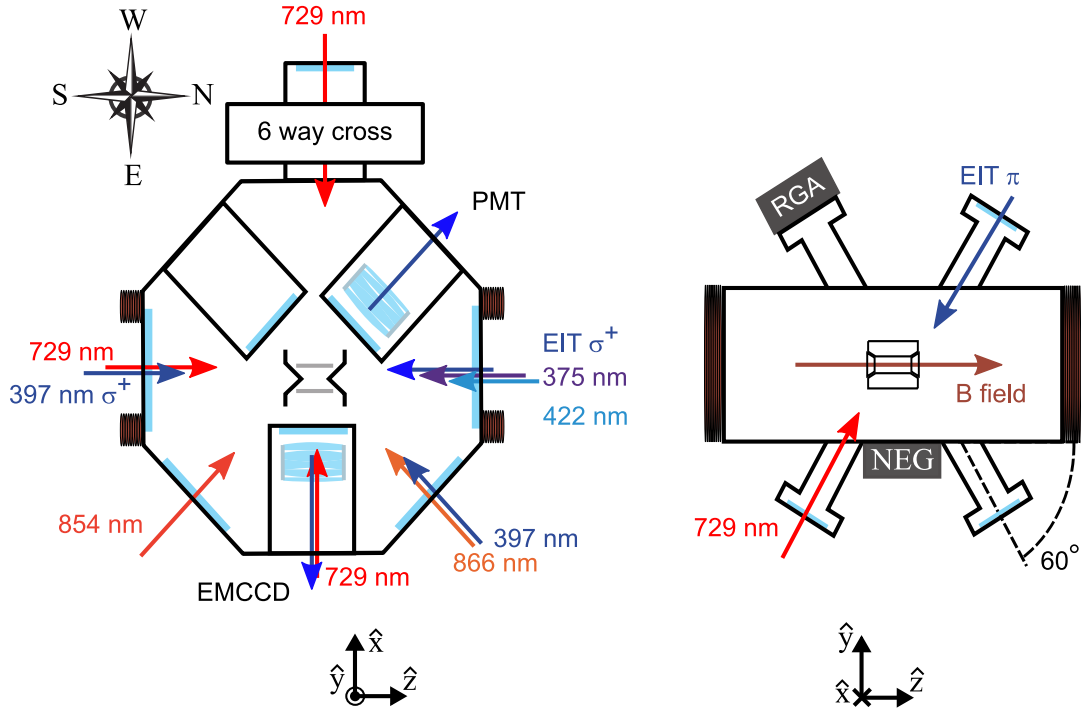


Figure 6.2. Top-view and side-view schematics of the vacuum vessel, with orientation in the physical lab frame indicated by the compass star in the left upper corner. The schematic is based on Fig. 3.6 in reference [138]. A six-way cross connects the major part of the vacuum setup to the main chamber housing the trap. In addition, a non-evaporable getter (NEG) is connected to the bottom flange and a residual gas analyzer (RGA) is connected to a flange protruding at 60° from the top. All laser sources used for the experiments described here are indicated, including the beams at 397 nm for EIT cooling. Details on their application can be found in the main text and in Ch. 4. Note that the position of incidence of the 729 nm beam is chosen with respect to the ion motion — the experiments presented in this chapter are carried out with the beam propagating from west to east, thereby coupling to the radial motional modes. The photomultiplier tube (PMT) and electron-multiplying charged-coupled device (EMCCD) camera are used to read out the electronic state of the ions. In both cases, an objective consisting of five lenses is used for magnification. Two magnetic field coils (brown) facing south and north, generate a magnetic field pointing north.

Additional optical access is provided by two CF40 flanges with an angle of 60° to the horizontal plane, welded to the top and bottom flange, respectively.

Electrical connections are implemented via the top and bottom flanges. The top CF200 flange has both a CF40 feedthrough for the RF connection to the helical resonator and a CF16 feedthrough for DC electrical connections to the endcap and compensation electrodes. The commercial calcium source¹¹ is mounted below the trap and connected electrically via a CF16 feedthrough.

In the QSim experiment, precise control of the applied magnetic field and suppression of unwanted magnetic field fluctuations play an integral role. Magnetic field fluctuations influence the transition frequency used to encode the quantum bit, thus introducing an error source to the quantum computation [37]. Hence,

¹¹Alvatec Production and Sales GesmbH; AS-2-Ca-50-C

6.1. The linear-trap setup

the vacuum apparatus is surrounded by a magnetic shield¹² that protects the trap from DC and [alternating current \(AC\)](#) magnetic-field components. The magnetic field to lift the Zeeman-sublevel degeneracy is generated with two coils mounted to the vacuum vessel (see Fig. 6.2) and driven with a proportional-integral (PI) stabilized current driver built by our electronics workshop.

6.1.2 The laser setup

Photoionization lasers at 375 nm and 422 nm

As described in Ch. 4, Sec. 4.2.1, photoionization of neutral calcium atoms is a two-step process: a first, resonant step at 422 nm excites the atom from the $4s^1S_0$ state to the $4p^1P_1$ state and a second, off-resonant step at 375 nm induces an excitation to the continuum.

In the QSim experiment, the light at 422 nm is frequency-doubled 844 nm light from a commercially available module¹³, and the 375 nm light is provided by a diode laser¹⁴. Both beams are sent through optical fibers and overlapped in front of the vacuum chamber before passing through the holes in the trap endcaps. This configuration ensures that the photoionization beams are aligned along the trap axis.

Laser driving the $S_{1/2} \Leftrightarrow P_{1/2}$ transition

As described in Ch. 4, Sec. 4.2.2, light at 397 nm is used to address the $S_{1/2} \Leftrightarrow P_{1/2}$ transition to provide Doppler cooling, state detection, state preparation, and EIT cooling.

The laser light is generated by a master-oscillator power-amplifier system¹⁵, which is a commercial frequency doubling system with TA. A part of the 794 nm light before the doubling stage is sent to a wavemeter¹⁶, and another part is sent through an [electro-optical modulator \(EOM\)](#) to an external reference cavity, which provides a stable frequency reference. Details on this resonator can be found in reference [126]. The laser is locked to the cavity via the [Pound Drever Hall \(PDH\)](#) locking scheme. After doubling, the light is split in different paths using a cascaded system of $\lambda/2$ wave plates and [polarizing beam splitter \(PBS\)](#) cubes. Acousto-optic modulators (AOMs)¹⁷ with a center frequency of 220 MHz in double-pass configuration allow on and off switching of the light in the different paths. Single-mode fibers couple the light from the laser table to the experimental table and to the setup for EIT cooling (Sec. 6.1.3).

¹²IMEDCO AG; Switzerland

¹³TOPTICA Photonics AG, TA-SHG pro

¹⁴TOPTICA Photonics AG, DL-100

¹⁵TOPTICA Photonics AG, DL-SHG pro

¹⁶HighFinesse GmbH, WSU/2

¹⁷Crystal Technology Inc., 3220-120

Laser driving the $S_{1/2} \Leftrightarrow D_{5/2}$ transition

As described in Ch. 4, Sec. 4.2.3, light at 729 nm is used to address the $S_{1/2} \Leftrightarrow D_{5/2}$ transition to enable ground-state cooling, spectroscopy, and the implementation of gate operations.

As in the Microon apparatus, light at 532 nm from a diode-pumped Nd:YV04¹⁸ is used to pump a Ti:Sa laser¹⁹, which generates light at 729 nm. A fraction of the 729 nm light is sent via an EOM to an external frequency reference, to which the laser is locked via the PDH scheme. In this way, the laser linewidth can be stabilized to within a few hertz. The frequency reference is a stable high-finesse resonator (finesse $\mathcal{F} = 407000$, linewidth $\Delta\nu = 4.75$ kHz [138]), which consists of ultra-low expansion (ULE) material. In addition, the resonator is subject to temperature stabilization and vibration isolation to suppress perturbations originating from noisy surroundings. As described in Ch. 4, Sec. 4.2.3, the long-term drift of the cavity is counteracted by comparison of the 729 nm laser frequency and the $S_{1/2} \Leftrightarrow D_{5/2}$ resonance frequency of the ion. These measures result in a long-term drift rate of 60 mHz/s. A detailed characterization of the resonator can be found in reference [138].

Most of the light is amplified by a TA²⁰ before passing through an AOM²¹ with a center frequency of 270 MHz in double-pass configuration. Additional AOMs²² with center frequencies of 80 MHz are used to switch between different beam paths that enter the chamber through different viewports (Fig. reffig:VacQ). Thus, we are able to switch between a tightly focused beam that addresses only a single ion within an ion crystal and beams that interact with all ions. Furthermore, the laser's different angles of incident enable optimization of the coupling strength between the addressed motional mode and the laser light.

Lasers driving the $D_{3/2} \Leftrightarrow P_{1/2}$ transition and the $D_{5/2} \Leftrightarrow P_{3/2}$ transition

As described in Ch. 4, Sec. 4.2.4 and Sec. 4.2.5, light at 866 nm is used to address the $D_{3/2} \Leftrightarrow P_{1/2}$ transition, and light at 854 nm is used to address the $D_{5/2} \Leftrightarrow P_{3/2}$ transition. Both infrared laser beams are used to close the transition cycle.

Both laser sources are commercially available diode lasers²³. The light generated by each laser is divided into three paths: one for an external reference cavity lock using the PDH locking scheme, a second for monitoring the wavelength on the wavemeter, and a third in which light is sent to the experiment. Details on the external frequency reference can be found in reference [126].

For the 854 nm laser, an AOM²⁴ with a center frequency of 80 MHz is used in double-pass configuration. The part of the 866 nm light sent to the experiment

¹⁸Coherent Inc., Verdi V10

¹⁹Coherent Inc., CR-899-21

²⁰TOPTICA Photonics AG, TA pro

²¹Brimrose Corporation of America, TEF-270-100

²²Crystal Technology Inc., 3080-120

²³TOPTICA Photonics AG, DL-100 and DL-pro

²⁴Crystal Technology Inc., 3080-120

6.1. The linear-trap setup

is also controlled via an AOM²⁵ with a center frequency of 80 MHz. However, due to historic reasons, the 866 nm setup makes use of the AOM in single-pass configuration.

6.1.3 The EIT-cooling setup

We plan to carry out measurements using long ion crystals (i.e., more than twenty). Thus, the application of a multi-mode cooling technique would allow us to reduce the duration of an experimental sequence. Therefore, part of the light generated by the commercial doubling system at 397 nm is used to implement the EIT cooling technique.

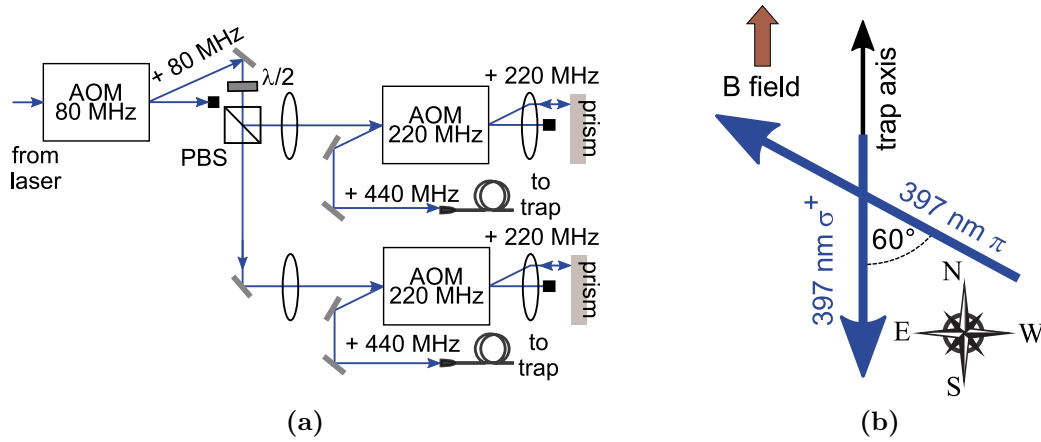


Figure 6.3. Optical setup implemented for EIT cooling and overview of the EIT cooling beam alignment. (a) The first diffraction order of an AOM with center frequency of 80 MHz is split into two paths using a PBS cube, while its zeroth order is blocked. The diffracted light is sent through two nearly identical paths: both consist of an AOM with a center frequency of 220 MHz used in double-pass configuration. The modulated light is then sent through single-mode fibers to the vacuum chamber. (b) Laser beam alignment with respect to the trap axis. The orientation in the physical lab frame is indicated by the compass star in the right lower corner. The σ^+ -polarized light is oriented anti-parallel to the magnetic field axis, while the π -polarized light forms an angle of 60° with it. The resulting Raman k vector has equal overlap with both radial modes and forms an angle of 60° with the axial direction of motion. Compare also Fig. 6.2 for a more complete overview.

While most of the light at 397 nm is used for Doppler cooling and optical pumping, about 20% of it is coupled through a single-mode fiber to the cooling setup illustrated in Fig. 6.3(a). There, the output passes through an AOM with a center frequency of 80 MHz²⁶. The +1 order is shared between two paths using a half wave plate and a PBS in order to provide both σ^+ and π -polarized beams. Each path consists of an AOM with a center frequency of 220 MHz²⁷, used in double-pass configuration. The modulated light from each path is coupled into a single-mode fiber and sent to the trap.

²⁵Crystal Technology Inc., 3080-120

²⁶Brimrose Corporation of America, QZF 80-20-395

²⁷Crystal Technology Inc., 3220-120

In the vacuum chamber, the σ^+ -polarized light passes through the tips of the trap and is thus aligned with the magnetic field. The beam waist is chosen so that the edges do not clip on the trap tips. If light was scattered on the trap tips, the trap electrodes might charge, which would alter the trap potential. The π -polarized light is sent into the chamber from one of the upper viewports at an angle of 60° to the horizontal plane (see Fig. 6.2). Its beam waist is chosen based on the target length of the ion chains it should cool, but again, it is necessary to reduce the possibility of charge built-up due to stray light. A schematic of the alignment is presented in Fig. 6.3(b).

The current beam arrangement results in a Raman k vector, $(\mathbf{k}_\pi - \mathbf{k}_\sigma)$, that forms an angle of 60° with respect to the trap axis. Hence, there is an overlap between the axial motion and the Raman k vector. In addition, there is equal overlap between the Raman k vector and both radial modes, facilitating cooling of both directions of motion with equal efficiency.

Previously executed experiments were carried out using the radial mode spectrum for gate operations [132]. Furthermore, future experiments were envisioned to incorporate up to twenty ions and more with gate operations also implemented with the transversal modes. Thus, we focused on the characterization of the EIT cooling investigation in this part of the spectrum. The equal overlap with both radial directions of motion allowed cooling of all radial motional modes with one single cooling pulse (Sec. 6.3).

However, we also observed an unwanted heating of the axial modes for potential settings that would allow trapping of such large ion strings, i.e., with an axial trap frequency of approximately $2\pi \times 200$ kHz. The heating manifested in a decreased excitation for driving Rabi oscillation with a focused 729 nm beam. Thus, the vibrational excitation of the axial motional modes was investigated with a single ion. It was not possible to measure and compare Rabi oscillations on the red sideband and blue sideband, since the ion was in such a high vibrational state. Instead, the red-sideband axial mode spectrum was investigated after Doppler cooling, and EIT cooling optimized to act on the radial mode spectrum. The observations clearly indicated an increase in temperature for the EIT cooling case, as the number of visible higher-order sidebands increased. We estimated the mean phonon number after Doppler cooling to be $\langle n \rangle_{\text{Doppler}} \approx 180$ by fitting a Gaussian to the determined spectra based on a Boltzmann velocity distribution in a thermal state. For the axial trap frequency of $2\pi \times 200$ kHz, a theoretical calculation yields $\langle n \rangle_{\text{theo}} = 54$. In addition, previous measurements of the mean phonon number at higher trap frequencies lead to an expected value ranging between $\langle n \rangle \approx 90 - 120$ for a trap frequency of $2\pi \times 200$ kHz. Thus, the observed mean phonon number is larger than the theoretical value by more than a factor of three and deviates from the empirically determined value range by at least 30%. After EIT cooling of the radial mode spectrum is applied, the vibrational excitation increases further to $\langle n \rangle_{\text{EIT}} \approx 320$.

Currently, the mechanism behind this effect is not clear. One possible explanation is that the high vibrational excitation for low axial confinement after Doppler cooling leads to a break down of the EIT theory. The initial high temperatures might result in a dissolution of the carrier suppression usually provided

6.2. Motional-state analysis

by the technique, allowing off-resonant scattering processes to heat the ion up even further.

The reported problem can be overcome by a change in the setup: for an angle of 90° between the Raman k vector and the axial direction of motion, no overlap exists and the axial motion does not couple to the cooling beams. One approach to realize this configuration is a change in the magnetic field axis. However, this would also include a change in the optical setup and decrease the coupling strength of the 729 nm with the $S_{1/2} \Leftrightarrow D_{5/2}$ transitions. At the moment, there are no plans of rebuilding the setup, since all experiments envisioned in the near future can be carried out with sideband cooling as a ground-state cooling technique. However, a change-over may become necessary when the number of ions involved in computations and simulations increase beyond the current number of twenty.

6.2 Motional-state analysis

In order to assess the performance of a cooling technique, a measurement of the vibrational state of the ions' motional mode is necessary. While for a single trapped ion a comparison of the excitation on the red-sideband transition and the blue-sideband transition is sufficient, the situation gets more complicated for a trapped ion crystal due to the ions' mutual Coulomb repulsion. Hence, different approaches to determine the mean phonon number are necessary. Details on theoretical considerations concerning these measurements can be found in Ch. 3.

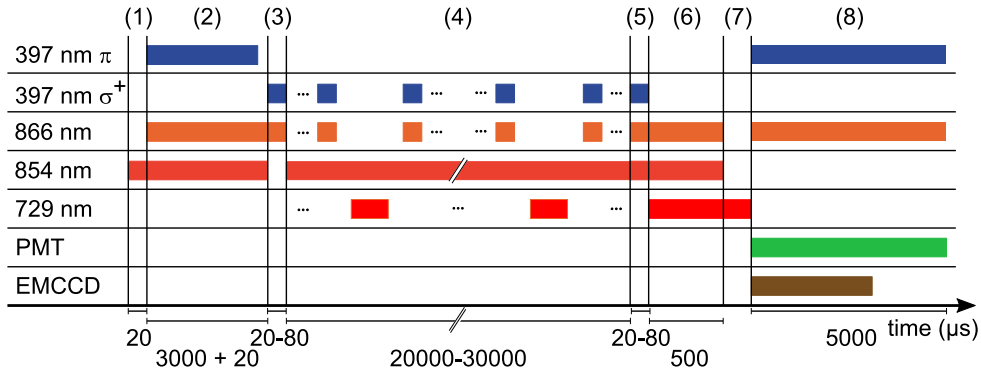


Figure 6.4. Experimental sequence for the QSim experiment. (1) Each sequence starts with a repumping step, ensuring the ion no longer populates the long-lived $D_{5/2}$ state. (2) Subsequently, the ion is Doppler cooled. The closing of the cooling cycle is ensured by applying the infrared lasers at 866 nm and 854 nm for an additional 20 μs . (3) Thereafter, population is accumulated in one of the ground states by optical pumping using a resonant σ^+ -polarized beam. The cycle is again closed with the 866 nm laser. (4) For the experiments in this section, sideband cooling is the ground-state cooling technique used. The length varies depending on the number of modes cooled. In addition, the sideband cooling step consists of several repetitions alternating between optical pumping and cooling of the modes. Two additional steps ensure proper state initialization of the ion: (5) optical pumping using the resonant σ^+ beam, and (6) optical pumping using the 729 nm laser. (7) After these initial steps, the quadrupole laser is applied to manipulate the qubit state. Note that it is this step that changes depending on the applied motional state analysis. (8) The electronic state of the ion is read out with the PMT and the camera using the electron-shelving method.

During the work for this thesis, we implemented various techniques to determine the mean phonon number for a motional mode. For a single trapped ion, the excitations on the red sideband and blue sideband were compared. For a multi-ion crystal, a *global* blue-sideband Rabi oscillation was recorded and compared to the theoretical expectations. In this context, *global* refers to the fact that all ions are illuminated by the laser simultaneously. Another fast and robust measurement method that was implemented is [RAP](#). The measurements presented here have been executed based on the sequence illustrated in Fig. 6.4. Note that step (7) in the presented sequence differs, depending on the executed experiment. The techniques and the obtained results are discussed below.

6.2.1 Single-ion heating rate

The method of comparing the excitations on the red sideband and blue sideband was implemented to extract the heating rate of the radial [COM](#) modes of an ion with trap frequencies $\{\omega_x, \omega_y, \omega_z\} = 2\pi \times \{2.74, 2.61, 0.5\}$ MHz.

As depicted in Fig. 6.4, the ion was prepared in its electronic and vibrational ground state for one of the radial COM modes by applying Doppler cooling, optical pumping and sideband cooling on that mode. These experimental steps were followed by a varying waiting time (from 0 ms up to 100 ms). Subsequently, excitation on the red sideband or blue sideband of the $|S_{1/2}, m = 1/2\rangle \leftrightarrow |D_{5/2}, m = 5/2\rangle$ transition was executed ($2\pi \times 2.74$ MHz and $2\pi \times 2.61$ MHz, respectively). The excitation time was set to implement a π pulse on the blue sideband for an ion prepared in the motional ground state ($n = 0$). The Rabi frequencies were $\Omega_{01} = 2\pi \times 1.5$ kHz for the mode at $2\pi \times 2.74$ MHz and $\Omega_{01} = 2\pi \times 1.8$ kHz for the mode at $2\pi \times 2.61$ MHz.

The observed heating rates for both radial COM modes are illustrated in Fig. 6.5. Both show a linear increase with increasing waiting time. This behavior corresponds to the theoretical predictions, which relate a fixed rate to the interaction between the trapped ion and its noisy environment. A linear regression model fit to the data determines the heating rates to be 5.9(3) phonons/s for the mode at $2\pi \times 2.74$ MHz [[data14d](#)] and 4.6(2) phonons/s for the mode at $2\pi \times 2.61$ MHz [[data14e](#)].

Direct comparison of previously published heating rates is not directly possible, since the value of 21(1) phonons/s was determined at an axial motional frequency of $2\pi \times 1.23$ MHz. However, the extracted values match the known behavior of low heating rates for macroscopic traps. This fact is punctuated by a comparison of the macroscopic trap's heating rates with the ones obtained for the [Mireon](#) trap (Ch 5, Fig 5.4): although the radial trapping frequencies are more than 1.5 times higher in the [Mireon](#) trap than in the macroscopic linear trap, the heating rates for the smaller trap are several orders of magnitude larger. This deviation can probably be attributed to the difference in the electrode-ion distance in both traps, which is 2.1 times larger in the macroscopic linear trap.

6.2. Motional-state analysis

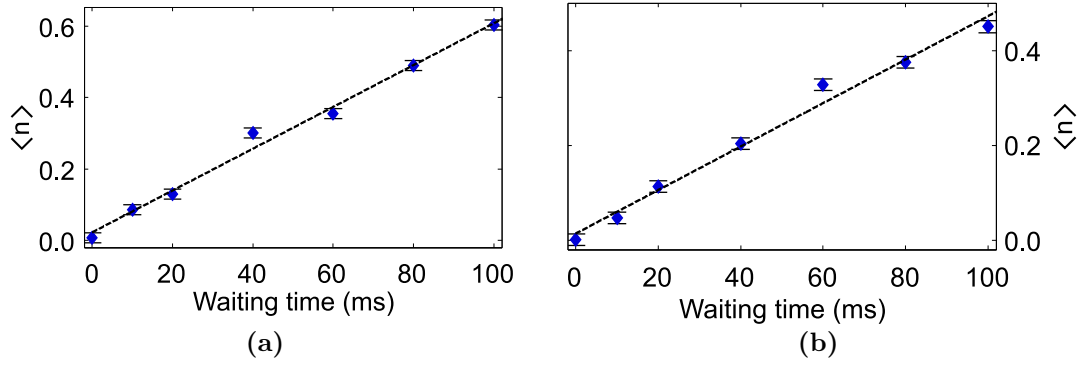


Figure 6.5. Heating-rate measurement for a single trapped ion on both radial COM modes. The measurement was executed by comparing the excitations on the red-sideband and blue-sideband transitions after sideband cooling. The error bars are derived from projection noise. (a) A linear regression model fitted to the data [data14d] (dashed line) yields a heating rate of 5.9(3) phonons/s on the radial COM mode at $2\pi \times 2.74$ MHz. (b) A linear regression model fitted to the data [data14e] (dashed line) yields a heating rate of 4.6(2) phonons/s on the radial COM mode at $2\pi \times 2.61$ MHz.

6.2.2 Dynamics of the blue-sideband transition

One method to determine the vibrational state of an ion chain is by blue-sideband pulse-length scans on all ions simultaneously. The data from these measurements allow the extraction of the Fock state populations, which can be compared to numerical simulations, as discussed in Ch. 3. We implemented this technique using a four-ion crystal with trap frequencies $\{\omega_x, \omega_y, \omega_z\}_{\text{com}} = 2\pi \times \{2.71, 2.64, 0.50\}$ MHz.

As for the single-ion measurement, and as depicted in Fig. 6.4, the ion crystal was prepared in the electronic ground state and the vibrational ground state by applying Doppler cooling, optical pumping and sideband cooling. However, due to an oversight, sideband cooling was not optimized for the higher COM mode at $2\pi \times 2.71$ MHz used for the measurement but set to $2\pi \times 2.67$ MHz, cooling both radial COM modes inefficiently. After cooling and state initialization, all ions were subject to a pulse-length scan on the blue-sideband transition of the COM mode at $2\pi \times 2.71$ MHz. The $|S_{1/2}, m = 1/2\rangle \leftrightarrow |D_{5/2}, m = 5/2\rangle$ transition was used for this measurement, due to the strong coupling between the 729 nm laser and this transition based on the experimental geometry. The Rabi frequency on the carrier transition was $\Omega = 2\pi \times 100$ kHz and the Lamb-Dicke factor for the radial COM mode was $\eta = 0.0209$.

Fig. 6.6 shows the measured population oscillations, averaging over three measurements [data14f]. The error bars represent projection noise. The depicted traces illustrate the excitation probabilities for the following cases: all ion dark $|0000\rangle$, all but one ions dark $|1000\rangle$, two ions dark and two ions bright $|1100\rangle$, all but one ions bright $|1110\rangle$, and all ions bright $|1111\rangle$.

Generally, laser cooling can be described as a dissipative process that couples the trapped ion to a thermal environment. One common representation of this situation is based on a thermal distribution of the phonon number in the system. Based on this considerations, the experimental data are compared to a thermal

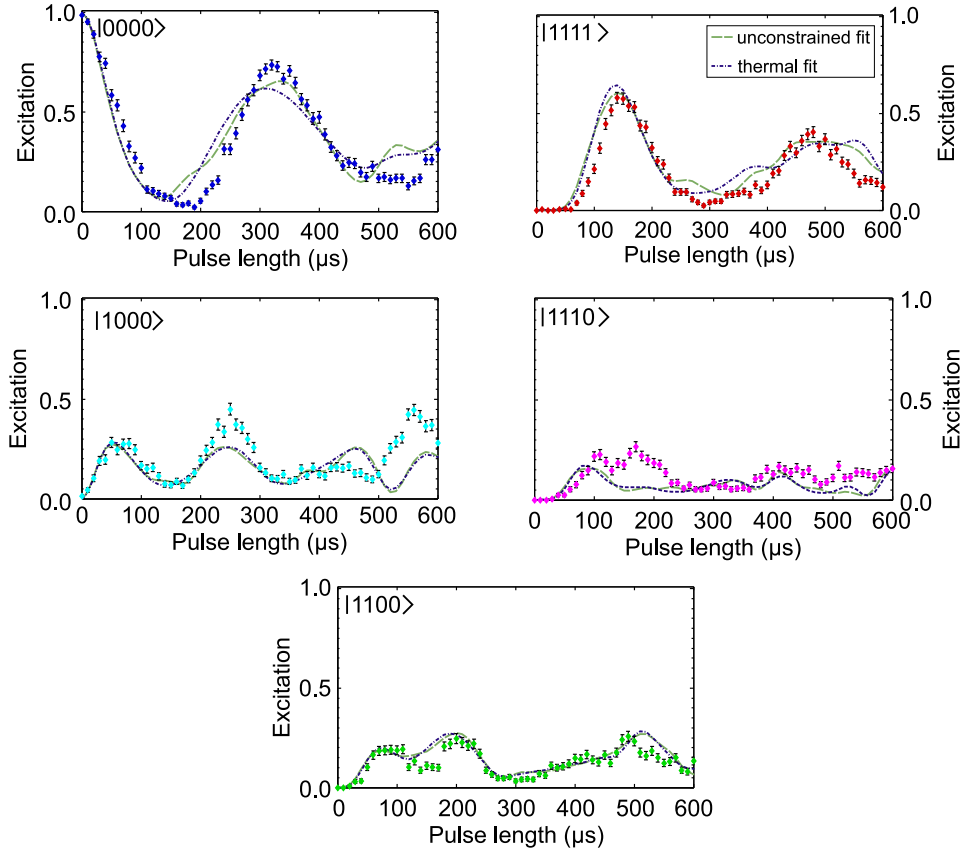


Figure 6.6. Global blue-sideband pulse-length scan of a four-ion crystal, driven on the COM mode at $2\pi \times 2.71$ MHz [data14f]. Error bars correspond to projection noise. The five different traces correspond to five possible cases of electronic excitation, indicated by $|0000\rangle$ for all ions are dark, $|1111\rangle$ for all ions bright, and every possible configuration in between these two cases. Fitting routines assuming a thermal phonon distribution are represented by the blue dashed-dotted lines. In addition, an unconstrained fit has been introduced and is represented by the black dashed line. The fitting routines allow us to determine the phonon population distribution from the measurement data (see Fig. 6.7). They take into account a carrier Rabi frequency of $\Omega = 2\pi \times 100$ kHz and a Lamb-Dicke factor of $\eta = 0.0209$.

distribution fit. In addition, an unconstrained model fit was used in order to test the reliability of our assumption. The experimental data are compared to calculations based on both theories, incorporating solutions of the Schrödinger equation taking into account initial phonon excitation up to $n = 5$. As indicated by the legend, the blue dashed-dotted lines correspond to a thermal distribution of phonon states and the black dashed lines are the result of an unconstrained fit.

The extracted phonon number distributions, as presented in Fig. 6.7, are derived by applying the fit models simultaneously to the data for all five different cases of electronic excitation, depicted in Fig. 6.6. The extracted mean phonon numbers are $\langle n \rangle = 1.0(3)$ for the unconstrained fit, and $\langle n \rangle = 0.9(1)$ for the thermal distribution fit. The **root-mean-square error (RMSE)** is a measure of the deviation from the values predicted by the models and the measurement data. The unconstrained fit has an RMSE value of 0.0825, and the thermal fit has an RMSE value of 0.0858. Thus, the unconstrained model fit achieves a better over-

6.2. Motional-state analysis

lap between theoretical calculations and the measurement data, but there is only 4% difference between the two fits.

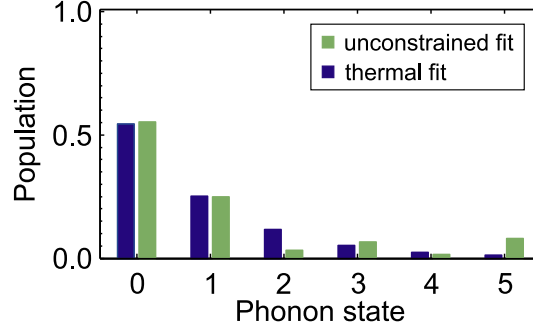


Figure 6.7. Phonon-state distribution for a global blue-sideband pulse-length scan of a four-ion crystal. The distributions are derived from the fits shown in Fig. 6.6. Note that the models are fitted to all five subplots in Fig. 6.6 simultaneously. For the ground state and first excited state, the derived populations are similar regardless of the fitting routine applied. However, the thermal distribution fit shows a continuous decrease of population with higher phonon number, which is not the case for the unconstrained fit.

We are confident to state that the mean phonon number is $\langle n \rangle = 0.9(1)$, derived from the thermal distribution fit. This decision is based on the fact, that the ions were sideband cooled and the extracted mean phonon numbers for both fitting models correspond within the error margin. The deviations between the thermal distribution fit curve and the PMT data, specifically for the cases of only one ion excited $|1000\rangle$ (for pulse lengths between $200\ \mu\text{s}$ and $300\ \mu\text{s}$ and between $500\ \mu\text{s}$ and $600\ \mu\text{s}$) and all but one ion excited $|1110\rangle$ (for pulse lengths between $100\ \mu\text{s}$ and $200\ \mu\text{s}$), could not be accounted for. The preliminary assumption that these deviations were based on a bad setting of the PMT thresholds, which discriminate the different cases, could be ruled out by thorough data analysis. However, future application of this technique to determine the mean phonon number, especially for larger ion crystals, could be based on the EMCCD camera. Thereby, the fit model might show more overlap with the data, thus reducing the RMSE value.

The presented measurement of global blue-sideband Rabi oscillations represents one method to extract the mean phonon number of a motional mode in a multi-ion crystal. However, the investigation also showed that the method has some drawbacks, as it relies on the precise knowledge of the initial Rabi frequency and can only be applied in an indirect fashion. Thus, we implemented another method to determine the vibrational state of a motional mode. RAP represents a technique that allows a more direct readout of the vibrational excitation. Nonetheless, global excitations of the blue sideband can be an effective way to determine the mean phonon number, specifically if high heating rates of the system prevent the application of RAP, which takes up several ms within an experimental sequence.

6.2.3 RAP to determine the mean phonon number

RAP can be applied to create Fock states as well as to determine the mean phonon number for a motional mode of an ion crystal, as presented theoretically in Ch. 3. In the QSim trap, we implemented both techniques. The possibility to map the vibrational state of an ion string onto electronic excitations using a chirped, intensity-shaped laser pulse is a very useful, versatile and robust technique, as is shown in the following measurements.

The presented measurements again follow the sequence depicted in Fig. 6.4. Depending on the task at hand, RAP is implemented either to read out the ion chain's vibrational state or to create a Fock state. The control electronics of the QSim experiment are able to generate intensity-shaped pulses²⁸, for example, in Blackman shape (Ch. 3, Eq. 3.43), combined with a linear frequency sweep, as required for the RAP experiments.

6.2.3.1 RAP to measure Fock states

In order to test the principal functionality of the RAP sequence, we prepared Fock states of a nine-ion crystal with trap frequencies $\{\omega_x, \omega_y, \omega_z\}_{\text{com}} = 2\pi \times \{2.76, 2.59, 0.5\}$ MHz using addressed pulses on the blue-sideband transition. Then, the generated number state was read out by applying the RAP method.

RAP was applied to a radial mode at $2\pi \times 2.25$ MHz. This mode was selected due to its good spectral separation (approximately 70 kHz to the nearest higher and lower modes). Furthermore, the expected heating rate for the mode was lower than for the radial COM modes [139, 140], enabling the slow frequency sweep necessary to accomplish RAP²⁹. The ion excursion from equilibrium for this mode is largest for the second and eighth ion. Hence, an addressed laser pulse should focus on either of the two ions to result in a high coupling strength.

Preparation of the ion crystal in the electronic and vibrational ground state was executed, using Doppler cooling, optical pumping and sideband cooling of both the $2\pi \times 2.25$ MHz mode and two lower neighboring modes by choosing a frequency of $2\pi \times 2.13$ MHz. In multi-ion crystals, the coupling strength of the mode applied for quantum bit manipulation is altered due to the vibrational excitation of neighboring modes. Thus, cooling of these modes is beneficial as is shown, for example, by a decreased damping of the Rabi oscillation contrast (see reference [37], Fig. 15). Therefore, we chose the given mode frequencies for cooling. The higher neighboring mode at $2\pi \times 2.32$ MHz was not included in the sideband cooling scheme in the presented measurements. However, an additional sideband cooling pulse at this frequency could improve the reported ground-state population of 97(3) %.

The initialization was followed by the preparation of the ion crystal in a Fock state, using consecutive addressed π pulses on the $|S_{1/2}, m = 1/2\rangle \leftrightarrow |D_{5/2}, m =$

²⁸Details on the pulse sequencer used can be found in P. Schindler's master's thesis [115].

²⁹The pulse duration to achieve RAP given the QSim experimental parameters is approximately 5 ms. However, during this time, the COM mode's vibrational excitation increases by about 0.3 phonons for a nine-ion crystal. This is due to the fact that the heating rate scales proportional to the number of ions in the crystal.

6.2. Motional-state analysis

$5/2\rangle$ transition with a focused beam coupling to the second ion. An addressed π pulse on the blue sideband for the second ion prepared in the motional ground state ($n=0$) had a pulse duration of 123 μs . This value corresponded to a Rabi frequency of $\Omega_{0,1} = 2\pi \times 8.1\text{ kHz}$, which was extracted from a fit to Rabi oscillations measured under the described conditions. After each preparation step, a pulse at 854 nm was implemented to return the population to the electronic ground state for the following RAP, as illustrated for the single addressed ion in Fig. 6.8.

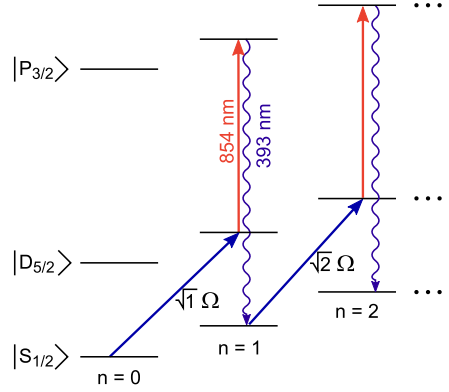


Figure 6.8. The preparation of the ion crystal in a Fock state is based on an addressed pulse on a single ion, which excites the blue-sideband transition to increase the mean phonon number, followed by a pulse on the $D_{5/2} \Leftrightarrow P_{3/2}$ transition using the 854 nm laser to pump the population back to the electronic ground state. The blue-sideband pulse acts on a single ion only and the consecutive infrared pulse is applied globally. However, the illustration only takes into account the single ion.

After the ion chain was prepared in the Fock state, [rapid adiabatic passage](#) was implemented to determine the vibrational excitation of the chain and thereby infer the prepared number state. This measurement was carried out on the red-sideband transition of the mode at $2\pi \times 2.25\text{ MHz}$ with the RAP pulse applied on all ions simultaneously. Optimization of the RAP parameters resulted in a pulse duration of 5 ms, during which the laser frequency was swept over a range of 50 kHz across the red-sideband transition. At the end of the sequence, the electronic state of the ions was detected with the EMCCD camera. The number of excited ions was identified with the numbers of phonons prior to the RAP pulse. The resulting phonon distributions are shown in Fig. 6.9 [\[data14g\]](#).

The results presented in Fig. 6.9 [\[data14g\]](#) show the histograms that correspond to the phonon number distribution for different Fock states ($n = 0$ to $n = 9$). The measured population of 97(3) % for the ground state $n = 0$ directly after sideband cooling indicates imperfect ground-state cooling. The population of the target state decreases with respect to the population found for lower number states, previously prepared and measured. $n = 2$ is an exception for this, as the population in this case is lower than for the higher number states up to $n = 5$. At the highest Fock state that can be read out using a nine-ion crystal, $n = 9$, only 53(3) % of the population has accumulated in this state, while the rest of the population is distributed across lower number states. In general, the prepared Fock state can be reconstructed with a probability $> 50\%$.

If the preparation process and the RAP measurement process were perfect,

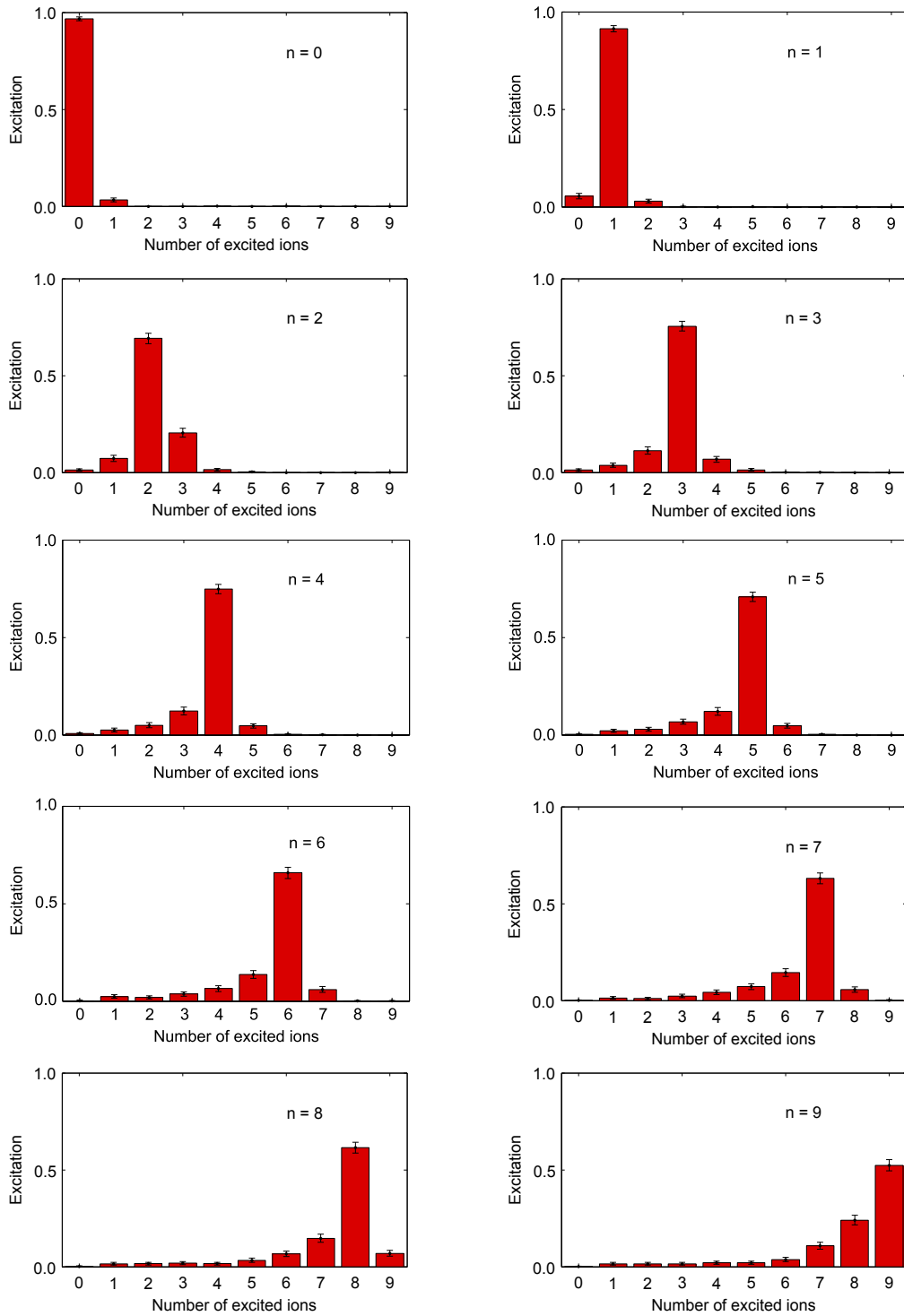


Figure 6.9. Fock-state measurement using RAP [data14g]. A nine-ion crystal was prepared in a Fock state using addressed blue-sideband excitation. Thereafter, RAP was applied to map the number state that the mode was in onto the electronic excitation of the ions in the chain. The histograms present the probability for a given number of ions to be excited, ranging from zero ions to nine ions. Error bars are derived from a Monte-Carlo simulation, in which the projection noise is varied. However, these error bars are a lower estimate as they do not take into account additional error sources. These additional errors include addressing errors for the state preparation and decay into levels that are not participating in the RAP process.

6.2. Motional-state analysis

a sharply defined phonon-number distribution with 100% population residing in the target phonon number would be observed. However, experimental imperfections lead to a deviation from this ideal outcome. There are two possible sources for the broadening of the observed distribution: either the Fock-state preparation is imperfect or the reconstruction of the prepared state using the RAP method is erroneous. Hence, we conducted an additional experiment to determine the reliability of the state preparation method. Red-sideband transitions were driven after number state preparation, and Rabi oscillations were measured.

Measuring the phonon distribution with Rabi oscillations

In the Lamb-Dicke regime, three kinds of transitions have to be considered: transitions on the carrier, which do not change the phonon number; transitions on a blue sideband, which increase the phonon number by one; and transitions on a red sideband, which decrease the phonon number by one (see Ch. 3). The coupling on the carrier transition is, to first order, independent of the phonon number, but the sideband-transition rate is directly dependent on the vibrational state of the mode.

The red sideband coupling strength, $\Omega_{n,n-1}$, increases with the phonon number, n , as (Ch. 3, Eq. 3.14)

$$\Omega_{n,n-1} = \eta\sqrt{n}\Omega,$$

in proportion with the carrier Rabi frequency, Ω , and the Lamb-Dicke factor η . For a Fock state of $n = 0$, there is no red-sideband coupling, and a pulse-length scan of the red-sideband excitation shows zero signal. However, for Fock states with $n > 0$, the connection between the Rabi frequency, $\Omega_{n,n-1}$ and the phonon number n can be employed to determine the phonon number.

In particular, a pulse-length scan on the red-sideband excitation allows the experimental determination of the phonon number for a selected mode. From a fit to the observed Rabi oscillations, the number state can be extracted if Ω and η are known. This relation was exploited to investigate specifically prepared Fock states, in order to estimate the influence of possible state-preparation imperfections on the results for applying the RAP process.

The experiments were carried out using a nine-ion crystal exhibiting trap frequencies $\{\omega_x, \omega_y, \omega_z\} = 2\pi \times \{2.76, 2.59, 0.5\}$ MHz. As for testing RAP, the ion crystal was prepared in the electronic and vibrational ground state by applying Doppler cooling, optical pumping, and sideband cooling of the modes at $2\pi \times 2.25$ MHz and $2\pi \times 2.13$ MHz. The Fock-state preparation was executed in the same fashion as previously described: an addressed blue-sideband pulse with a pulse duration corresponding to a π pulse was applied to the second ion in the chain, exciting the mode at $2\pi \times 2.25$ MHz. After the preparation step, an addressed pulse applied to the second ion on the red sideband of the mode at $2\pi \times 2.25$ MHz, and the electronic state of the ions was detected. The whole sequence was repeated for varying durations of the addressed red-sideband pulse to observe Rabi oscillations for the prepared number state $|n\rangle$.

Fig. 6.10 shows results [data14h] for experiments aiming to prepare and measure Fock states with $n = 3$ to $n = 10$. In contrast to the RAP method, the mea-

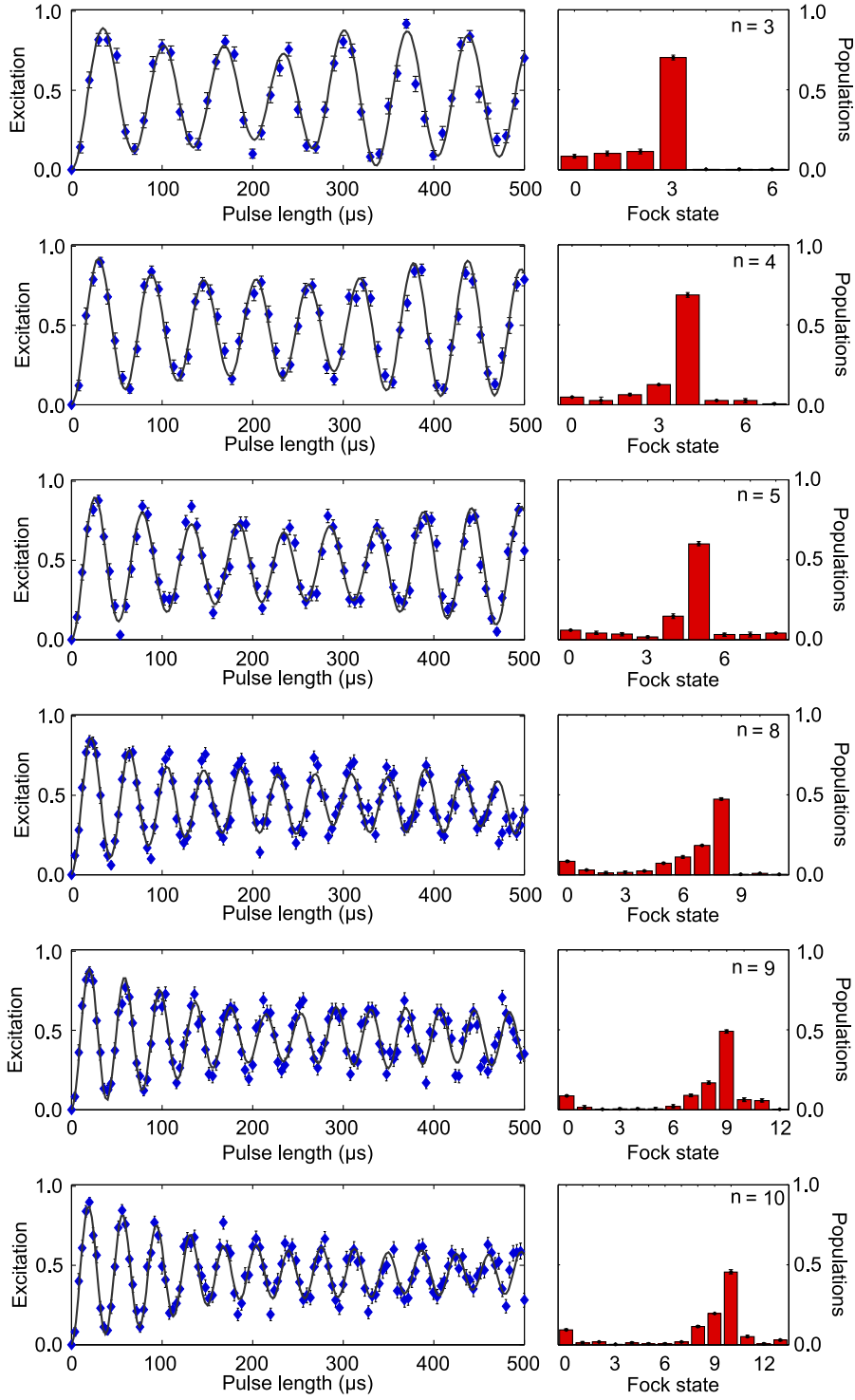


Figure 6.10. Fock-state measurement with red-sideband Rabi oscillations for a nine-ion crystal [data14h]. The Fock states were prepared using an addressed blue-sideband pulse on the second ion, employing the mode at $2\pi \times 2.25$ MHz. The Rabi oscillation frequency used for the fit is $\Omega_{1,0} = 2\pi \times 8.6$ kHz. Error bars are calculated from projection noise and Monte-Carlo simulations. They represent a lower limit as they do not include systematic and other error sources such as imperfections in the state preparations.

6.2. Motional-state analysis

surement using Rabi oscillations is not limited in the number of commensurable phonons by the number of ions forming the crystal. On the left side of Fig. 6.10, the data are presented with a fit obtained using a convex optimization routine and a Rabi frequency of $\Omega_{1,0} = 2\pi \times 8.6$ kHz. This frequency corresponds to the blue-sideband Rabi frequency for the addressed pulse on the second ion cooled to the ground state ($\Omega_{0,1}$). The right hand side presents the extracted phonon-number distribution. As for the phonon number distributions determined with RAP, the extracted population declines for higher target number states.

The results show the expected oscillatory behavior: the population of higher phonon states leads to faster oscillation frequencies. A spread of the extracted phonon-number distributions is visible, which for the perfect state-preparation and phonon state read out should not be the case. This behavior is related to a damping³⁰ of the Rabi oscillations, which leads to a reconstruction of the beat signal from a broader range of base frequencies. However, the prepared Fock number state always exhibits the highest population, allowing an unambiguous identification.

Comparison of the measurement methods

The phonon-number distributions measured using Rabi oscillations exhibit similar features as those observed for the RAP technique. The Fock-state populations derived with this method are slightly lower than for the RAP scheme, yielding, for example, a population of 50(1) % for the state $n = 9$. A larger deviation of about 10 % between the two methods can be found for the states $n = 5$ and $n = 8$. The phonon-number distributions observed with the Rabi oscillation method are also broader and take into account higher populations of the ground state.

Comparing the two phonon-number distributions, it can be inferred that the limiting factor in the RAP experiment was the method of Fock state preparation. Both reconstruction methods gave similar phonon state distributions, yielding the highest population for the prepared Fock state and concentrating the non-zero populations around this state. However, the preparation method accumulated errors with each additional step to prepare higher Fock states. This behavior can be observed regardless of the method to determine the number state.

The technique based on Rabi oscillations on the red-sideband transition has the disadvantage of heavily relying on fitting models. Also, with increasing Fock-number state the reliability of the method deteriorates: the higher the Fock-number state is, the less distinguishable the Rabi oscillation frequencies are.

[Rapid adiabatic passage](#) provides a single-shot measurement of the phonon-number distribution. Although the size of the ion crystal limits the number of commensurable phonons, RAP is a useful tool to determine the phonon-number distribution and thus mean phonon number for multi-ion crystals. In addition, the method is very versatile. We demonstrate this by using RAP on the blue-sideband transition to prepare large Fock states.

³⁰Note that this damping is inherent of the process, i.e., the damping is based on ordinary dephasing from different oscillation frequencies, and does not rely on external factors such as laser phase fluctuations.

6.2.3.2 RAP to prepare large Fock states

We demonstrate the preparation of large Fock states using RAP on the blue-sideband transition. Again, a nine-ion crystal with trap frequencies $\{\omega_x, \omega_y, \omega_z\} = 2\pi \times \{2.76, 2.59, 0.5\}$ MHz was used. The ions were initialized in the electronic and vibrational ground state by Doppler cooling, optical pumping and sideband cooling. Since the RAP process used the mode at $2\pi \times 2.25$ MHz, this mode and two lower neighboring modes ($2\pi \times 2.13$ MHz) were sideband-cooled to the ground state.

Subsequent to the initialization, [rapid adiabatic passage](#) on the blue-sideband of the $|S_{1/2}, m = 1/2\rangle \Leftrightarrow |D_{5/2}, m = 5/2\rangle$ transition was implemented for all ions. As a result of the interaction, as described in Ch. 3, the system evolved to a symmetric product state with all ions excited and as many phonons added as there are ions in the crystal³¹.

Consecutive application of the RAP process on the blue sideband results in ever higher Fock states; the Fock-state number increases by the number of ions within the chain each time RAP is applied. However, in between each application of RAP, it is necessary to pump all population to the electronic ground state by applying a carrier excitation followed by application of the infrared lasers at 854 nm and 866 nm. The carrier excitation ensures that the system is reinitialized from a dark state for the RAP process to a state, from which a blue-sideband excitation can be driven.

Since readout using RAP cannot be used to extract phonon numbers larger than the number of ions in the crystal, a different method to determine the Fock state was applied. With increasing mean phonon number n , the Rabi oscillation frequency on the blue sideband $\Omega_{n,n+1}$ increases as (Ch. 3, Eq. 3.16)

$$\Omega_{n,n+1} = \eta\sqrt{n+1}\Omega,$$

with η the Lamb-Dicke factor and Ω the carrier Rabi frequency. Hence, a pulse-length scan addressed to the second ion on the blue sideband of the mode at $2\pi \times 2.25$ MHz was applied to determine the corresponding Rabi oscillations. From the increasing Rabi oscillation frequency it was possible to determine the Fock state distribution generated using a fit based on convex optimization.

On the left side of Fig. 6.11, Rabi oscillations are plotted for three prepared number states [data14i]. As expected, we see that as the phonon number n increases, the Rabi frequency increases. The determination of the population distribution as presented on the right side relies on a fit based on a convex optimization assuming a blue-sideband Rabi frequency of $\Omega_{01} = 2\pi \times 7.4$ kHz.

The first measurement of Fig. 6.11, in which the population distribution of $n = 0$ is determined, reveals imperfect ground-state cooling as only 93(1) % of the population resides in this state. This can be attributed to uncooled modes at higher frequencies and insufficient cooling of modes at lower frequencies. With increasing number state, the fitting routine reliably extracts the population distribution. However, since the Rabi frequency is proportional to $\sqrt{n+1}$, frequencies

³¹After one application of RAP on the blue-sideband transition, the state is $|111111111, n = 9\rangle$.

6.2. Motional-state analysis

corresponding to neighboring Fock states become more difficult to distinguish. For the state $n = 18$, taking into account twenty-three number states, our evaluation shows a population of 43(4) % in the target state and 36(5) % accumulated in the state $n = 17$. The situation deteriorates for the preparation of the $n = 27$ state, for which in total thirty-two states are considered. Here, the expected state shows a population of 40(22) % and the neighboring lower state of $n = 26$ is populated with 19(23) %.

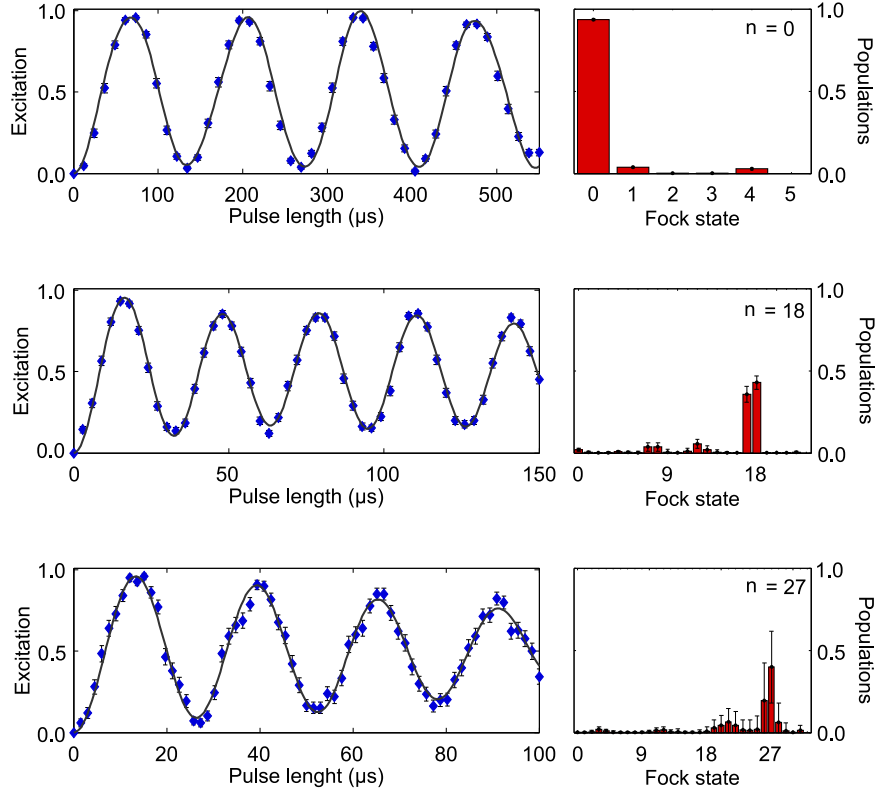


Figure 6.11. Preparation of large Fock states using blue-sideband RAP [data14i]. Rabi oscillations, depicted on the left side, allow the determination of the population distribution. The extracted distributions are presented on the right side and are determined based on a convex optimization routine using a Rabi frequency of $\Omega_{01} = 2\pi \times 7.4$ kHz. Errors in the Rabi oscillation data are attributed to projection noise. Error bars on the histograms are determined from the fitting routine and a Monte-Carlo simulation. The additional population of lower Fock number-states for $n = 18$ and $n = 27$ is due to an incomplete population transfer with the RAP process. However, the seemingly periodic occurrence of these populations has so far only been observed for the presented data and is not yet fully understood.

The indicated error bars provide a measure for the increasing difficulty in distinguishing the Fock number state. One approach to resolve the number state more clearly would be a longer measurement time, as data points for later times could be used to determine the frequency more precisely.

The state preparation of large Fock-number states by RAP is robust against fluctuations in laser intensity or detuning. One additional advantage, as compared to the state preparation method via sideband excitation introduced in Sec. 6.2.3.1, is that a single application of RAP directly generates a Fock number state that

is equal to the number of the ions in the chain. However, the duration of a single RAP step typically takes up 5 ms for experimental parameters in the QSim apparatus. Thus, data acquisition consisting of state preparation using one or several RAP pulses and subsequent excitation of the blue-sideband to determine the prepared Fock state can be tedious. In spite of the described difficulties in quantifying the phonon number, repeated RAP on the blue-sideband transition has proven to be a fast and robust technique to generate large Fock states as compared to, for example, addressed pulses on a blue-sideband transition.

6.2.3.3 RAP to determine heating rates

We carried out a heating-rate measurement on a multi-ion crystal, by applying [rapid adiabatic passage](#). For varying waiting times between the ground-state cooling technique applied and the [rapid adiabatic passage](#) process, the mean phonon number was determined. A nine-ion crystal with trap frequencies $\{\omega_x, \omega_y, \omega_z\} = 2\pi\{2.74, 2.69, 0.57\}$ MHz was used to measure the heating rate on the radial COM mode at $2\pi \times 2.74$ MHz. Results of the measurement are shown in Fig. 6.12 [[data14j](#)].

The ion crystal was prepared in its electronic and vibrational ground state by applying Doppler cooling, optical pumping and sideband cooling of the three highest radial modes (see Fig. 6.4). In this way, heating of the mode used in the measurement due to coupling to the neighboring modes is suppressed. Subsequently, a variable waiting time was included before RAP was implemented on the red-sideband of the radial COM mode of the $|S_{1/2}, m = 1/2\rangle \leftrightarrow |D_{5/2}, m = 5/2\rangle$ transition. The mapping of the vibrational excitation onto the electronic state was set up as a pulse with duration of 4 ms and a frequency sweep range of 38 kHz across the resonant sideband transition. The EMCCD camera was used to collect atomic fluorescence, from which the phonon number distributions were extracted (Fig. 6.12 inset). A thermal distribution fit to the phonon-number distribution gave the mean phonon number. The error for the data points was derived from the covariance matrix of the fitting routine.

The insets of Fig. 6.12 present two single-shot phonon-number-distribution measurements taken with the RAP method. They confirm that the phonon-number-distribution is indeed thermal, as expected for a ground-state cooled mode that is coupled to a (high-temperature) reservoir.

Fig. 6.12 shows a linear increase of the mean phonon number with the waiting time. A linear fit to the extracted mean phonon numbers yields a heating rate of 65(7) phonons/s, which is a tenfold increase compared to the single-ion heating rate (Sec. 6.2.1). The observed scaling with the ion number shows the expected behavior for the COM mode. The behavior is attributed to a near-perfect correlation for the electric field noise acting on different ions as the inter-ion distances are much smaller than the distance to the nearest trap electrode.

In theory, heating occurs only on the COM mode [[139](#), [140](#)]. Surprisingly, also higher-order radial (transverse) modes exhibited a non-zero heating rate, which was found to increase for shorter-wavelength modes. The origin of this effect is currently unclear. Mode cross-coupling to axial (longitudinal) motional modes,

6.3. EIT cooling of a multi-ion crystal

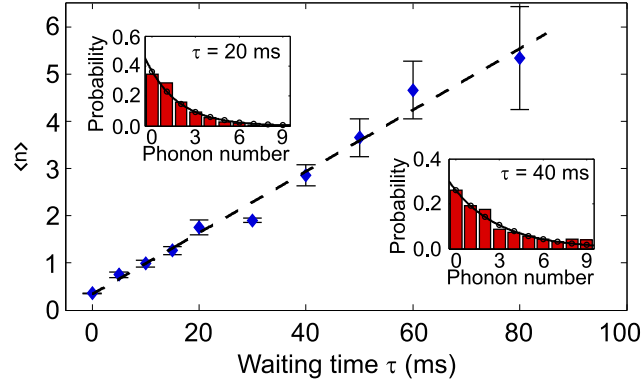


Figure 6.12. Heating-rate measurement with RAP for a nine-ion crystal [data14j]. Rapid adiabatic passage was implemented on the COM mode at $2\pi \times 2.74$ MHz. The data are compiled as histograms of how many ions are bright or dark, from which the phonon number distribution is determined. A thermal distribution fit allows us to extract the mean phonon number (solid black line, inset). Measurements were taken for varying waiting times to determine the accompanying increase in mean phonon number. The error bars were extracted from the covariance matrix of the fitting routine. The heating rate was determined to be 65(7) phonons/s based on a linear regression model fit (dashed black line).

which have high phonon number populations, might be a mechanism capable of coupling energy into short-wavelength radial modes [141].

6.3 EIT cooling of a multi-ion crystal

In the QSim experiment, trapping of long strings of ions has been successfully demonstrated: Recent experiments carried out in the setup showed simulations of quantum Ising models with up to fifteen ions [132]. These measurements were executed using transversal modes and a repetitive sideband-cooling scheme acting on several modes. Since ground-state cooling of multiple modes was carried out to suppress unwanted heating effects due to mode coupling, more than 70% of the total cycle duration were attributed to this step. Hence, the implementation of EIT cooling promised a reduction of the experimental cycle time due to the cooling scheme's broadband cooling property. In the following, characterization techniques to prepare the beams for EIT cooling are presented, followed by results that quantify the functionality, which demonstrate the broadband behavior of the method.

6.3.1 Characterizing the EIT beams

A theoretical description of the EIT cooling method is given in Ch. 3. As a reminder, the conditions the cooling beams need to fulfill can be summarized as follows [48, 49]:

- Both EIT beams need to be blue-detuned from the atomic transition. Their detunings have to be equal to generate an electromagnetically induced transparency on to the carrier transition.

- Since the Λ -like system in $^{40}\text{Ca}^+$ consists of Zeeman sublevels from the $S_{1/2}$ and $P_{1/2}$ manifolds, the polarization of the EIT beams has to be optimized in order to drive the desired transitions only.
- The light shift induced by the stronger beam (σ^+ beam) has to be equal to the frequency of the mode(s) to be cooled. Also, the light shift induced by the weaker beam (π beam) has to be significantly smaller than the one induced by the strong beam: in our experiments a typical ratio of $\delta_\sigma/\delta_\pi \approx 20$.

These requirements are fulfilled through the choice of the beams' frequencies, polarizations and intensities accordingly.

Frequency optimization

A spectroscopic measurement on the quadrupole transition ($S_{1/2} \leftrightarrow D_{5/2}$) determines the Zeeman splitting of the ground states. This data is used to set the frequency difference of the EIT beams. In the QSim experiment, the applied magnetic field has a value of 0.4 mT, which corresponds to a Zeeman splitting of 11.4 MHz.

The overall detuning is set based on a measurement of the spectral line profile of the dipole transition ($S_{1/2} \leftrightarrow P_{1/2}$) with the Doppler-cooling laser. For the measurements presented here, the detuning is set to $2\pi \times 106(10)$ MHz. The error estimate is derived from systematic errors arising in the line center measurement.

The techniques used for EIT characterization in the Microon setup relied on determination of the optical pump rates between the Zeeman $S_{1/2}$ levels. The fit that was necessary to determine experimental parameters like induced light shift and Rabi frequency required exact knowledge of the excited state's decay rates and the laser parameters. In order to circumvent errors arising from the fit and in order to supply easily reproducible settings, two new techniques were implemented in the QSim apparatus to optimize the polarization of the σ^+ beam and to determine the induced light shifts.

Optimization of the σ^+ polarization

A quarter-wave plate in front of the vacuum chamber facilitates polarization optimization. The transition driven with the σ^+ beam, $|S_{1/2}, m = -1/2\rangle \leftrightarrow |P_{1/2}, m = +1/2\rangle$, corresponds to a change in the magnetic quantum number of $\Delta m = 1$. Transitions satisfying $\Delta m = \pm 1$ are only accessible for a circularly polarized light field propagating along the magnetic field axis. In the QSim experiment, selective driving of the σ^+ transition is achieved when the 397 nm beam is aligned along the trap axis, which is done by coupling the light through the tip holes of the linear trap, as depicted in Fig. 6.3.

A Ramsey-type experiment [142] can be used to optimize the polarization of the strong (dressing) EIT beam, as illustrated in Fig. 6.13: A 729 nm $\pi/2$ pulse prepares the ion in a superposition of the $|S_{1/2}, m = 1/2\rangle$ and the $|D_{5/2}, m = 5/2\rangle$ states. Subsequently, σ^+ polarized EIT light at 397 nm illuminates the ion before

6.3. EIT cooling of a multi-ion crystal

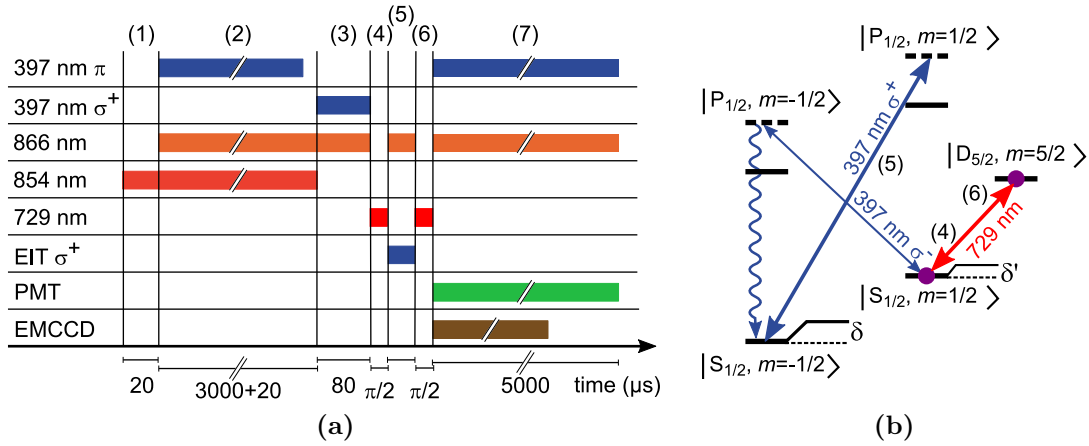


Figure 6.13. EIT polarization optimization using a Ramsey experiment. (a) Experimental sequence applied. (1) After the ion is initialized by repumping to the $|S_{1/2}, m = 1/2\rangle$ state, (2) Doppler cooling, (3) and optical pumping, (4) a $\pi/2$ pulse on the quadrupole transition $|S_{1/2}, m = 1/2\rangle \leftrightarrow |D_{5/2}, m = 5/2\rangle$ is applied. (5) This step is followed by illumination of the ion with the EIT σ^+ beam (6) and a subsequent re-interference of the population in the $|S_{1/2}, m = 1/2\rangle$ state by another $\pi/2$ pulse. (7) The electron-shelving technique is used for state detection. (b) Level scheme used in the experiment.

another $\pi/2$ pulse at 729 nm re-interferes the populations from the $|S_{1/2}, m = 1/2\rangle$ and the $|D_{5/2}, m = 5/2\rangle$ states.

If the phase of the second pulse is shifted by 90° with respect to the first pulse, an excitation of 0.5 will be measured in the case of perfect σ^+ polarization. This result arises from the absence of interaction between the σ^+ light and the states involved in the superposition.

However, σ^- -polarized light at 397 nm couples to the $|S_{1/2}, m = 1/2\rangle$ and the $|P_{1/2}, m = -1/2\rangle$ states. Hence, an unwanted component of σ^- light induces a light shift, δ' , of the $|S_{1/2}, m = 1/2\rangle$ state and can pump some of the population to the $|S_{1/2}, m = -1/2\rangle$ state. Therefore, the signal derived from the Ramsey experiment will exhibit an exponentially decaying oscillation as a function of the EIT pulse length, centered around an excitation of 0.5.

The induced light shift, δ' , causes the oscillation of the signal as it introduces a mismatch between the atomic transition frequency and the laser frequency. The decay of the signal can be attributed to a pump-out of population to the $|S_{1/2}, m = -1/2\rangle$ state (Fig. 6.13(b)), where it does not participate in the re-interference due to the second $\pi/2$ pulse. With increasing interaction time, the amount of population accumulated in this state increases, thereby diminishing the interfering population.

The polarization is optimized by adjusting the quarter-wave plate in front of the vacuum chamber in order to reduce the oscillation period of the signal as much as possible. This method allows precise reduction of unwanted polarization components on the order of 10^{-3} , using measurements such as the one shown in Fig. 6.14 [data14k].

The π -polarized EIT beam forms an angle of 60° with the trap axis. Due to optical-access constraints in the setup (see Fig. 6.2), it is not possible to achieve

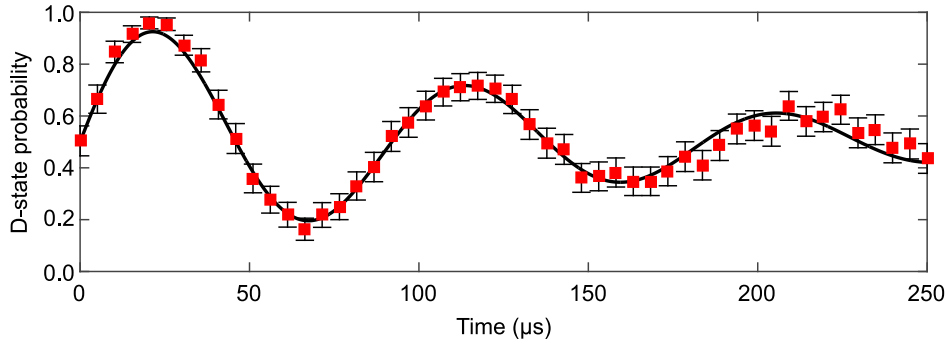


Figure 6.14. Measurement for EIT σ^+ polarization optimization with a nine-ion crystal [data14k]. The Ramsey experiment as described in the main text was used to decrease the σ^- components present in the EIT beam. These data show an unwanted induced light shift of $\delta' = 2\pi \times 10.8(5)$ kHz, which is about 200 times smaller than the set overall light shift for the σ^+ beam of $\delta = 2\pi \times 2.2$ MHz. Error bars correspond to projection noise. The solid line represents a fit to the data.

a purely π -polarized beam. The Raman k vector ($\mathbf{k}_\pi - \mathbf{k}_\sigma$) of the EIT beams forms an angle of 60° with the trap axis, which corresponds to the direction of axial mode excursion. It has equal overlap with both transversal modes, cooling both modes equally efficient.

Determination of the induced light shift

The light intensity of the EIT beams determines the induced light shift. Illuminating the ion with the σ^+ -polarized EIT beam leads to a shift of the state $|P_{1/2}, m = 1/2\rangle$, while the state $|S_{1/2}, m = -1/2\rangle$ is shifted by the same amount in the opposite direction. For effective EIT cooling with pure σ^+ polarization, the Zeeman splitting may take on any value as long as the detuning, Δ , is small with respect to the fine structure splitting, Δ_{FS} . For arbitrary polarization, $\Delta_{\text{FS}} \ll \Delta$ is required.

Spectroscopy on the quadrupole transition ($S_{1/2} \leftrightarrow D_{5/2}$) can be used to measure the induced light shift on the $|S_{1/2}, m = -1/2\rangle$ state (Fig. 6.15). After the ion is prepared in its electronic and vibrational ground state, population is transferred to the $|D_{5/2}, m = -5/2\rangle$ state by applying a π pulse with the 729 nm laser. This step is followed by illumination of the ion with the σ^+ -polarized light at 397 nm simultaneously with an excitation of the $|S_{1/2}, m = -1/2\rangle \leftrightarrow |D_{5/2}, m = -5/2\rangle$ transition with the 729 nm laser. The probability to find the ion in the $D_{5/2}$ state is determined as a function of the 729 nm laser frequency.

Within the scheme, population is optically pumped from the $|D_{5/2}, m = -5/2\rangle$ state to the $|S_{1/2}, m = 1/2\rangle$ state by the 729 nm beam and the EIT beam. The light shift induced by the EIT beam is determined from the frequency shift between the minimum of the $D_{5/2}$ -state probability in the unperturbed case and its minimum in case of illumination with the σ^+ beam.

Fig. 6.16 shows a measurement, in which the σ^+ beam is found to induce a light shift of $\delta_\sigma = 2\pi \times 2.26(1)$ MHz [data14l]. Both the EIT σ^+ beam and the 729 nm beam had a pulse length of 250 μs . The 729 nm beam was used with an optical power corresponding to a Rabi frequency of $\Omega = 2\pi \times 39$ kHz. These values

6.3. EIT cooling of a multi-ion crystal

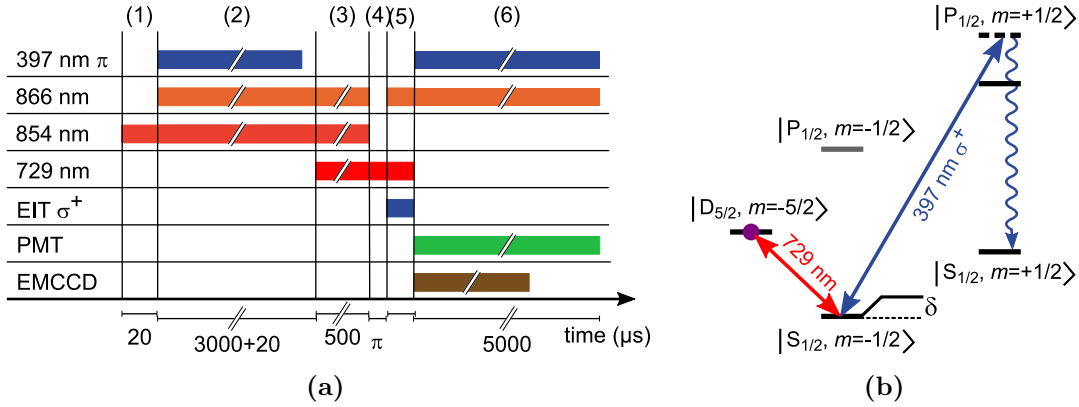


Figure 6.15. EIT light-shift optimization. (a) Pulse sequence detailing the steps to optimize the induced light shift. (1) After the ion is repumped to the $S_{1/2}$ state, (2) Doppler cooling (3) and optical pumping using the 729 nm laser is applied. Note that it is also possible to apply optical pumping using the resonant σ^+ beam at 397 nm or even a combination of both techniques. (4) Afterwards, the ion is prepared in the $|D_{5/2}, m = -5/2\rangle$ state by a π pulse with the 729 nm laser. (5) Subsequently, the 729 nm laser is scanned across the transition frequency of the $|S_{1/2}, m = -1/2\rangle \leftrightarrow |D_{5/2}, m = -5/2\rangle$ transition, while the ion is simultaneously illuminated with the EIT σ^+ light. (6) Readout is executed using the electron-shelving technique. (b) Level scheme used to optimize the light shift induced by the EIT σ^+ beam to set it equal to the motional mode frequency it should cool.

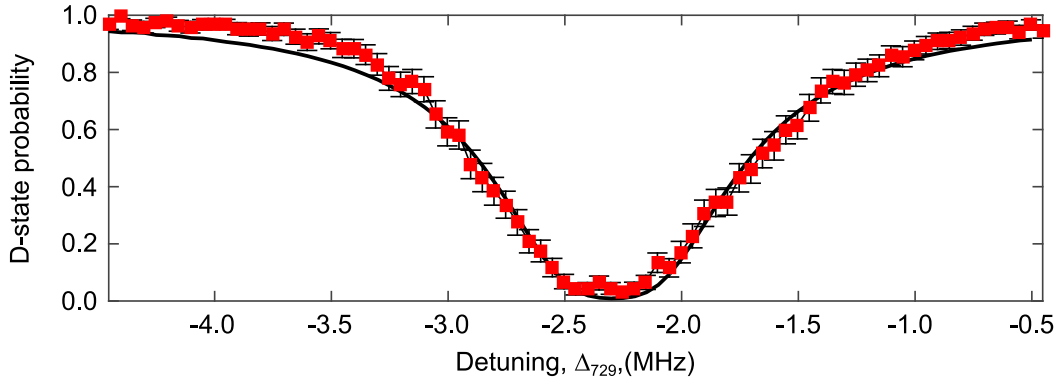


Figure 6.16. Measurement of the light shift induced by the EIT σ^+ beam with an eighteen-ion crystal [data141]. The induced light shift extracted from the fit (solid line) is $\delta = 2\pi \times 2.26(1)$ MHz. Error bars correspond to projection noise.

were chosen to achieve depletion of the $D_{5/2}$ state and simultaneously reduce power broadening of the resonance. A master-equation approach was used to numerically simulate the dynamics and thereby fit the measured excitation (solid line in Fig. 6.16). The intensity and thus the induced light shift of the π -polarized EIT beam was set using the same technique.

6.3.2 EIT cooling results

As described in Ch. 2, for fixed radial COM mode frequencies, a linear ion-crystal configuration can only be achieved as the ion number is increased if the axial COM mode frequency is reduced [77]. However, the decrease in axial frequency

is accompanied by an increase in the time necessary for gate operations, such that the heating effects play a larger role reducing the available computation time. Therefore, the use of the transversal modes to implement gate operations is beneficial, because for once, these modes are at higher frequencies and also, they are less sensitive to ion heating and thermal motion. [134].

Measurements in which the coupling of the electronic states of the ions with the transversal mode spectrum is mediated through lasers benefit from this. The study of spin-boson models and the simulation of long-range spin-spin interactions [131–133] are two topics of interest that have relied on this scheme. Hence, we choose to focus our EIT investigation on this part of the mode spectrum. A general experimental sequence including EIT cooling is presented in Fig. 6.17.

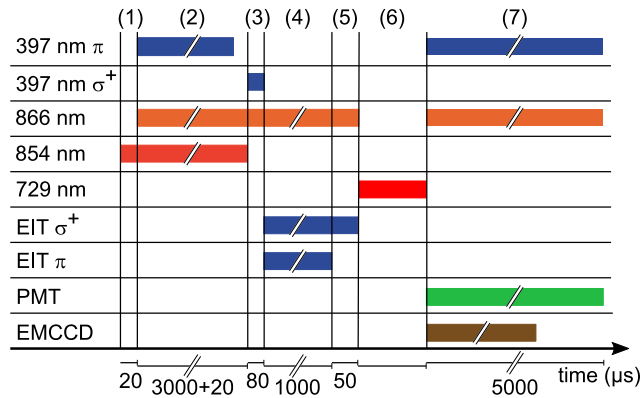


Figure 6.17. Experimental sequence for the QSim apparatus with EIT cooling. (1) Each experimental cycle begins with a repumping step, ensuring the ion no longer populates the long-lived $D_{5/2}$ state. (2) Subsequently, the ion is Doppler cooled. The infrared lasers are applied for an additional $20 \mu\text{s}$ to close the cooling cycle. (3) Thereafter, optical pumping using a resonant σ^+ polarized beam at 397 nm is carried out. The cycle is again closed with the 866 nm laser. (4) For the experiments in this section, EIT cooling is used for ground-state cooling. (5) State initialization is achieved by applying the EIT σ^+ beam for an additional $50 \mu\text{s}$ together with the laser at 866 nm . (6) After these steps, the quadrupole laser is applied to manipulate the qubit state. (7) The electron-shelving technique is used to determine the electronic state of the ion using the PMT and the camera.

We use the linear ion trap at IQOQI to characterize EIT cooling properties for large ion crystals. The investigation was carried out with an ion crystal of nine ions exhibiting trap frequencies $\{\omega_x, \omega_y, \omega_z\}_{\text{com}} = 2\pi \times \{2.76, 2.59, 0.50\} \text{ MHz}$ and a crystal of eighteen ions with trap frequencies $\{\omega_x, \omega_y, \omega_z\}_{\text{com}} = 2\pi \times \{2.71, 2.68, 0.21\} \text{ MHz}$.

Fig. 6.18 (a) shows the radial mode spectrum for the nine-ion crystal after Doppler cooling [data14m]. For comparison, Fig. 6.18 (b) illustrates the radial mode spectrum of the nine-ion crystal after an initial Doppler cooling step and subsequent EIT cooling for 1 ms [data14n]. Using the methods previously described, the light shift induced by the σ^+ beam was set to $\delta_\sigma = 2\pi \times 2.20(2) \text{ MHz}$, approximately centered within the radial mode spectrum, which corresponds to a Rabi frequency of $\Omega_\sigma = 2\pi \times 30 \text{ MHz}$. The light shift due to unwanted σ^- -polarization components was reduced to $\delta' = 2\pi \times 11.3(8) \text{ kHz}$. The π -polarized EIT beam induced a light shift of $\delta_\pi = 2\pi \times 78(6) \text{ kHz}$, which corresponded to a

6.3. EIT cooling of a multi-ion crystal

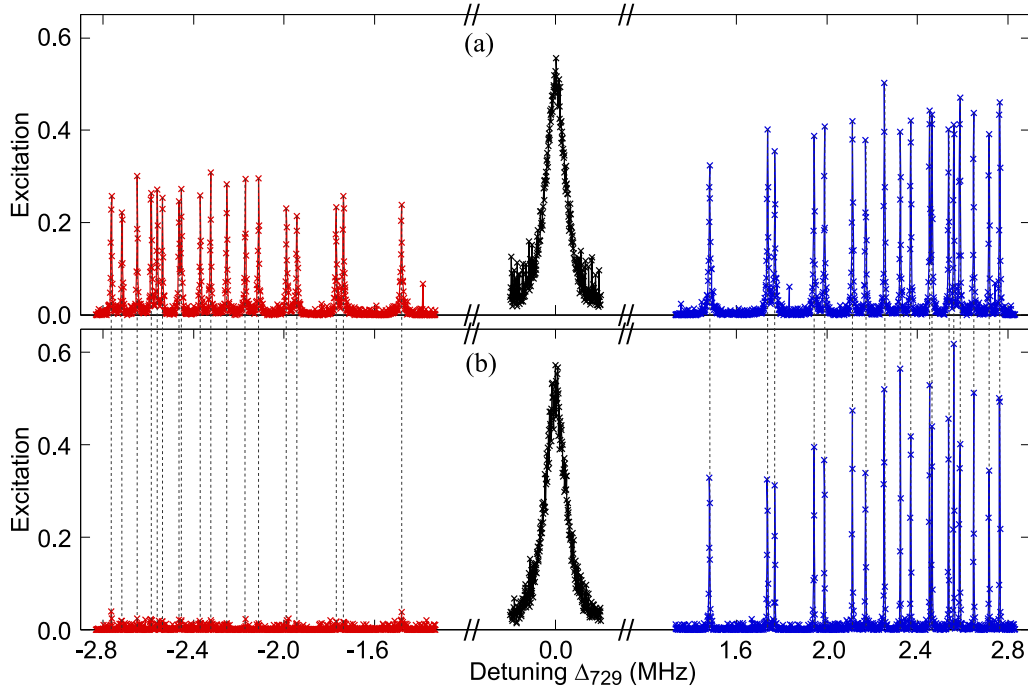


Figure 6.18. Radial mode spectra for a nine-ion crystal without [data14m] and with EIT cooling [data14n]. (a) Radial mode spectrum after 3 ms of Doppler cooling. (b) Radial mode spectrum after 3 ms of Doppler cooling and a subsequent 1 ms EIT cooling pulse. The σ^+ -induced light shift was set to $2\pi \times 2.20(2)$ MHz. Dashed lines between (a) and (b) serve to aid a comparison of the spectra. As is illustrated, the EIT cooling worked simultaneously on all radial modes spread over a range of 1.2 MHz. The additional weak excitations which appear in the wings of the Doppler cooled carrier spectrum in (a) (black curve) can be attributed to second-order sideband processes that exchange phonons between two radial modes.

Rabi frequency of approximately $\Omega_\pi = 2\pi \times 6$ MHz.

A similar result was obtained for the eighteen-ion crystal, as illustrated in Fig. 6.19 [data14o] [data14p]. In this case, the σ^+ light shift was set to $\delta_\sigma = 2\pi \times 2.26(1)$ MHz, in the lower frequency range of the observed radial mode spectrum, which extended between $2\pi \times 2.71$ MHz and $2\pi \times 2.08$ MHz. We chose this light shift setting to investigate whether the EIT cooling method was capable to cool all radial modes, despite a shift from the center of the radial mode spectrum. Unwanted light shifts from σ^- components could be reduced to $\delta' = 2\pi \times 18(2)$ kHz. Here, the π -beam intensity was set to induce a light shift of $\delta_\pi = 2\pi \times 100(13)$ kHz, about twenty times smaller than the σ^+ -induced light shift. All radial modes spread over 0.6 MHz could be cooled simultaneously into or close to the ground state by the application of a single EIT cooling pulse with a duration of 1 ms, as shown in Fig. 6.19 (b).

The reduced red-sideband absorption after EIT cooling observed in both Fig. 6.18 and Fig. 6.19 is a strong indication of ground-state cooling. However, as discussed in Ch. 3, the average mean phonon number can not be determined for a multi-ion crystal by a comparison of the red-sideband and blue-sideband absorption probabilities. This is illustrated in the nine-ion Doppler-cooled spectrum Fig. 6.18 (a): Even though the mean phonon number expected from Doppler

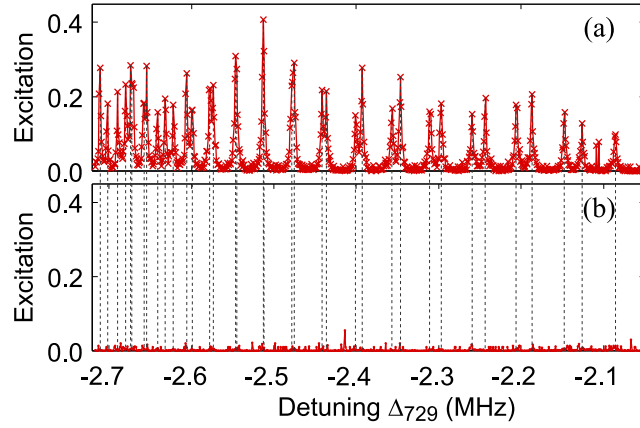


Figure 6.19. Radial mode spectra of an eighteen-ion crystal without [data14o] and with EIT cooling [data14p]. (a) Red-sideband radial mode spectrum after 3 ms of Doppler cooling. (b) Red-sideband radial mode spectrum after 3 ms of Doppler cooling and a subsequent 1 ms EIT cooling pulse. The σ^+ -induced light shift was set to $2\pi \times 2.26(1)$ MHz. Dashed lines between (a) and (b) serve to aid a comparison of the spectra. As illustrated, the EIT cooling worked simultaneously on all radial modes spread over a range of 0.6 MHz.

cooling $\langle n \rangle \approx 5$, an asymmetry in the absorption is found. For a single trapped ion, such an asymmetry would be the signature for cooling close to the ground state, $\langle n \rangle \approx 2$ (Ch. 3, Eq. 3.36).

In the single-ion case, the asymmetry of the absorption spectrum can be attributed to $n = 0$ being a dark state for excitation on the red-sideband transition. For multi-ion crystals, $n = 0$ is still a dark state for excitation on the red-sideband transition, but higher number states exhibit different coupling strengths for red-sideband and blue-sideband excitations. In general, the lowest phonon states $n = 0, \dots, N$, with N being the number of ions in the crystal, show different coupling strength for the red sideband and blue sideband. Hence, even for $\langle n \rangle > 1$ multi-ion crystals exhibit asymmetric absorption spectra.

A numerically simulated spectrum of the nine-ion crystal taking into account the experimental parameters resembled the red-sideband absorption spectrum of Fig. 6.18 (a) for a thermal phonon distribution with $\langle n \rangle \approx 5 - 8$. The calculations were based on N two-level atoms coupled by a homogeneous laser beam to the mode of interest only. This approach yields $N + 1$ coupled states, $|\psi_k^n\rangle = (\hat{S}^+)^k |0, n\rangle$, with \hat{S}^+ an electronic raising operator³², and $|j, n\rangle$ an N -ion state with j electronic and n vibrational excitations. For the blue-sideband spectrum, a similar correspondence between the experimental observation and the simulation was found.

We introduce RAP as a better measure for the vibrational excitation of a mode in a multi-ion crystal. The technique was used to determine the cooling dynamics present with EIT cooling. The data below have been measured using the same eighteen-ion crystal already introduced for the radial mode-spectrum

³²The definition of the electronic raising operator is $\hat{S}^+ = \sum_{i=1}^N \eta_{i\nu} \sigma_i^+ a_i$, with $\eta_{i\nu}$ the Lamb-Dicke factor of the i th ion and ν the motional mode frequency.

6.3. EIT cooling of a multi-ion crystal

measurement. The preparation consisted of Doppler cooling, EIT cooling and optical pumping to the $|S_{1/2}, m = 1/2\rangle$ state. The EIT settings were $\delta_\sigma = 2\pi \times 2.26(1)$ MHz, $\delta' = 2\pi \times 18(2)$ kHz and $\delta_\pi = 2\pi \times 100(13)$ kHz, as already introduced.

The vibrational excitation of the mode was mapped to the electronic excitation of the ions in the crystal by RAP implemented on the lowest-frequency radial motional mode at $2\pi \times 2.08$ MHz. Readout of the ions' individual electronic states was performed via the EMCCD camera. The data obtained were analyzed in terms of the probability for ion number excitation. Fitting a thermal distribution of states to the experimentally derived phonon-number distribution yielded the mean phonon number.

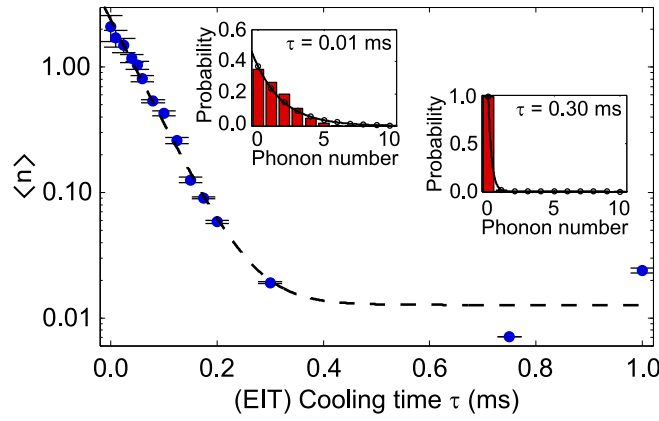


Figure 6.20. EIT cooling dynamics for an eighteen-ion crystal measured on the radial mode at $2\pi \times 2.08$ MHz [data14r]. The ions were subject to 3 ms of Doppler cooling and EIT cooling pulses of varying duration. The light shift induced by the σ^+ beam was $2\pi \times 2.26(1)$ MHz. After the cooling step, RAP was implemented to determine the mean phonon number. The histograms (insets) determined from the EMCCD camera data give the probability for observing a given number of excited ions (from no ions to eighteen ions). The mean phonon number was derived from a thermal distribution fit to the data, which represent the phonon-number distribution (solid line). A least-square fit (dashed line) applied to the measured mean phonon numbers gives a cooling rate of $19(3) \times 10^3 \text{s}^{-1}$.

The insets of Fig. 6.20 show the histograms extracted from the camera data for an EIT cooling time of 0.01 ms and 0.30 ms. The depicted black solid line is a thermal distribution fit to extract the mean phonon number. The mean phonon numbers, illustrated in the Fig 6.20 as blue dots, correspond to such a histogram each. The mean phonon number decreases exponentially with increasing cooling time, achieving values below $\langle n \rangle = 1$ after 0.05 ms and reaching a steady state after 0.30 ms of EIT cooling.

An exponential fit was applied to the data to derive the cooling dynamics of the process (dashed line in Fig. 6.20). This method is based on the time evolution of the mean phonon number, which can be solved using the equation $\langle n(t) \rangle = Ae^{-rt} + n_{\text{eq}}$ with A being a constant, and n_{eq} representing an offset term (see also Ch. 5, Sec. 5.3.2). A fit to calculate the cooling rate based on this formula yields a too small cooling rate as the absolute deviation between measurement and fit for long cooling times is small as well. However, the relative deviation between

data and fit for long cooling times is large. This discrepancy can be taken into account by applying a least-square fitting routine to the logarithm of the data thus ensuring a more appropriate weighting for data taken at longer cooling times. With this approach, the cooling rate was found to be $19(3) \times 10^3 \text{ s}^{-1}$.

Typical cooling rates for sideband cooling of $^{40}\text{Ca}^+$ in macroscopic traps are on the order of $^{33} 5 \times 10^3 \text{ s}^{-1}$. A comparison of the cooling rates for the different methods show approximately a fourfold increase for EIT cooling.

The results presented in this section show the superior abilities of EIT cooling compared to sideband cooling: the combination of fast ground-state cooling of a large number of modes, demonstrated in Fig. 6.20, Fig. 6.18 and Fig. 6.19.

Summary

In this chapter, the setup of QSim at IQOQI, is introduced, which has been used to implement EIT cooling and rapid adiabatic passage for long strings of ions. In contrast to the setup presented in the previous chapters, the QSim setup is based on a macroscopic linear Paul trap.

As our major interest in this investigation was to work with multi-ion crystals, this chapter details various techniques to determine the mean phonon number in such a configuration. One technique uses the dynamics of global excitation on the blue sideband and was implemented using a four-ion crystal. However, this method represents a very indirect way of determining the mean phonon number.

We applied rapid adiabatic passage as a single shot measurement to determine the vibrational excitation of a given motional mode. In this chapter, the RAP process itself is characterized using specifically prepared Fock states. Furthermore, the implementation of RAP to determine heating rates and cooling dynamics for multi-ion crystals is introduced. Additionally, the technique offers the possibility to generate large Fock states.

We investigated EIT cooling in order to apply this technique for fast multi-mode cooling on multi-ion crystals. In this chapter, two novel approaches to the beam characterization are presented. In addition, the application of the method to a nine-ion crystal and an eighteen-ion crystal are shown: We successfully applied EIT cooling on all radial motional modes of these ion crystals, thereby covering a frequency range of up to 1.2 MHz. This results were based on a single EIT cooling step of 1 ms, addressing all radial motional modes simultaneously. Furthermore, our investigation of the cooling rates achieved with the technique showed approximately a fourfold increase as compared to the typical cooling rate for sideband cooling. The properties demonstrated in our measurements show that the application of EIT cooling is specifically effective for multi-ion crystals.

³³The stated value corresponds to a recently measured value for a trap of similar built than the one used in the QSim trap.

7

Summary and outlook

In this thesis, multi-mode cooling techniques for long strings of ions are investigated along with methods to determine the phonon number of a motional mode in such a system. Our results highlight the fast broadband cooling behavior of EIT cooling. These properties are highly beneficial to increase the number of ions available for a computation in a trapped ion quantum computer. The experiments presented have been carried out in two different traps: a microtrap in sandwich geometry and a macroscopic linear Paul trap.

Our primary incentive to investigate cooling techniques in the Mircreon apparatus was to find a reliable method of operation despite the high heating rates in that trap, which are attributed to the small electrode-ion distance [73]. Previously, a combination of Doppler cooling modified by a dark resonance and sideband cooling of the axial motional mode achieved ground-state cooling of said mode [84]. However, during the course of this work, we observed an increase in the mean phonon number after sideband cooling of a single trapped ion. Thus, we investigated the heating rates of the system, to compare this parameter to measurement values obtained two years prior. Although the mean phonon number of the axial motional mode achieved after sideband cooling was higher by more than a factor of ten, the extracted heating rate corresponded with our previous measurements.

In order to fully characterize the heating rates of the system, we decided to carry out an investigation of the radial modes. However, a single sideband cooling step, which addressed the measured mode, did suffice to observe Rabi oscillations only in one of the two radial directions. Our conclusion was, that a high phonon occupation number of the neighboring mode influenced the measurement [37]. Thus, we decided to implement repetitive sideband cooling as a multi-mode cooling technique. In Ch. 5, the results based on this technique are presented. Not only could the mean phonon number of the axial motional mode be decreased by approximately 20%, but also heating-rate measurements of the radial modes were carried out for the first time in the Mircreon trap. With values of several hundred phonons/s, the observed heating rates correspond to empirically derived data found in the literature for traps with similar electrode-ion distances [73].

Consecutive sideband cooling on multiple modes is a slow process, that takes a sizable amount of the experimental cycle time: for the results presented in Ch. 5, Sec. 5.2, about 65% of the experimental cycle duration was spent on sideband cooling. In addition, consecutive cooling of the modes allows the modes cooled first to be heated in the time it takes to cool the other modes. This effect can

be attributed to the cooling time of one mode representing a waiting time for the uncooled modes. Such a situation is disadvantageous, specifically for traps that exhibit high heating rates.

Based on these reasons, we considered EIT cooling as a further improvement of the experimental system. As demonstrated in Innsbruck more than a decade ago [49], EIT cooling offers the properties of a broad cooling bandwidth, which enables simultaneous cooling of multiple modes, and fast cooling rates. We regarded the combination of these properties specifically useful, since the long-term goal for the Microon trap was trapping of long ion crystals (ten ions and more) in anharmonic trapping potentials.

We characterized the cooling efficiency and cooling rates for all six motional modes of a two-ion crystal (see Ch. 5). The determined cooling bandwidth during which a mean phonon number of $\langle n \rangle = 1$ and below is achieved is approximately 1 MHz. The fast cooling rates resulted in a duration of 1 ms to accomplish cooling into or close to the ground state. In contrast to the repetitive sideband cooling scheme, this corresponds to less than 20 % of the total experimental cycle time. In addition, an overlap of cooling into the ground state (below $\langle n \rangle = 1$) for several motional modes was observed: cooling of all radial modes could be achieved simultaneously with the induced light shift corresponding to a frequency in the middle of this mode spectrum.

We planned further investigations involving longer ion crystals and specifically generated quartic trapping potentials. Quartic potentials would allow us to confine equidistant strings of ions. Such a situation would enable stable trapping of long strings of ions (theoretically, hundreds of ions and more) [57]. Thereby, the number of ions, whose electronic states represent the smallest processing unit of a quantum computer, could be scaled up. Ultimately, the measurements we wanted to implement in the Microon trap were envisaged to show the ability to increase the number of ions available for quantum computation with anharmonic trapping potentials. This accomplishment would bring us closer to the goal of outperforming a classical computer with a quantum computer. However, we were not able to carry out these investigations due to the limited stability of multi-ion crystals in the Microon trap.

Therefore, the investigation of the EIT cooling properties was moved to the macroscopic linear trap setup. In this apparatus, long strings of up to twenty ions and more can be trapped for several hours in a harmonic potential. As the mode spectrum becomes denser with an increasing number of trapped ions, we wanted to investigate EIT cooling as a way to efficiently cool a large part of this spectrum.

Investigations of the Ising spin model, which were carried out prior to the application of the new cooling technique, were implemented using transversal modes [132]. The application of the radial mode spectrum for gate operations is advantageous, since the gate operation times are faster compared to the axial gate operations, which are implemented at lower frequencies. Also, the transversal modes are less sensitive to ion heating and thermal motion. Thus, we concentrated our examination of EIT cooling on this part of the mode spectrum.

We implemented EIT cooling for ion crystals of up to eighteen ions. The data

show that we can simultaneously cool all radial modes over a range of 1.2 MHz with a single EIT pulse of 1 ms. Thus, we could reduce the typical time within a sequence allocated to cooling from approximately 70 % for repetitive sideband cooling to about 10 % for EIT cooling. This represents a lower limit for the total gain, since the sideband cooling scheme is applied on a limited number of radial modes only, while EIT cooling works on all radial modes.

All results obtained in the linear-trap apparatus showed that we have the capability for fast multi-mode cooling with EIT cooling. However, the beam configuration currently used has a component of the Raman k vector coupling to the axial modes of motion. For experiments with long strings of ions, the axial mode frequencies have to be low to enable a linear crystal configuration (see Ch. 2 and references [77–79]), and the expected mean phonon numbers of these modes are therefore high¹. In the cooling investigation, heating of the axial modes was observed when EIT cooling was applied to the radial mode spectrum. Therefore, we took measurements of the axial mode spectrum of a single ion. The data obtained showed a vibrational excitation after EIT cooling of $\langle n \rangle \approx 320$. This high vibrational excitation turned out to be a major obstacle for an implementation of EIT cooling into the regular experimental routine.

Currently, the beam alignment is constrained by the geometry of the setup. A change of the magnetic field axis and the optical setup would be necessary to eliminate the axial component of the Raman k vector and thereby the axial heating. This step is crucial for future use of the EIT cooling method in the macroscopic trap apparatus. However, the experiments planned for the near future are still feasible if we apply sideband cooling. In addition, the change in the setup would lead to a downtime of the apparatus that with the number of currently planned experiments not relying on EIT cooling is not justifiable.

An additional result we obtained during our investigation of EIT cooling is based on novel techniques to determine the mean phonon number of a multi-ion crystal. Two methods are presented in this work, both relying on a globally applied laser excitation: the recording of Rabi oscillations on the blue sideband driven globally on all ions represents an indirect measurement, while the global application of [rapid adiabatic passage \(RAP\)](#) is a single-shot measurement.

We applied the method based on global blue-sideband Rabi oscillation to a four-ion crystal. In this work, the resulting data are presented with a theoretical fit based on solutions of the Schrödinger equation to extract the initial phonon population distribution (Ch. 6). The method relies on the precise knowledge of the Rabi frequency and experimental parameters as inputs for the fitting routine.

In addition, we implemented [rapid adiabatic passage](#), which uses a global pulse on the red-sideband excitation to map the vibrational excitation of a mode directly to the electronic excitation within the ion chain. We tested the method by measuring specifically prepared Fock states using addressed blue-sideband excitation. This analysis showed the capability of RAP to reliably reproduce a target state.

¹From Ch. 3 Eq. 3.20, one can conclude that a frequency of 1 MHz results in $\langle n \rangle \approx 11$, while a frequency of 0.2 MHz results in $\langle n \rangle \approx 54$.

We present results for the application of RAP to study heating and cooling dynamics of our system: the heating rate of the COM mode of a nine-ion crystal was measured, as well as the EIT cooling dynamics on the lowest radial mode of an eighteen-ion crystal. In both cases, the application of RAP enabled quick and efficient measurements.

Depending on the sideband across which [rapid adiabatic passage](#) is applied, it is not only possible to read out the phonon number distribution, but also to create large Fock states or entangled states [111]. We implemented RAP on a blue sideband of a nine-ion crystal to create Fock states. This work presents data for a Fock state $n = 27$. This is, to our knowledge, one of the biggest Fock states created with trapped ions up to now.

The results presented in this work show the superior properties of EIT cooling as compared to other ground-state cooling techniques, like, for example, sideband cooling. The characterization we present emphasizes the method's usefulness in the research field of trapped ion quantum computation, which has also been shown for a mixed four-ion crystal in reference [50]. Moreover, EIT cooling has proven its versatility in a number of other areas: cavity-QED experiments [52], nanomechanical resonators [53], and quantum-gas microscopy [51].

For the future, we plan to implement RAP as a way to create symmetric Dicke states in the macroscopic linear trap. Such multipartite entangled states are one integral component for quantum computers. Furthermore, these states are used to transmit information over separate channels, for example, in a teleportation protocol. Thus, they play a central role in quantum cryptography. Aside their usefulness for quantum information science, multipartite entangled states can also be applied to increase the sensitivity of atomic clocks.

The highest rate of entanglement can be achieved by applying RAP on the COM mode. However, it is also this mode that has the highest heating rate, which, in addition, increases the longer the ion crystal becomes. Thus, in my opinion, a combination of EIT cooling, which works faster and on a broader frequency range than sideband cooling, and RAP would enable the multipartite entanglement of large ion crystals (more than fourteen ions). These measurements would require a modification of the QSim apparatus, as already described. In addition, the cooling duration within an experimental sequence would be shorter as compared to the current status. Thus, we could apply more gate operations before decoherence effects set in.

An application of EIT cooling to other ion trap designs and potential configurations could be considered. An array of ions trapped in neighboring potentials might exhibit different trap frequencies. The application of a single EIT cooling pulse could be used to cool all ions at once without the need of addressing each individual ion and each motional frequency.

A

Anharmonic trapping potentials

Segmented traps were initially conceived so that multiple harmonic trapping potentials could be created in close proximity to each other [34, 67]. The transport of ions between different zones assigned to loading and storing of ions and zones for quantum manipulation was envisaged. Later, it was realized that the segmentation could also be used to allow the tailoring of potentials with higher-order multipoles [76]. Hence, segmented electrodes facilitate the generation of chains of equidistant ions [57].

Uniformly spaced ion chains in anharmonic potentials are interesting as they offer greater stability of the linear chain configuration as compared to ion crystals in a harmonic potential [78, 85, 143]. Although the axial motional frequencies are expected to be low, which is disadvantageous for gate operations implemented with these modes, the transverse motional modes can be used to implement quantum simulations [134, 143]. Furthermore, single-ion addressing is not limited in the same way as for a harmonic potential, where the minimum inter-ion distance is dependent on the number of trapped ions. In this appendix, the considerations behind the generated potential are outlined along with an overview of the maths used to calculate the equilibrium positions of ions.

Basic considerations for an equidistant ion chain

For a chain of N ions within a trapping potential, there are two forces counteracting each other: the external trapping force confining the ions and the Coulomb repulsion between the ions. The ion position can be linearized in the form of a time-dependent equilibrium position and a small oscillation around this position (see also Sec. 2.2.1). In general, the equilibrium positions can be calculated from balancing the confining potential and the Coulomb potential.

In order to generate a uniformly spaced ion crystal, the specified equilibrium positions serve as a starting point for the considerations. From these positions, the Coulomb force at each ion position can be calculated, and the external electric field to counteract the repulsion is given by

$$E_{\text{ext}}(z_i) = -\frac{1}{2} \frac{e}{4\pi\epsilon_0} \sum_{\substack{j=1 \\ j \neq i}}^N \frac{\text{sgn}(z_i - z_j)}{(z_i - z_j)^2}, \quad (\text{A.1})$$

with e the electron charge, ϵ_0 the vacuum permittivity, and z_i the position of the i th ion along the trap axis. The external electric field determined in this

Appendix A. Anharmonic trapping potentials

fashion is valid only at the ions' position but an interpolation from these points is possible. A good ansatz to interpolate the field from $E_{\text{ext}}(z_i)$ to $E_{\text{ext}}(z)$ for an equally spaced chain is a harmonic series¹, yielding the expression

$$E_{\text{HS}}(z) = -\frac{2e}{\pi\epsilon_0 d_0^2} \left(\frac{z/d_0}{N^2 - (2z/d_0)^2} \right), \quad (\text{A.2})$$

with the inter-ion distance d_0 . An illustration of the field as a function of position is presented in Fig. A.1(a) for a crystal of eighteen singly charged ions with an inner spacing of $4.8 \mu\text{m}$.

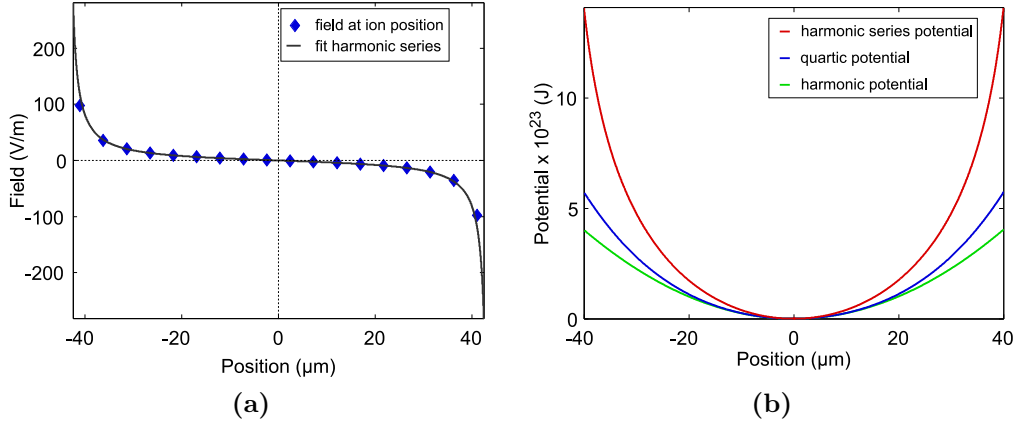


Figure A.1. Electric field and corresponding potential required to trap a string of eighteen equidistant ions with an inter-ion distance of $4.8 \mu\text{m}$. (a) The electric field due to eighteen singly charged point charges equidistantly spaced $4.8 \mu\text{m}$ apart (blue diamonds) is illustrated. Also, a fit using a second-order hyperharmonic series approximation to the position to extract the corresponding external electric field is presented (black curve). (b) External potential needed to generate an equidistant chain of eighteen ions with $4.8 \mu\text{m}$ inter-ion distance. The red curve shows the anharmonic potential derived directly from Eq. A.3, while the blue curve illustrates the solution for a Taylor expansion of the harmonic series terminated after the fourth term (Eq. A.5). The derived coefficients are $\kappa_2 = 5.04 \times 10^{-14} \text{ J m}^{-2}$ and $\kappa_4 = 2.66 \times 10^{-5} \text{ J m}^{-4}$. The green curve shows the Taylor expansion for termination after the second term, yielding a harmonic potential with a frequency of $\omega_z = 2\pi \times 0.138 \text{ MHz}$. As illustrated, the series approximation leads to a deviation between the potential based on the harmonic series and the quartic potential. This leads to a deviation of the realized inter-ion distance from the initial equidistant setting.

From the interpolated formula for the electric field, the external potential, Φ , to confine the particles can be calculated as

$$\Phi(z) = -\frac{e^2}{4\pi\epsilon_0 d_0} \ln \left(\frac{N^2}{N^2 - (2z/d_0)^2} \right). \quad (\text{A.3})$$

Fig. A.1(b) depicts the required potential that emerges from the presented considerations for a crystal of eighteen singly charged ions with an inter-ion distance of $4.8 \mu\text{m}$.

¹For the interpolation here, a hyperharmonic series is chosen, given in general as $HS(k) = \sum_{m=1}^k m^{-2} = \frac{\pi^2}{6} - \frac{2}{1+2k} \left(1 - \frac{1}{6(1+2k)^2} \right)$.

In order to physically realize the calculated potential (Eq. A.3) using a segmented ion trap, it is advantageous to expand the expression given in Eq. A.3 as a power series, yielding

$$\Phi_{\text{approx}}(z) \approx -\frac{e^2}{4\pi\epsilon_0 d_0^2} \left(\frac{4}{d_0 N^2} z^2 + \frac{8}{d_0^3 N^4} z^4 \right). \quad (\text{A.4})$$

In this form, the potential coefficients can be connected to the generic coefficients of the quartic potential also mentioned in Ch. 2, (Eq. 2.17)

$$U(z) = \frac{\kappa_2}{2} z^2 + \frac{\kappa_4}{4} z^4, \quad (\text{A.5})$$

which are denoted κ_2 and κ_4 . These two coefficients can now be related not only to the power series in Eq. A.4 but also to the voltages applied to the trap and the emerging secular frequency ($\kappa_2 = m\omega_z^2$),

$$|\kappa_2| \approx \frac{2e^2}{\pi\epsilon_0 d_0^3 N^2}, \quad (\text{A.6})$$

$$|\kappa_4| \approx \frac{8e^2}{\pi\epsilon_0 d_0^5 N^4}. \quad (\text{A.7})$$

The outcome of this Taylor expansion is illustrated in Fig. A.1(b), which compares the ideal case taking into account the full harmonic series approach with the quartic (harmonic) potential derived from a series expansion terminated after the fourth (second) term. All cases refer to an eighteen ion crystal with an inter-ion spacing of 4.8 μm , which is the same configuration as in Sec. 2.2.2 of Ch. 2. However, as is presented in Fig. A.1(b), the confinement related to the quartic and harmonic potentials is far less strong as the confinement arising from the harmonic series potential. Therefore, it is expected that the ion positions along the trap axis and hence the inter-ion distance derived for the approximations deviate from the initially chosen target value of 4.8 μm . This deviation is illustrated in Ch. 2.

The presented approach combined with a simulation of the potentials generated by each electrode pair allows one to calculate the voltages for an anharmonic trapping potential with nearly equidistant spacing. However, because the implemented anharmonic potential is only an approximation of the ideal case, based on a truncated harmonic series, uniform spacing over the whole chain cannot be achieved.

Derivation of the equilibrium positions

The potential energy for a string of N ions within a static quartic (pseudo) potential generated by a segmented Paul trap can be expressed as

$$\begin{aligned}
 U(x, y, z, t) = & \frac{m}{2} \sum_{i=1}^N \left(\omega_x^2 x_i^2(t) + \omega_y^2 y_i^2(t) \right) + \sum_{i=1}^N \left(\frac{\kappa_2}{2} z_i^2(t) + \frac{\kappa_4}{4} z_i^4(t) \right) \\
 & + \frac{1}{2} \frac{e^2}{4\pi\epsilon_0} \sum_{\substack{j,i=1 \\ j \neq i}}^N \frac{1}{|\mathbf{r}_j(t) - \mathbf{r}_i(t)|}.
 \end{aligned} \tag{A.8}$$

For cold ions, an approximation as described in Eq. 2.9 can be applied, splitting the coordinates in a static term (\mathbf{r}_i^0) and a time dependent term ($\mathbf{q}_i(t)$). The usual linear configuration along the trap axis (z axis) further simplifies the calculation of the ions' equilibrium positions, as they can be described by ($x_i^0 = 0, y_i^0 = 0, z_i^0$). Taking the derivative of the potential given in Eq. A.8 and taking into account the linear crystal shape leads to the following steps:

$$\begin{aligned}
 \left[\frac{\partial U}{\partial z_i} \right]_{z_i=z_i^0} &= \frac{\partial}{\partial z_i} \left(\sum_{i=1}^N \left(\frac{\kappa_2}{2} z_i^2 + \frac{\kappa_4}{4} z_i^4 \right) + \frac{e^2}{8\pi\epsilon_0} \sum_{\substack{j,i=1 \\ j \neq i}}^N \frac{1}{|z_j - z_i|} \right) \\
 &= \frac{\partial}{\partial v_i} \frac{1}{b} \left(\sum_{i=1}^N \left(\frac{\kappa_2}{2} b^2 v_i^2 + \frac{\kappa_4}{4} b^4 v_i^4 \right) + \frac{e^2}{8\pi\epsilon_0} \frac{1}{b} \sum_{\substack{j,i=1 \\ j \neq i}}^N \frac{1}{|v_j - v_i|} \right) \\
 &= \left(\sum_{i=1}^N (v_i + B v_i^3) - \sum_{\substack{j,i=1 \\ j \neq i}}^N \frac{1}{|v_j - v_i|^2} \right) = 0.
 \end{aligned} \tag{A.9}$$

The following substitutions (which are also stated in Eq. 2.18) have been applied,

$$\begin{aligned}
 v_i &= \frac{z_i^0}{b}, \\
 b &= \left(\frac{e^2}{4\pi\epsilon_0\kappa_2} \right)^{1/3}, \\
 B &= \frac{\kappa_4}{\kappa_2} b^2 = \frac{\kappa_4}{\kappa_2} \left(\frac{e^2}{4\pi\epsilon_0\kappa_2} \right)^{2/3},
 \end{aligned} \tag{A.10}$$

with the dimensionless coordinate v_i , the length scale b , and the dimensionless ratio B . The system of N coupled equations presented in Eq. A.9 can be solved numerically, yielding the positions of ions in an anharmonic, quartic potential dependent on the externally applied voltages.

B

List of publications

The work in this thesis has been presented to the public in the following publication:

- R. Lechner, C. Maier, C. Hempel, P. Jurcevic, B. P. Lanyon, T. Monz, M. Brownnutt, R. Blatt, and C. R. Roos,
Electromagnetically-induced-transparency ground-state cooling of long ion strings,
Physical review A **93**, 053401 (2016).
(arXiv:1603.05568)

Furthermore, the author of this work has contributed to the following publication:

- M. Harlander, R. Lechner, M. Brownnutt, R. Blatt, and W. Hänsel,
Trapped-ion antennae for the transmission of quantum information,
Nature **471**, 200 (2011).
(arXiv:1011.3639)

C

List of datasets

In order to increase the traceability of the measurement data displayed in this thesis, each dataset is tagged with an index referring to the year it was taken in. In this appendix, each index used can be found with a short description of what is displayed, the notebook number used to catalogue the measurement and the date and time when the data were taken. The date and time are also used as label for electronic storage of the data on the group server: data obtained with the Microon trap are stored in the folder “segfalle” and data taken with the linear trap are stored in the folder “calcium43”. For results presenting a larger number of single measurement results, the first and last timestamp is indicated.

[data12a] **page 56**

Single ion; Rabi oscillations;
Labbook # 10, page 23;
Time: 1122⁰² ,
Date: February 21st, 2012

[data12b] **page 56**

Single ion; drifts in maximum $D_{5/2}$ -state population;
Labbook # 10, page 23;
Time: 1055
Date: February 21st, 2012

[data12c] **page 59**

Single ion; Rabi oscillation improved by sample-and-hold circuit on Doppler-cooling beams;
Labbook # 10, page 97;
Time: 1441⁰² ,
Date: June 28th, 2012

[data12d] **page 59**

Single ion; drifts in maximum $D_{5/2}$ -state population improved by sample-and-hold circuit on Doppler-cooling beams;
Labbook # 10, page 97;
Time: 1500
Date: June 28th, 2012

[data12e] **page 64**

Single ion; axial heating rate measurement, axial sideband cooling only;

Labbook # 10, page 100;
Time: 1555 - 1603⁰⁶
Date: June 29th, 2012

[data12f] **page 65**
 Single ion; axial heating rate measurement, sideband cooling all motional modes;
 Labbook # 10, page 115;
Time: 1108 - 1121⁰²
Date: July 19th, 2012

[data12g] **page 65**
 Single ion; radial heating rate measurement, sideband cooling all motional modes;
 Labbook # 10, page 116;
Time: 1153 - 1207⁰²
Date: July 19th, 2012

[data12h] **page 65**
 Single ion; radial heating rate measurement, sideband cooling all motional modes;
 Labbook # 10, page 116;
Time: 1234 - 1247⁰²
Date: July 19th, 2012

[data14a] **page 69**
 Single ion; EIT σ^+ -induced light-shift characterization;
 Labbook # 19, page 180;
Time: 1513
Date: January 15th, 2014

[data14c] **page 74**
 Two-ion crystal; cooling dynamic for EIT cooling;
 Labbook # 19, page 183-186;
Time: 1453 - 2126
Date: January 17th, 2014

[data14d] **page 86**
 Single ion; radial heating rate measurement, one radial mode sideband cooled only;
 Labbook # 25, page 72;
Time: 1432 - 1436⁰³
Date: September 30th, 2014

[data14e] **page 86**
 Single ion; radial heating rate measurement, one radial mode sideband cooled;
 Labbook # 25, page 72;
Time: 1518 - 1519⁰³
Date: September 30th, 2014

[data14f] **page 87**
 Four-ion crystal; global blue-sideband excitation;
 Labbook # 25, page 68;
Time: 1451 - 1501
Date: September 25th, 2014

List of datasets

- [**data14g**] **page 91**
Nine-ion crystal; Fock state measurement with rapid adiabatic passage;
Labbook # 25, page 102/103;
Time: 1551 - 1801
Date: October 22nd, 2014
- [**data14i**] **page 96**
Nine-ion crystal; Fock state measurement with addressed blue-sideband pulse length scan;
Labbook # 25, page 105;
Time: 1856 - 2037
Date: October 23rd, 2014
- [**data14j**] **page 98**
Nine-ion crystal; heating rate measurement using rapid adiabatic passage;
Labbook # 25, page 76;
Time: 1818 - 1847
Date: October 1st, 2014
- [**data14k**] **page 101**
Nine-ion crystal; σ^+ polarization optimization using a Ramsey experiment;
Labbook # 25, page 138;
Time: 1340
Date: December 3rd, 2014
- [**data14l**] **page 102**
Eighteen-ion crystal; EIT beam induced light shift measurement;
Labbook # 25, page 128;
Time: 1055
Date: November 26th, 2014
- [**data14m**] **page 104**

Nine-ion crystal; Doppler cooled radial mode spectrum;
Labbook # 25, page 135;
Time: 0947 - 1319
Date: December 2nd, 2014
- [**data14n**] **page 104**
Nine-ion crystal; Doppler and EIT cooled radial mode spectrum;
Labbook # 25, page 136;
Time: 1400 - 1755
Date: December 2nd, 2014
- [**data14o**] **page 105**
Eighteen-ion crystal; Doppler cooled red-sideband radial mode spectrum;
Labbook # 25, page 128;
Time: 1115 - 1136
Date: November 26th, 2014

[data14p]

page **105**

Eighteen-ion crystal; Doppler and EIT cooled red-sideband radial mode spectrum;

Labbook # 25, page 128;

Time: 1255 - 1342

Date: November 26th, 2014

Bibliography

- [1] E. Speyer, *Six roads from Newton: great discoveries in physics*, New York: Wiley, 1994.
- [2] R. Baierlein, *Newton to Einstein: the trail of light; an excursion to the wave-particle duality and the special theory of relativity*, Cambridge: Cambridge University Press, 1996.
- [3] O. Darrigol, *A history of optics: from Greek antiquity to the nineteenth century*, Oxford: Oxford University Press, 2012.
- [4] M. Planck, *Zur Theorie des Gesetzes der Energieverteilung im Normalspectrum*, Verh. D. P. G. **2**, 245 (1900).
- [5] A. Einstein, *Über die Entwicklung unserer Anschauung über das Wesen und die Konstitution der Strahlung*, Ann. Phys. **322**, 132 (1905).
- [6] G. N. Lewis, *The Conservation of Photons*, Nature **118**, 874 (1926).
- [7] L. de Broglie, *The reinterpretation of wave mechanics*, Found. Phys. **1**, 5 (1970).
- [8] C. Davisson and L. H. Germer, *Diffraction of Electrons by a Crystal of Nickel*, Phys. Rev. **30**, 705 (1927).
- [9] T. Maiman, *Stimulated optical radiation in ruby*, Nature **187**, 493 (1960).
- [10] W. D. Phillips, *Nobel lecture: Laser cooling and trapping of neutral atoms*, Rev. Mod. Phys. **70**, 721 (1998).
- [11] C. N. Cohen-Tannoudji, *Nobel lecture: Manipulating atoms with photons*, Rev. Mod. Phys. **70**, 707 (1998).
- [12] D. J. Wineland, R. E. Drullinger, and F. L. Walls, *Radiation-pressure cooling of bound resonant absorbers*, Phys. Rev. Lett. **40**, 1639 (1978).
- [13] W. Neuhauser, M. Hohenstatt, P. Toschek, and H. Dehmelt, *Optical sideband cooling of visible atom cloud confined in parabolic well*, Phys. Rev. Lett. **41**, 233 (1978).
- [14] F. Diedrich, J. C. Bergquist, W. M. Itano, and D. J. Wineland, *Laser Cooling to the Zero-Point Energy of Motion*, Phys. Rev. Lett. **62**, 403 (1989).
- [15] C. Monroe, D. M. Meekhof, B. E. King, S. R. Jefferts, W. M. Itano, and D. J. Wineland, *Resolved-Sideband Raman Cooling of a Bound Atom to the 3D Zero-Point Energy*, Phys. Rev. Lett. **75**, 4011 (1995).

- [16] A. D. Cronin, J. Schmiedmayer, and D. E. Pritchard, *Optics and interferometry with atoms and molecules*, Rev. Mod. Phys. **81**, 1051 (2009).
- [17] K. Gibble and S. Chu, *Laser-cooled Cs frequency standard and a measurement of the frequency shift due to ultracold collisions*, Phys. Rev. Lett. **70**, 1771 (1993).
- [18] A. D. Ludlow, M. M. Boyd, J. Ye, E. Peik, and P. O. Schmidt, *Optical atomic clocks*, Rev. Mod. Phys. **87**, 637 (2015).
- [19] I. Bloch, J. Dalibard, and W. Zwerger, *Many-body physics with ultracold gases*, Rev. Mod. Phys. **80**, 885 (2008).
- [20] H. Häffner, W. Hänsel, C. F. Roos, P. O. Schmidt, M. Riebe, M. Chwalla, D. Chek-al Kar, J. Benhelm, U. D. Rapol, T. Körber, C. Becher, O. Gühne, W. Dür, and R. Blatt, *Quantum computation with trapped ions*, in *Controllable Quantum States*, 2008.
- [21] M. Saffman, T. G. Walker, and K. Mølmer, *Quantum information with rydberg atoms*, Rev. Mod. Phys. **82**, 2313 (2010).
- [22] T. W. Hänsch and A. L. Schawlow, *Cooling of gases by laser radiation*, Opt. Commun. **13**, 68 (1975).
- [23] R. P. Feynman, *Simulating Physics with Computers*, Int. J. Theor. Phys. **21**, 467 (1982).
- [24] P. Benioff, *Quantum mechanical models of turing machines that dissipate no energy*, Phys. Rev. Lett. **48**, 1581 (1982).
- [25] D. Deutsch, *Quantum theory, the Church-Turing principle and the universal quantum computer*, Proc. R. Soc. Lond. A **400**, 97 (1985).
- [26] D. Deutsch and R. Jozsa, *Rapid solution of problems by quantum computation*, Proc. R. Soc. Lond. A **439**, 553 (1992).
- [27] P. W. Shor, *Algorithms for quantum computation: Discrete logarithms and factoring*, in *Foundations of Computer Science, 1994 Proceedings, 35th Annual Symposium*, pages 124–134, IEEE, 1994.
- [28] J. I. Cirac and P. Zoller, *Quantum Computations with Cold Trapped Ions*, Phys. Rev. Lett. **74**, 4091 (1995).
- [29] A. R. Calderbank and P. W. Shor, *Good quantum error-correcting codes exist*, Phys. Rev. A **54**, 1098 (1996).
- [30] L. K. Grover, *Quantum Mechanics Helps in Searching for a Needle in a Haystack*, Phys. Rev. Lett. **79**, 325 (1997).
- [31] T. D. Ladd, F. Jelezko, R. Laflamme, Y. Nakamura, C. Monroe, and J. L. O’Brien, *Quantum computers*, Nature **464**, 45 (2010).

- [32] D. P. DiVincenzo, *The Physical Implementation of Quantum Computation*, Fortschr. Phys. **48**, 771 (2000).
- [33] D. J. Wineland and D. Leibfried, *Quantum information processing and metrology with trapped ions*, Laser Phys. Lett. **8**, 175 (2011).
- [34] D. J. Wineland, C. Monroe, W. M. Itano, D. Leibfried, B. E. King, and D. M. Meekhof, *Experimental Issues in Coherent Quantum-State Manipulation of Trapped Atomic Ions*, J. Res. Natl. Inst. Stand. Technol. **103**, 259 (1998).
- [35] C. Monroe, D. M. Meekhof, B. E. King, W. M. Itano, and D. J. Wineland, *Demonstration of a Fundamental Quantum Logic Gate*, Phys. Rev. Lett. **75**, 4714 (1995).
- [36] F. Schmidt-Kaler, S. Gulde, M. Riebe, T. Deuschle, A. Kreuter, G. Lancaster, C. Becher, J. Eschner, H. Häffner, and R. Blatt, *The coherence of qubits based on single Ca^+ ions*, J. Phys. B **36**, 623 (2003).
- [37] P. Schindler, D. Nigg, T. Monz, J. T. Barreiro, E. Martinez, S. X. Wang, S. Quint, M. F. Brandl, V. Nebendahl, C. F. Roos, M. Chwalla, M. Hennrich, and R. Blatt, *A quantum information processor with trapped ions*, New J. Phys. **15**, 123012 (2013).
- [38] T. Monz, *Quantum information processing beyond ten ion-qubits*, PhD thesis, Leopold-Franzens-Universität Innsbruck, 2011.
- [39] R. Blatt and D. Wineland, *Entangled states of trapped atomic ions*, Nature **453**, 1008 (2008).
- [40] F. Mintert and C. Wunderlich, *Ion-Trap Quantum Logic Using Long-Wavelength Radiation*, Phys. Rev. Lett. **87**, 257904 (2001).
- [41] M. Johanning, A. Braun, N. Timoney, V. Elman, W. Neuhauser, and C. Wunderlich, *Individual Addressing of Trapped Ions and Coupling of Motional and Spin States using rf Radiation*, Phys. Rev. Lett. **102**, 073004 (2009).
- [42] C. Ospelkaus, U. Warring, Y. Colombe, K. R. Brown, J. M. Amini, D. Leibfried, and D. J. Wineland, *Microwave quantum logic gates for trapped ions*, Nature **476**, 181 (2011).
- [43] F. Schmidt-Kaler, H. Häffner, M. Riebe, S. Gulde, G. P. T. Lancaster, T. Deuschle, C. Becher, C. F. Roos, J. Eschner, and R. Blatt, *Realization of the Cirac-Zoller controlled-NOT quantum gate*, Nature **422**, 408 (2003).
- [44] A. Sørensen and K. Mølmer, *Quantum computation with ions in thermal motion*, Phys. Rev. Lett. **82**, 1971 (1999).
- [45] G. J. Milburn, S. Schneider, and D. F. James, *Ion trap quantum computing with warm ions*, Fortschr. Phys. **48**, 801 (2000).

- [46] E. Solano, R. L. de Matos Filho, and N. Zagury, *Coherent Manipulation of Two Trapped Ions with Bichromatic Light*, in *Modern Challenges in Quantum Optics*, Berlin Heidelberg: Springer, 2001.
- [47] G. Kirchmair, J. Benhelm, F. Zähringer, R. Gerritsma, C. F. Roos, and R. Blatt, *Deterministic entanglement of ions in thermal states of motion*, *New J. Phys.* **11**, 1 (2009).
- [48] G. Morigi, J. Eschner, and C. H. Keitel, *Ground State Laser Cooling Using Electromagnetically Induced Transparency*, *Phys. Rev. Lett.* **85**, 4458 (2000).
- [49] C. F. Roos, D. Leibfried, A. Mundt, F. Schmidt-Kaler, J. Eschner, and R. Blatt, *Experimental Demonstration of Ground State Laser Cooling with Electromagnetically Induced Transparency*, *Phys. Rev. Lett.* **85**, 5547 (2000).
- [50] Y. Lin, J. P. Gaebler, T. R. Tan, R. Bowler, J. Jost, D. Leibfried, and D. J. Wineland, *Sympathetic electromagnetically-induced-transparency laser cooling of motional modes in an ion chain*, *Phys. Rev. Lett.* **110**, 153002 (2013).
- [51] E. Haller, J. Hudson, A. Kelly, D. A. Cotta, B. Peaudecerf, G. D. Bruce, and S. Kuhr, *Single-atom imaging of fermions in a quantum-gas microscope*, *Nature Phys.* **11**, 738 (2015).
- [52] T. Kampschulte, W. Alt, S. Manz, M. Martinez-Dorantes, R. Reimann, S. Yoon, D. Meschede, M. Bienert, and G. Morigi, *Electromagnetically-induced-transparency control of single-atom motion in an optical cavity*, *Phys. Rev. A* **89**, 033404 (2014).
- [53] J.-P. Zhu and G.-X. Li, *Ground-state cooling of a nanomechanical resonator with a triple quantum dot via quantum interference*, *Phys. Rev. A* **86**, 053828 (2012).
- [54] A. Kreuter, C. Becher, G. P. T. Lancaster, A. B. Mundt, C. Russo, H. Häffner, C. Roos, W. Hänsel, F. Schmidt-Kaler, R. Blatt, and M. S. Safronova, *New experimental and theoretical approach to the 3d 2D-level lifetime of $^{40}\text{Ca}^+$* , *Phys. Rev. A* **71**, 032504 (2005).
- [55] M. Harlander, R. Lechner, M. Brownnutt, R. Blatt, and W. Hänsel, *Trapped-ion antennae for the transmission of quantum information*, *Nature* **471**, 200 (2011).
- [56] K. R. Brown, C. Ospelkaus, Y. Colombe, A. C. Wilson, D. Leibfried, and D. J. Wineland, *Coupled quantized mechanical oscillators*, *Nature* **471**, 196 (2011).

- [57] G.-D. Lin, S.-L. Zhu, R. Islam, K. Kim, M.-S. Chang, S. Korenblit, C. Monroe, and L.-M. Duan, *Large-scale quantum computation in an anharmonic linear ion trap*, Europhys. Lett. **86**, 60004 (2009).
- [58] W. Paul, O. Osberghaus, and E. Fischer, *Ein Ionenkäfig*, in *Forschungsberichte des Wirtschafts- und Verkehrsministeriums Nordrhein-Westfalen*, volume 415, Köln, Opladen: Westdeutscher Verlag, 1958.
- [59] W. Paul, *Electromagnetic traps for charged and neutral particles*, Rev. Mod. Phys. **62**, 531 (1990).
- [60] H. G. Dehmelt and F. G. Major, *Orientation of $(He^4)^+$ ions by exchange collisions with cesium atoms*, Phys. Rev. Lett **8**, 213 (1962).
- [61] C. Zipkes, S. Palzer, C. Sias, and M. Köhl, *A trapped single ion inside a Bose-Einstein condensate*, Nature **464**, 388 (2010).
- [62] J. J. Bollinger, D. J. Heinzen, W. M. Itano, S. L. Gilbert, and D. J. Wineland, *A 303-MHz Frequency Standard Based on Trapped Be^+ Ions*, IEEE T. Instrum. Meas. **40**, 126 (1991).
- [63] S. A. Diddams, J. C. Bergquist, S. R. Jefferts, and C. W. Oates, *Standards of Time and Frequency at the Outset of the 21st Century*, Science **306**, 1318 (2004).
- [64] P. K. Ghosh, *Ion Traps*, Oxford: Clarendon Press, 1995.
- [65] M. D. Hughes, B. Lekitsch, J. A. Broersma, and W. K. Hensinger, *Micro-fabricated ion traps*, Contemp. Phys. **52**, 505 (2011).
- [66] G. Werth, V. N. Gheorghie, and F. G. Major, *Charged Particle Traps II*, Berlin: Springer, 2009.
- [67] D. Kielpinski, C. Monroe, and D. J. Wineland, *Architecture for a large-scale ion-trap quantum computer*, Nature **417**, 709 (2002).
- [68] D. J. Wineland, *Quantum information processing and quantum control with trapped atomic ions*, Phys. Scr. **2009**, 014007 (2009).
- [69] T. Monz, K. Kim, W. Hänsel, M. Riebe, A. S. Villar, P. Schindler, M. Chwalla, M. Hennrich, and R. Blatt, *Realization of the Quantum Toffoli Gate with Trapped Ions*, Phys. Rev. Lett. **102**, 040501 (2009).
- [70] D. Leibfried, R. Blatt, C. Monroe, and D. Wineland, *Quantum dynamics of single trapped ions*, Rev. Mod. Phys. **75**, 261 (2003).
- [71] C. Roos, *Controlling the quantum state of trapped ions*, PhD thesis, Leopold-Franzens-Universität Innsbruck, 2000.
- [72] J. D. Berkeland, J. D. Miller, J. C. Bergquist, W. M. Itano, and D. J. Wineland, *Minimization of ion micromotion in a Paul trap*, J. Appl. Phys. **83**, 5025 (1998).

- [73] M. Brownnutt, M. Kumph, P. Rabl, and R. Blatt, *Ion-trap measurement of electric-field noise near surfaces*, Rev. Mod. Phys. **87**, 1419 (2015).
- [74] J. D. Prestage, G. J. Dick, and L. Maleki, *New ion trap for frequency standard applications*, J. Appl. Phys. **66**, 1013 (1989).
- [75] S. T. Gulde, *Experimental Realization of Quantum Gates and the Deutsch-Jozsa Algorithm with Trapped $^{40}\text{Ca}^+$ Ions*, PhD thesis, Leopold-Franzens-Universität Innsbruck, 2003.
- [76] J. P. Home, D. Hanneke, J. D. Jost, D. Leibfried, and D. J. Wineland, *Normal modes of trapped ions in the presence of anharmonic trap potentials*, New J. Phys. **13**, 073026 (2011).
- [77] J. P. Schiffer, *Phase Transitions in Anisotropically Confined Ionic Crystals*, Phys. Rev. Lett. **70**, 818 (1993).
- [78] D. H. E. Dubin, *Theory of Structural Phase Transitions in a Trapped Coulomb Crystal*, Phys. Rev. Lett. **71**, 2753 (1993).
- [79] A. Steane, *The ion trap quantum information processor*, Appl. Phys. B **64**, 623 (1997).
- [80] D. F. V. James, *Quantum dynamics of cold trapped ions with application to quantum computation*, Appl. Phys. B **66**, 181 (1998).
- [81] D. G. Enzer, M. M. Schauer, J. J. Gomez, M. S. Gulley, M. H. Holzscheiter, P. G. Kwiat, S. K. Lamoreaux, C. G. Peterson, V. D. Sandberg, D. Tupa, A. G. White, and R. J. Hughes, *Observation of Power-Law Scaling for Phase Transitions in Linear Trapped Ion Crystals*, Phys. Rev. Lett. **85**, 2466 (2000).
- [82] D. Kielpinski, B. E. King, C. J. Myatt, C. A. Sackett, Q. A. Turchette, W. M. Itano, C. Monroe, and D. J. Wineland, *Sympathetic cooling of trapped ions for quantum logic*, Phys. Rev. A **61**, 032310 (2000).
- [83] J. P. Home and A. M. Steane, *Electrode configuration for fast separation of trapped ions*, Quantum Inf. Comput. **6**, 289 (2006).
- [84] M. J. Harlander, *Architecture for a scalable ion-trap quantum computer*, PhD thesis, Leopold-Franzens-Universität Innsbruck, 2012.
- [85] S. Fishman, G. De Chiara, T. Calarco, and G. Morigi, *Structural phase transition in low-dimensional ion crystals*, Phys. Rev. B **77**, 064111 (2008).
- [86] S. Stenholm, *The semiclassical theory of laser cooling*, Rev. Mod. Phys. **58**, 699 (1986).
- [87] J. Eschner, G. Morigi, F. Schmidt-Kaler, and R. Blatt, *Laser cooling of trapped ions*, J. Opt. Soc. Am. B **20**, 1003 (2003).

- [88] H. J. Metcalf and P. van der Straten, *Laser Cooling and Trapping*, New York: Springer, 1999.
- [89] R. Loudon, *The Quantum Theory of Light*, Oxford: Clarendon Press, 2007.
- [90] C. J. Foot, *Atomic Physics*, Oxford: Oxford University Press, 2008.
- [91] C. Cohen-Tannoudji, B. Diu, and F. Laloë, *Quantenmechanik 1*, Berlin: De Gruyter, 1999.
- [92] C. A. Blockley, D. F. Walls, and H. Risken, *Quantum Collapses and Revivals in a Quantized Trap.*, Europhys. Lett. **17**, 509 (1992).
- [93] A. Sørensen and K. Mølmer, *Entanglement and quantum computation with ions in thermal motion*, Phys. Rev. A **62**, 022311 (2000).
- [94] J. I. Cirac, L. J. Garay, R. Blatt, A. S. Parkins, and P. Zoller, *Laser cooling of trapped ions: The influence of micromotion*, Phys. Rev. A **49**, 421 (1994).
- [95] D. Reiß, A. Lindner, and R. Blatt, *Cooling of trapped multilevel ions: A numerical analysis*, Phys. Rev. A **54**, 5133 (1996).
- [96] D. Reiß, K. Abich, W. Neuhauser, C. Wunderlich, and P. E. Toschek, *Raman cooling and heating of two trapped Ba⁺ ions*, Phys. Rev. A **65**, 053401 (2002).
- [97] M. Hettrich, T. Ruster, H. Kaufmann, C. F. Roos, C. T. Schmiegelow, F. Schmidt-Kaler, and U. G. Poschinger, *Measurement of dipole matrix elements with a single trapped ion*, Phys. Rev. Lett. **115**, 143003 (2015).
- [98] I. Marzoli, J. I. Cirac, R. Blatt, and Zoller, *Laser cooling of trapped three-level ions: Designing two-level systems for sideband cooling*, Phys. Rev. A **49**, 2771 (1994).
- [99] J. I. Cirac, R. Blatt, P. Zoller, and W. D. Phillips, *Laser cooling of trapped ions in a standing wave*, Phys. Rev. A **46**, 2668 (1992).
- [100] S. E. Harris, *Electromagnetically Induced Transparency*, Phys. Today **50**, 36 (1997).
- [101] H. R. Gray, R. M. Whitley, and C. R. Stroud Jr., *Coherent trapping of atomic populations*, Opt. Lett. **3**, 218 (1978).
- [102] B. Lounis and C. Cohen-Tannoudji, *Coherent population trapping and Fano profiles*, J. Phys. II **2**, 579 (1992).
- [103] R. Blatt, J. I. Cirac, and P. Zoller, *Trapping states of motion with cold ions*, Phys. Rev. A **52**, 518 (1995).
- [104] D. M. Meekhof, C. Monroe, B. E. King, W. M. Itano, and D. J. Wineland, *Generation of Nonclassical Motional States of a Trapped Atom*, Phys. Rev. Lett. **76**, 1796 (1996).

- [105] Q. A. Turchette, D. Kielpinski, B. E. King, D. Leibfried, D. M. Meekhof, C. J. Myatt, M. A. Rowe, C. A. Sackett, C. S. Wood, W. M. Itano, C. Monroe, and D. J. Wineland, *Heating of trapped ions from the quantum ground state*, Phys. Rev. A **61**, 063418 (2000).
- [106] J. I. Cirac, R. Blatt, A. S. Parkins, and P. Zoller, *Quantum collapse and revival in the motion of a single trapped ion*, Phys. Rev. A **49**, 1202 (1994).
- [107] N. V. Vitanov, T. Halfmann, B. W. Shore, and K. Bergmann, *Laser-induced population transfer by adiabatic passage techniques*, Annu. Rev. Phys. Chem. **52**, 763 (2001).
- [108] X. Chen, I. Lizuain, A. Ruschhaupt, D. Guéry-Odelin, and J. G. Muga, *Shortcut to Adiabatic Passage in Two- and Three-Level Atoms*, Phys. Rev. Lett. **105**, 123003 (2010).
- [109] A. S. Parkins, P. Marte, P. Zoller, and H. J. Kimble, *Synthesis of Arbitrary Quantum States via Adiabatic Transfer of Zeeman Coherences*, Phys. Rev. Lett. **71**, 3095 (1993).
- [110] J. I. Cirac, R. Blatt, and P. Zoller, *Nonclassical states of motion in a three-dimensional ion trap by adiabatic passage*, Phys. Rev. **49**, R3174 (1994).
- [111] I. E. Linington, P. A. Ivanov, N. V. Vitanov, and M. B. Plenio, *Robust control of quantized motional states of a chain of trapped ions by collective adiabatic passage*, Phys. Rev. A **77** (2008).
- [112] C. Wunderlich, T. Hannemann, T. Körber, H. Häffner, C. Roos, W. Hänsel, R. Blatt, and F. Schmidt-Kaler, *Robust state preparation of a single trapped ion by adiabatic passage*, J. Mod. Opt. **54**, 1541 (2007).
- [113] I. E. Linington and N. V. Vitanov, *Robust creation of arbitrary-sized Dicke states of trapped ions by global addressing*, Phys. Rev. A **77**, 010302(R) (2008).
- [114] F. J. Harris, *On the Use of Windows for Harmonic Analysis with the Discrete Fourier Transform*, in *Proceedings of the IEEE*, volume 66, 1978.
- [115] P. Schindler, *Frequency synthesis and pulse shaping for quantum information processing with trapped ions*, Master's thesis, Leopold-Franzens-Universität Innsbruck, 2008.
- [116] J. R. Morris and B. W. Shore, *Reduction of degenerate two-level excitation to independent two-state systems*, Phys. Rev. A **27**, 906 (1983).
- [117] A. A. Rangelov, N. V. Vitanov, and B. W. Shore, *Extension of the Morris-Shore transform to multilevel ladders*, Phys. Rev. A **74**, 053402 (2006).
- [118] T. Watanabe, S. Nomura, K. Toyoda, and S. Urabe, *Sideband excitation of trapped ions by rapid adiabatic passage for manipulation of motional states*, Phys. Rev. A **84**, 033412 (2011).

- [119] W. Nagourney, J. Sandberg, and H. Dehmelt, *Shelved Optical Electron Amplifier: Observation of Quantum Jumps*, Phys. Rev. Lett. **56**, 2797 (1986).
- [120] T. Sauter, W. Neuhauser, R. Blatt, and P. E. Toschek, *Observation of Quantum Jumps*, Phys. Rev. Lett. **57**, 1696 (1986).
- [121] J. C. Bergquist, R. G. Hulet, W. M. Itano, and D. J. Wineland, *Observation of Quantum Jumps in a Single Atom*, Phys. Rev. Lett. **57**, 1699 (1986).
- [122] R. J. Hughes, D. F. V. James, E. H. Knill, R. Laflamme, and A. G. Petschek, *Decoherence Bounds on Quantum Computation with Trapped Ions*, Phys. Rev. Lett. **77**, 3240 (1996).
- [123] S. Schulz, *Scalable Microchip Ion Traps for Quantum Computation*, PhD thesis, Universität Ulm, 2009.
- [124] S. Gulde, D. Rotter, P. Barton, F. Schmidt-Kaler, R. Blatt, and W. Hogervorst, *Simple and efficient photo-ionization loading of ions for precision ion-trapping experiments*, Appl. Phys. B **73**, 861 (2001).
- [125] R. W. P. Drever, J. L. Hall, F. V. Kowalski, J. Hough, G. M. Ford, A. J. Munley, and H. Ward, *Laser Phase and Frequency Stabilization Using an Optical Resonator*, Appl. Phys. B **31**, 97 (1983).
- [126] J. Benhelm, *Precision Spectroscopy and Quantum Information Processing with Trapped Calcium Ions*, PhD thesis, Leopold-Franzens-Universität Innsbruck, 2008.
- [127] H. G. de Barros, *Raman spectroscopy and single-photon source in an ion-cavity system*, PhD thesis, Leopold-Franzens-Universität Innsbruck, 2010.
- [128] M. Chwalla, *Precision spectroscopy with $^{40}\text{Ca}^+$ ions in a Paul trap*, PhD thesis, Leopold-Franzens-Universität Innsbruck, 2009.
- [129] W. M. Itano, J. C. Bergquist, J. J. Bollinger, J. M. Gilligan, D. J. Heinzen, F. L. Moore, M. G. Raizen, and D. J. Wineland, *Quantum projection noise: Population fluctuations in two-level systems*, Phys. Rev. A **47**, 3550 (1993).
- [130] D. Rotter, *Quantum feedback and quantum correlation measurements with a single Barium ion*, PhD thesis, Leopold-Franzens-Universität Innsbruck, 2008.
- [131] S. Schneider, D. Porras, and T. Schaetz, *Experimental quantum simulation of many-body physics with trapped ions*, Rep. Prog. Phys. **75**, 024401 (2012).
- [132] P. Jurcevic, B. P. Lanyon, P. Hauke, C. Hempel, P. Zoller, R. Blatt, and C. F. Roos, *Quasiparticle engineering and entanglement propagation in a quantum many-body system*, Nature **511**, 202 (2014).

- [133] P. Richerme, Z.-X. Gong, A. Lee, C. Senko, J. Smith, M. Foss-Feig, S. Michalakis, A. V. Gorshkov, and C. Monroe, *Non-local propagation of correlations in long-range interacting quantum systems*, Nature **511**, 198 (2014).
- [134] S.-L. Zhu, C. Monroe, and L.-M. Duan, *Trapped Ion Quantum Computation with Transverse Phonon Modes*, Phys. Rev. Lett. **97**, 050505 (2006).
- [135] C. Monroe and J. Kim, *Scaling the Ion Trap Quantum Processor*, Science **339**, 1164 (2013).
- [136] A. Walther, F. Ziesel, T. Ruster, S. T. Dawkins, K. Ott, M. Hettrich, K. Singer, F. Schmidt-Kaler, and U. Poschinger, *Controlling Fast Transport of Cold Trapped Ions*, Phys. Rev. Lett. **109**, 080501 (2012).
- [137] R. Bowler, J. Gaebler, Y. Lin, T. R. Tan, D. Hanneke, J. D. Jost, J. P. Home, D. Leibfried, and D. J. Wineland, *Coherent Diabatic Ion Transport and Separation in a Multizone Trap Array*, Phys. Rev. Lett. **109**, 080502 (2012).
- [138] C. Hempel, *Digital quantum simulation, Schrödinger cat state spectroscopy and setting up a linear ion trap*, PhD thesis, Leopold-Franzens-Universität Innsbruck, 2014.
- [139] J. P. Home, *Quantum science and metrology with mixed-species ion chains*, Adv. Atom. Mol. Opt. Phys. **62**, 231 (2013).
- [140] B. C. Sawyer, J. W. Britton, and J. J. Bollinger, *Spin dephasing as a probe of mode temperature, motional state distribution, and heating rates in a two-dimensional ion crystal*, Phys. Rev. A **89**, 033408 (2014).
- [141] C. Marquet, F. Schmidt-Kaler, and D. F. V. James, *Phonon-phonon interactions due to non-linear effects in a linear ion trap*, Appl. Phys. B **76**, 199 (2003).
- [142] N. F. Ramsey, *Experiments with separated oscillatory fields and hydrogen masers*, Rev. Mod. Phys. **62**, 541 (1990).
- [143] R. Blatt and C. F. Roos, *Quantum simulation with trapped ions*, Nature Phys. **8**, 277 (2013).

Danksagung

Das Ausmaß an Dingen, welche ich während meiner Doktorarbeit lernen durfte, übersteigt den rein physikalischen Aspekt bei Weitem! Die Zusammenarbeit mit einer Vielzahl von Persönlichkeiten an einem spannenden, sich ständig weiterentwickelnden Thema, gab stets dazu Anlass, über sich hinauszuwachsen.

Mein besonderer Dank gilt Rainer Blatt, der mit seiner international renommierten Arbeitsgruppe in Innsbruck erst die Möglichkeit geschaffen hat, um Quantenforschung am Puls der Zeit durchzuführen. Innerhalb der Arbeitsgruppe gab es eine Vielzahl von Menschen, die mich in meinem Bemühen unterstützt haben. Namentlich erwähnen möchte ich hier Mike, unter dessen Betreuung ein Großteil meiner Doktoratszeit fiel. Speziell bedanken will ich mich beim QSim-Team: Danke an Christian, Christine, Cornelius und Petar für die gute Zusammenarbeit! Es war für mich unglaublich und erhebend, wie viel in kurzer Zeit geschafft werden kann, wenn man am gleichen Strang zieht! Dabei darf auch Max nicht vergessen werden, der mich an seiner Weisheit und Kochkunst hat teilhaben lassen — Hoch lebe die Weißwurstgruppe!

Natürlich gibt es noch einige andere, die immer da waren, um Fragen zu beantworten und einen schlechten Tag im Labor mit Humor aufzulockern und besser zu machen. Mein Dank hierfür gilt Tomi, Dani, Philipp, Esteban, Bernardo und noch einigen anderen, sowohl im großen Labor als auch am IQOQI und im 4. Stock.

Des Weiteren möchte ich auch noch meine Anerkennung für die nichtwissenschaftlichen Mitarbeiterinnen und Mitarbeiter in den Sekretariaten und mechanischen und elektronischen Werkstätten aussprechen: ohne euch würde Vieles nicht funktionieren. Danke für all eure Bemühungen und euren Einsatz!

Nicht vergessen möchte ich die Personen, die immer für mich da waren und mir sowohl ein Sicherheitsnetz als auch ein beständiger Ansporn waren. Mein größter Dank gilt hierbei meinem Partner Florian: Du verstehst es, mich auch in nahezu ausweglos scheinenden Situationen zum Lachen zu bringen und mich zu motivieren, wenn ich das Gefühl habe nicht mehr weitermachen zu können. Anerkennung und Dankbarkeit empfinde ich auch für meine Freundin Anke: Egal ob Freude oder Leid, du bist da um es zu teilen. Gemeinsam gegen die Einbahnstraße! Natürlich möchte ich mich auch bei meinen Eltern, Monika & Hermann, bedanken: Ihr habt mir so Vieles ermöglicht, mich immer unterstützt und mich mit zu dem Menschen gemacht, der ich heute bin. Abschließend noch ein großes Danke an den Rest meiner Familie sowie Antonia, Petra und Stefanie!

Ein herzliches Dankeschön!